

**1 Constraints on the Observability of Energetic Neutral  
2 Atoms from the Magnetosphere-Atmosphere  
3 Interactions at Callisto and Europa**

**4 C. Michael Haynes<sup>1</sup>, Tyler Tippens<sup>1</sup>, Sven Simon<sup>1,2</sup>, Lucas Liuzzo<sup>3</sup>**

**5** <sup>1</sup>School of Earth and Atmospheric Sciences, Georgia Institute of Technology, Atlanta, Georgia, USA

**6** <sup>2</sup>School of Physics, Georgia Institute of Technology, Atlanta, Georgia, USA

**7** <sup>3</sup>Space Sciences Laboratory, University of California, Berkeley, California, USA

**8 Key Points:**

- 9** • We generate synthetic images of the energetic neutral atom (ENA) flux from the  
magnetosphere-atmosphere interactions at Europa and Callisto
- 10** • Detectable ENA emissions form a segmented ring around each moon's disc; the  
ring's angular and radial structure is governed by ion gyroradii
- 11** • When Europa and Callisto are near the center of Jupiter's plasma sheet, the mag-  
netic draping pattern is visible from certain vantage points
- 12**
- 13**
- 14**

---

Corresponding author: C. Michael Haynes, [mhaynes@eas.gatech.edu](mailto:mhaynes@eas.gatech.edu)

15      **Abstract**

16      We investigate the emission of energetic neutral atoms (ENAs) from the magnetosphere-  
 17      atmosphere interactions at Europa and Callisto that may be observed by an ENA imag-  
 18      ing instrument. To do so, we combine the draped electromagnetic fields from the AIKEF  
 19      hybrid model with a tracing tool for the energetic magnetospheric parent ions. Using a  
 20      realistic viewing geometry, synthetic ENA images are generated for multiple detector po-  
 21      sitions and orientations with respect to the magnetospheric field. At both moons, we in-  
 22      vestigate the ENA emission morphology at different distances to the center of Jupiter's  
 23      plasma sheet. By generating ENA images for uniform electromagnetic fields as a base-  
 24      line, we also constrain the influence of field line draping and induction signals on the ob-  
 25      servable ENA emission signatures. Our major findings are: (a) In uniform fields, regions  
 26      of elevated ENA flux in the images populate segments of a ring around each moon's disc.  
 27      (b) The radial and angular extensions of these segments decrease with growing magne-  
 28      tospheric field strength. (c) The angle between the detector's boresight vector and the  
 29      ambient field determines the regions of the images populated with elevated ENA flux.  
 30      (d) Non-uniformities in the fields are discernible in the ENA images only when Europa  
 31      and Callisto are located near the center of Jupiter's plasma sheet. Even in this case, the  
 32      visibility of such features is restricted to certain viewing geometries. (e) Anisotropies in  
 33      the moons' atmospheric density profiles produce gradients in the observable ENA emis-  
 34      sions. This facilitates a global characterization of these neutral envelopes through ENA  
 35      imaging.

36      **1 Introduction**

37      Europa (radius  $R_E = 1560.8$  km) and Callisto (radius  $R_C = 2410.3$  km) are both  
 38      moons of Jupiter that maintain nearly circular, tidally-locked orbits in the planet's equa-  
 39      torial plane, located at radial distances of  $9.4R_J$  and  $26.3R_J$ , respectively (Jupiter's ra-  
 40      dius:  $R_J = 71,492$  km). The surfaces of these moons are rich in water ice, and each has  
 41      a tenuous atmosphere generated in part through sublimation (e.g., Spencer et al., 1999;  
 42      Galli et al., 2018) and sputtering (e.g., Vorburger & Wurz, 2018; Addison et al., 2022;  
 43      Carberry Mogan et al., 2023). Europa's neutral envelope consists largely of molecular  
 44      oxygen (Hall et al., 1995, 1998; Roth et al., 2016) with a secondary contribution from  
 45      water vapor. Specifically, observations from the Hubble Space Telescope revealed the ex-  
 46      istence of a localized increase in  $H_2O$  density, peaking around Europa's subsolar (or ram-

47 side) apex with a column density comparable to that of O<sub>2</sub> near this point (Roth, 2021).  
 48 Other water group products have been detected in Europa's atmosphere at concentra-  
 49 tions below 5% (e.g., Roth et al., 2016, 2017). At Callisto, CO<sub>2</sub> was the first atmospheric  
 50 constituent identified by using UV observations taken by the Galileo spacecraft during  
 51 the C10 flyby (Carlson et al., 1996; Carlson, 1999). However, molecular oxygen was sub-  
 52 sequently found to be the dominant component, with its number density near the sur-  
 53 face exceeding that of CO<sub>2</sub> by over an order of magnitude (Kliore et al., 2002; Cunning-  
 54 ham et al., 2015). Europa's and Callisto's atmospheres are partially ionized by electron  
 55 impacts and solar UV photons (e.g., Saur et al., 1998; Gurnett et al., 2000; Carberry Mo-  
 56 gan et al., 2022), generating ionospheres around these moons.

57 The orbits of Callisto and Europa are embedded within Jupiter's magnetosphere,  
 58 and as such, the moons are constantly exposed to the planet's magnetic field. Along Eu-  
 59 opa's orbit, Jupiter's internal field provides the dominant contribution to the magne-  
 60 tospheric field (Connerney et al., 2018, 2022). As distance from the planet's magnetic  
 61 axis increases –that is, moving from Europa's to Callisto's orbit– a growing contribution  
 62 stems from the equatorial current sheet (Khurana, 1997; Connerney et al., 2020). Jupiter's  
 63 magnetic moment is misaligned by about 9.6° with respect to its spin axis; consequen-  
 64 tially, the distance of Europa and Callisto the magnetic equator periodically varies. At  
 65 this equator, the magnetic field is oriented approximately southward. Above and below  
 66 the magnetic equator, the field is still (to within about 30°) southward at Europa's or-  
 67 bit, but the contribution of the current sheet causes a largely radial field orientation near  
 68 Callisto (e.g., Connerney et al., 2018; Liuzzo et al., 2022). The Jovian magnetic moment,  
 69 as perceived at the positions of Europa or Callisto, can be decomposed into a constant  
 70 component aligned with Jupiter's rotation axis and a time-varying (horizontal) compo-  
 71 nent in the moons' orbital plane. Over a synodic period of Jupiter (10.18 hr at Callisto  
 72 and 11.23 hr at Europa) each moon experiences one complete rotation of this horizon-  
 73 tal component (Kivelson et al., 2000; Zimmer et al., 2000; Khurana et al., 2009). This  
 74 periodicity in the ambient magnetic field induces a secondary field in any conducting lay-  
 75 ers at Europa and Callisto (Seufert et al., 2011), such as a salty subsurface ocean (Zimmer  
 76 et al., 2000; Vance et al., 2018, 2021) or a conductive ionosphere (Hartkorn & Saur, 2017).  
 77 These induction signals can perturb the Jovian magnetospheric field near Europa's or  
 78 Callisto's surfaces by upwards of 20% and 60%, respectively (e.g., Khurana et al., 1998;  
 79 Kivelson et al., 2000; Seufert et al., 2011; Vance et al., 2018).

80 Jupiter's magnetosphere contains a thermal plasma population with energies  $E \lesssim$   
 81 1 keV, transporting synchronously with the magnetic field and confined to a disc-like sheet  
 82 concentrated about the centrifugal equator (Bagenal & Delamere, 2011; Phipps & Bage-  
 83 nal, 2021). Moving away from the center of the plasma sheet in the north-south direc-  
 84 tion, the density of the thermal plasma decreases rapidly. Therefore, over a synodic ro-  
 85 tation, the ambient plasma density at Europa and Callisto changes periodically. Due to  
 86 Jupiter's fast rotation, the thermal plasma constantly impinges upon Europa's and Cal-  
 87 listo's trailing hemispheres at a relative velocity of about 100 – 200 km/s (Kivelson et  
 88 al., 2004; Bagenal et al., 2015, 2016). At both moons, newly created ionospheric ions are  
 89 picked up by the magnetospheric fields and carried downstream, mass-loading the inci-  
 90 dent plasma flow. The deflection of the thermal plasma by the moons' ionospheres and  
 91 induced fields causes the magnetospheric field to pile up around their trailing (ramside)  
 92 hemispheres, forming a draping pattern. At large distances, this pattern connects to a  
 93 system of Alfvén wings that ultimately reach Jupiter's polar ionosphere (Neubauer, 1980,  
 94 1998, 1999) and can excite auroral footprints (e.g., Bonfond et al., 2017; Bhattacharyya  
 95 et al., 2018; Moirano et al., 2024). The field enhancement in Callisto's pile-up region may  
 96 exceed five times the ambient magnetospheric field strength (Liuzzo et al., 2022), whereas  
 97 it remains below 50% of the background field at Europa (Kivelson et al., 1999, 2009).  
 98 Due to the periodic variation in the upstream plasma conditions and magnetic field at  
 99 these moons, the strength and shape of the perturbations vary with the Jovian synodic  
 100 frequency, too (Schilling et al., 2007; Addison et al., 2021; Harris et al., 2021).

### 101 1.1 Emission of Energetic Neutral Atoms

102 In addition to the thermal plasma, a population of energetic magnetospheric ions  
 103 and electrons with energies  $E > 1$  keV exists throughout Jupiter's magnetosphere (e.g.,  
 104 Paranicas et al., 2000; Mauk et al., 2004; Clark et al., 2019). These particles bounce along  
 105 magnetospheric field lines while drifting azimuthally. When interacting with Europa or  
 106 Callisto, energetic ions and electrons can be described as a test particle population sub-  
 107 ject to the magnetospheric fields (e.g., Liuzzo et al., 2019a, 2019b, 2024; Nordheim et  
 108 al., 2022; Addison et al., 2021, 2022, 2023). The energetic ion population is comprised  
 109 of mostly protons, oxygen, and sulfur (e.g., Paranicas et al., 2000; Cohen et al., 2001;  
 110 Clark et al., 2020) which constantly bombard the atmospheres and surfaces of Europa  
 111 and Callisto. When Callisto is near the center of Jupiter's magnetospheric plasma sheet,

energetic sulfur and oxygen ions heavily irradiate the region around the ramside apex, with their influx reduced by about a factor of two at other locations on the moon's surface (Liuzzo et al., 2019b, 2022). The energetic protons bombard Callisto nearly uniformly, apart from a 50% drop in influx around the Jupiter-averted apex. Moving from the center to far outside the Jovian plasma sheet, the influx of all three ion species maximizes near the Jupiter-averted and Jupiter-facing apices (Liuzzo et al., 2022). For the case of Europa located at the center of Jupiter's plasma sheet, the energetic ion influx is minimized around the ramside apex for all three species (Addison et al., 2021). This localized reduction in surface irradiation is still present when Europa is far from the center of the sheet; in this case, an additional depletion in the precipitation pattern stretches around the moon along its equator. Comparing energetic ion precipitation obtained for uniform and draped fields, the influx at both Europa and Callisto is reduced by a factor of 2–5 at most surface locations when the field perturbations are taken into account. Even so, the draped fields allow energetic ions to irradiate regions on the surface which are inaccessible in uniform fields, and vice versa (Breer et al., 2019; Addison et al., 2021; Liuzzo et al., 2019b, 2022).

Not all of the incident energetic ions impact Europa's and Callisto's surfaces and contribute to their erosion (Addison et al., 2021; Carberry Mogan et al., 2023; Haynes et al., 2023). Some interact with the moons' atmospheres through charge exchange, where the energetic ion strips an electron from a neutral particle. At Europa, such charge exchange processes were found to contribute to the reductions in energetic proton fluxes observed during Galileo's flybys of the moon (Huybrighs et al., 2023). Charge exchange between energetic ions and atmospheric neutrals is highly forward-scattered, so the newly created Energetic Neutral Atom (ENA) travels away with the momentary velocity of the parent ion at the moment of charge exchange (e.g., Dandouras & Amsif, 1999; Lindsay & Stebbings, 2005). The kinetic energy of an ENA is vast compared to its potential energy in the gravitational fields of the Jovian system, so it propagates along a straight line (e.g., Mauk et al., 2003; Mauk, Clark, et al., 2020; Mauk, Allegrini, et al., 2020). As revealed by the model of Haynes et al. (2023), ENAs generated through charge exchange with Callisto's and Europa's atmospheres typically have energies between 5–100 keV. This is because the energetic ion abundance is reduced below a few keV (Paranicas et al., 2002; Mauk et al., 2004), and the cross sections for charge exchange decline steeply above energies of 100 keV (Lindsay & Stebbings, 2005).

145 Plasma and magnetometer observations of moon-magnetosphere interactions are  
 146 taken only along the one-dimensional trajectory of the spacecraft. Thus, multiple fly-  
 147 bys with distinct trajectories under nearly identical upstream conditions are required to  
 148 (approximately) reconstruct the three-dimensional structure of the plasma interaction  
 149 region. ENA imaging instruments such as the Ion and Neutral CAmera (INCA; Mitchell  
 150 et al., 1996; Krimigis et al., 2004) aboard the Cassini spacecraft use the incoming flux  
 151 of ENAs to construct a two-dimensional image during a certain flyby, loosely analogous  
 152 to the operation of a CCD camera for visible light. The perturbed electromagnetic fields  
 153 guide the trajectories of the energetic ions, some of which are converted into ENAs mov-  
 154 ing along tangent lines of the parent ion trajectories within the atmosphere. Since the  
 155 trajectories of the energetic ions within the moon's interaction regions determine the ENA  
 156 emission pattern, ENA imaging can partially overcome the limitations of in-situ plasma  
 157 and magnetic field data by providing global “snapshots” of the draped fields (e.g., Wulms  
 158 et al., 2010; Kabanovic et al., 2018; Tippens et al., 2022).

159 ENA images from INCA have served as a valuable diagnostic tool in characteriz-  
 160 ing the interaction between Titan and Saturn's magnetospheric plasma, which produces  
 161 qualitatively similar electromagnetic structures as Callisto's and Europa's magnetospheric  
 162 interactions (e.g., Mitchell et al., 2005; Brandt et al., 2012; Liuzzo et al., 2015). Along  
 163 Cassini's path to the Saturnian system, ENA images were captured as the spacecraft passed  
 164 the Jovian magnetosphere, but only Jupiter's atmosphere and the Europa neutral torus  
 165 were resolved at the spacecraft's large distance from the planet (Mauk et al., 2003; Smith  
 166 et al., 2019). To date, a spacecraft with an ENA detector has not yet imaged the moon-  
 167 magnetosphere interactions at Europa or Callisto, but the JUpiter ICy moons Explorer  
 168 (JUICE) is, at the time of this writing, en route to become the first (Grasset et al., 2013;  
 169 Tosi et al., 2024). It carries the JENI instrument, capable of detecting ENAs between  
 170 energies of 0.5–300 keV (Galli et al., 2022). Thus, ENA images taken by JUICE will pro-  
 171 vide a unique opportunity to understand the properties of Europa's and Callisto's plasma  
 172 interaction regions on a global scale, complementing in-situ plasma and magnetometer  
 173 observations.

## 174 1.2 Modeling ENA Emissions from Moon-Plasma Interactions

175 To provide context for the upcoming JUICE observations at Europa and Callisto,  
 176 Haynes et al. (2023) combined the three-dimensional electromagnetic field output from

177 the AIKEF hybrid model (thermal kinetic ions, fluid electrons; Müller et al., 2011) with  
 178 a tracing model for the energetic parent ions to calculate the ENA flux from charge ex-  
 179 change with these moons' atmospheres. ENA detectors aboard spacecraft have a lim-  
 180 ited angular field of view (FOV) and are point-like on the length scales of the plasma  
 181 interaction (e.g., Krimigis et al., 2004). Therefore, only a tiny fraction of the emitted ENA  
 182 population is sampled by an actual spacecraft instrument, and a large set of observations  
 183 from different vantage points is needed to capture the global emission morphology. To  
 184 obtain a global picture of the emitted ENA population, Haynes et al. (2023) generated  
 185 maps of the ENA flux through a hypothetical, concentric spherical detector around each  
 186 moon's neutral envelope. These maps reveal the locations on the detector sphere hit by  
 187 ENAs, independent of their velocity vectors at impact. Such a spherical ENA detector  
 188 records the *entire* ENA population leaving the moons' atmospheres, i.e., it captures the  
 189 global morphology of atmospheric ENA emissions detectable from outside the neutral  
 190 envelope. To assess the variability of ENA emissions at Europa and Callisto over a syn-  
 191 odic rotation, Haynes et al. (2023) considered two locations of each moon with respect  
 192 to Jupiter's magnetospheric plasma sheet: at the center and at maximum distance be-  
 193 low the center. By comparing the modeled maps of ENA flux through their spherical de-  
 194 tector in draped fields to those generated for uniform fields, the authors isolated which  
 195 features of the ENA emissions are caused by field perturbations from plasma interaction  
 196 currents.

197 At Europa and Callisto, Haynes et al. (2023) found that the majority of detectable  
 198 ENA emissions are focused into a band of high ENA flux centered around the great cir-  
 199 cle on the detector sphere that is perpendicular to the ambient magnetospheric field. With  
 200 changing distance between each moon and the center of the Jovian plasma sheet, this  
 201 band is rotated on the detector sphere according to the change in orientation of the am-  
 202 bient magnetospheric field vector. The fraction of observable ENA flux confined to the  
 203 band is controlled by the ratio of the energetic ion gyroradii to the moon's atmospheric  
 204 scale height: the more gyrations a parent ion can carry out within the atmosphere, the  
 205 greater the likelihood of it undergoing charge exchange and emitting an ENA into the  
 206 band. In the strong magnetospheric field at Europa, parent ions with pitch angles near  
 207  $90^\circ$  traverse a path through the atmosphere 10–100 times longer than those moving (largely)  
 208 along the magnetic field. Thus, over 80% of the observable ENA flux at Europa prop-  
 209 agates in planes nearly perpendicular to the magnetic field and contributes to the band.

At Callisto, the ambient magnetospheric field is 1–2 orders of magnitude weaker than at Europa, and the vast majority of parent protons can only complete partial gyrations within the atmosphere. As a result, the parent protons with pitch angles near  $90^\circ$  are less heavily “favored” for ENA production over the field-aligned particles at Callisto, compared to the case at Europa. Hence, only about 50–60% of the total ENA flux leaving Callisto’s atmosphere contributes to the band. Comparing ENA emissions in uniform versus draped fields, Haynes et al. (2023) found that the (partial) deflection of impinging parent ions by the field perturbations reduces the intensity in the band of elevated ENA flux at both moons regardless of the longitude on the detector sphere (Haynes et al., 2023).

Because they capture all of the detectable ENAs emitted from Europa’s or Callisto’s atmosphere, the global maps of ENA flux from Haynes et al. (2023) cannot be directly compared to actual ENA images taken by a spacecraft detector. An ENA detector is point-like on the length scales of the plasma interaction (e.g., Europa’s or Callisto’s radius) and has a limited FOV. Thus, at a given position, such an instrument would capture only a small fraction of the ENA flux which contributes to the global emission maps. Therefore, the physics encoded in the ENA emissions (readily accessible in the maps of Haynes et al., 2023) are deeply “encrypted” within ENA images of Europa and Callisto, to be captured during the JUICE mission (Grasset et al., 2013; Galli et al., 2022; Tosi et al., 2024). Hence, the analysis of such images requires a template for “decrypting” the physics contained in the observed ENA emissions.

Tippens et al. (2024) combined the three-dimensional structure of the draped fields from AIKEF and a particle tracing tool for the energetic parent ions to assemble synthetic ENA images for the upstream conditions observed during Cassini’s TA flyby of Titan. These authors employed a “backtracing” approach for calculating synthetic ENA images: their model initializes energetic parent ions at the positions where they emit ENAs into the detector, and evolves their trajectories backward in time (using a *negative* timestep). Thus, their model does not calculate any ion trajectories that, e.g., would never enter Titan’s atmosphere and emit an ENA toward the detector. Therefore, this approach is much more computationally efficient than, e.g., the global detector model of Haynes et al. (2023). After identifying which parent ion trajectories emit ENA flux into the detector, the model of Tippens et al. (2024) computes their contributions to the synthetic ENA image by treating their charge exchange interactions with Titan’s upper atmosphere. The

243 influence of field line draping on the structures in the synthetic ENA images produced  
 244 for TA was found to depend strongly on the detector's viewing geometry: the modifi-  
 245 cations introduced by draping are visible only from certain vantages, with no morpho-  
 246 logical differences in the synthetic ENA images between uniform and draped fields for  
 247 others. That is, *if* and *how* the draping of Saturn's magnetospheric field around Titan's  
 248 ionosphere is visible in synthetic ENA images depends on the location of the imaging  
 249 instrument and the pointing of its boresight vector (Tippens et al., 2024).

250 To date, no synthetic ENA images have been generated for Europa or Callisto. In  
 251 order to provide a forecast of upcoming ENA observations, we therefore proceed anal-  
 252 ogous to Tippens et al. (2024) and combine a backtracing tool for the energetic parent  
 253 ions with the three-dimensional electromagnetic fields from the AIKEF hybrid model.  
 254 For numerous viewing geometries at both moons, we compare synthetic ENA images gen-  
 255 erated for uniform and draped electromagnetic fields. In this way, we constrain which  
 256 positions and pointings of an ENA detector may allow for a global characterization of  
 257 the field perturbations in the vicinities of Europa and Callisto. More specifically, the goal  
 258 of this study is twofold: (i) we aim to catalog the morphology of atmospheric ENA emis-  
 259 sions to be detected by an ENA imager at Europa and Callisto, identifying the role of  
 260 field line draping in shaping these images. (ii) At both moons, we shall constrain the vari-  
 261 ability of the synthetic ENA images as a function of distance to the center of Jupiter's  
 262 plasma sheet.

263 The outline of this manuscript is as follows: in section 2, we provide an overview  
 264 of the parameters used in AIKEF to emulate the draped fields near Europa and Callisto.  
 265 We also describe the model employed to calculate synthetic ENA images at both moons.  
 266 In section 3, we discuss the morphology of the features seen in our synthetic ENA im-  
 267 ages, investigating how Europa's and Callisto's non-uniform electromagnetic environments  
 268 map into these images. We also probe the dependence of this effect on the viewing ge-  
 269 ometry. Finally, in section 4, we conclude with a brief summary of our major findings.

## 270 2 Modeling ENA Emissions at Europa and Callisto

271 In section 2.1, we provide a brief overview of the parameters used in the AIKEF  
 272 hybrid model to calculate the draped electromagnetic fields near Europa and Callisto.  
 273 In section 2.2, we describe the model used for generating synthetic ENA images at these

moons. Throughout this study, we employ the Cartesian Satellite Interaction System (SIS) with coordinates  $\mathbf{r} = (x, y, z)$  at each moon. This system originates at the center of Europa or Callisto, with the following unit vectors:  $\hat{\mathbf{x}}$  is aligned with the direction of corotational flow in our model,  $\hat{\mathbf{z}}$  is perpendicular to  $\hat{\mathbf{x}}$  and (approximately) aligned with Jupiter's spin axis, and  $\hat{\mathbf{y}} = \hat{\mathbf{z}} \times \hat{\mathbf{x}}$  bears roughly toward Jupiter, completing the system. The symbol  $R$  represents the radius of the respective moon, that is,  $R = R_C$  at Callisto and  $R = R_E$  at Europa.

## 2.1 Three-Dimensional Model of Europa's and Callisto's Electromagnetic Environments

In order to construct synthetic ENA images at Europa or Callisto, the 3D structure of these moons' electromagnetic environments must be known. We use the AIKEF hybrid model (Müller et al., 2011) to calculate the perturbations to the electric and magnetic fields near Europa and Callisto, generated by the interaction between the moons and the impinging thermal magnetospheric plasma. AIKEF has an extensive history of application at both Callisto (Liuzzo et al., 2015, 2016, 2017, 2018, 2019a, 2019b, 2022, 2024; Haynes et al., 2023) and Europa (Breer et al., 2019; Arnold et al., 2019; Arnold, Liuzzo, & Simon, 2020; Arnold, Simon, & Liuzzo, 2020; Addison et al., 2021, 2022, 2023, 2024; Haynes et al., 2023). For this study, we use the exact same electromagnetic field configurations as the preceding analysis of the global ENA emission morphology at Europa and Callisto by Haynes et al. (2023): these authors considered the moons' electromagnetic environments at the center of the Jovian magnetospheric plasma sheet as well as at maximum distance below it. At both of these locations, they took into account the draped fields from AIKEF and a “baseline” scenario that treats the fields near each moon as uniform. In the latter case, the magnetic field is set to the uniform magnetospheric background field  $\mathbf{B}_0$  at the moon's position, and the electric field is given by  $\mathbf{E}_0 = -\mathbf{u}_0 \times \mathbf{B}_0$ , where  $\mathbf{u}_0$  denotes the ambient plasma flow velocity. Thus, four distinct model scenarios for the fields are considered at both Europa and Callisto. The magnetospheric upstream conditions for these setups are summarized in Table 1 of Haynes et al. (2023). For a detailed justification of the chosen model parameters, we refer the reader to section 2.1 in that work. Visualizations of the draped fields for each AIKEF scenario are shown and discussed in section 3.1 of Haynes et al. (2023).

305        The dependence of the magnetospheric thermal ion density  $n_0$  on distance to the  
 306        center of Jupiter's plasma sheet follows a Gaussian distribution (e.g., Bagenal & Delamere,  
 307        2011). As a result, the upstream plasma density at both moons is smaller at their max-  
 308        imum distance below the Jovian plasma sheet, compared to the center. The bulk veloc-  
 309        ity  $\mathbf{u}_0$  of the impinging plasma is aligned with the (+x) axis, and it has a magnitude of  
 310         $|\mathbf{u}_0| = 100 \text{ km/s}$  at Europa and  $|\mathbf{u}_0| = 192 \text{ km/s}$  at Callisto (see Kivelson et al. (2004)  
 311        and section 2.1 of Haynes et al. (2023)). The magnetic environment of both moons may  
 312        be modified by an induction signal from a conducting subsurface ocean (Europa, Cal-  
 313        listo) or ionosphere (Callisto). In AIKEF, the induced field is treated as a dipole cen-  
 314        tered at the moon, and the strength of the induced magnetic moment is proportional to  
 315        the horizontal component of  $\mathbf{B}_0$  (see discussion of equation (1) in Haynes et al., 2023).  
 316        When Europa and Callisto are at maximum distance from the center of Jupiter's plasma  
 317        sheet,  $\mathbf{B}_0$  possesses three nonzero components, and the induced field is at its strongest.  
 318        In contrast, when each moon is at the center of the Jovian plasma sheet, the ambient  
 319        magnetospheric field  $\mathbf{B}_0$  is nearly anti-parallel to Jupiter's spin axis and no induced mag-  
 320        netic moment is included in our model.

321        At both moons, the atmospheric neutral density as a function of altitude is described  
 322        by a barometric law for each constituent. The AIKEF model also assumes Europa's and  
 323        Callisto's neutral envelopes to possess a ram-wake asymmetry: at both moons, the den-  
 324        sity of the neutral gas peaks at the ramside apex. At Europa, we include only the  $\text{O}_2$   
 325        component observed to dominate the atmosphere below altitudes of several hundred km  
 326        (Roth et al., 2016; Plainaki et al., 2018; Vorburger & Wurz, 2018). We use a scale height  
 327        of 100 km and a surface density of  $5.5 \cdot 10^{14} \text{ m}^{-3}$  at the ramside apex, which yields a  
 328        column density consistent with that derived from UV observations (Hall et al., 1995, 1998;  
 329        Roth et al., 2016). Cervantes and Saur (2022) found that the additional, localized bulge  
 330        of elevated  $\text{H}_2\text{O}$  density around the moon's subsolar or ramside apex (Roth, 2021) only  
 331        introduces very subtle modifications to Europa's electromagnetic environment. Besides,  
 332        the global ENA emission model of Haynes et al. (2023) revealed that the inclusion of this  
 333         $\text{H}_2\text{O}$  component does not generate any morphological changes to the global ENA emis-  
 334        sion pattern. For this reason, the atmospheric  $\text{H}_2\text{O}$  bulge is not included in our model.  
 335        At Callisto, we incorporate both the observed  $\text{CO}_2$  and  $\text{O}_2$  components of the atmosphere  
 336        (Carlson, 1999; Cunningham et al., 2015). To obtain column densities within the observed  
 337        range, we use a surface density (at the ramside apex) of  $1.0 \cdot 10^{15} \text{ m}^{-3}$  for molecular oxy-

338 gen and  $4.0 \cdot 10^{13} \text{ m}^{-3}$  for carbon dioxide, both with a scale height of 230 km (for fur-  
 339 ther details, see also Liuzzo et al., 2015). Our chosen value for Callisto's O<sub>2</sub> column den-  
 340 sity is approximately within a factor of 2 to a recent deduction using observations of the  
 341 moon's optical aurorae by the Hubble Space Telescope (de Kleer et al., 2023). In the AIKEF  
 342 model, Europa's atmosphere is partially ionized by electron impacts, whereas Callisto's  
 343 ionosphere is generated through a combination of solar UV ionization and electron im-  
 344 pact ionization (see Haynes et al., 2023, and references therein).

345       The model domain at Callisto is a cube centered at the moon with edges spanning  
 346  $-15R \leq x, y, z \leq 15R$ . At Europa, we use a cuboid which extends  $-8R \leq x \leq 22R$   
 347 in the corotation direction,  $-10R \leq y \leq 10R$  along the Europa-Jupiter line, and  $-30R \leq$   
 348  $z \leq 30R$  in the north-south direction. The extension of the model domain for each base-  
 349 line case (using uniform fields) is identical to that of the AIKEF domain at the respec-  
 350 tive moon.

## 351       2.2 Generating Synthetic ENA Images at Callisto and Europa

352       In order to generate synthetic ENA images that can guide the planning of ob-  
 353 servations, we must calculate the ENA flux entering a point-like (on length scales of the  
 354 plasma interaction) spacecraft detector with a finite field of view (FOV) for different elec-  
 355 tromagnetic environments at each moon. The model applied by Haynes et al. (2023) to  
 356 calculate the *global* ENA emission morphology is not suitable for this endeavor; the num-  
 357 ber of ENAs passing through any specific point (e.g., a spacecraft detector) in their sim-  
 358 ulation domain is near-zero. Thus, that model would require runtimes on the order of  
 359 several months to obtain even a single, smoothly resolved synthetic ENA image. For this  
 360 reason, we implement a “backtracing” method which initializes parent protons at the point  
 361 where they would emit an ENA into the detector, and evolves their trajectories back-  
 362 wards in time, i.e., with a *negative timestep* ( $\Delta t < 0$ ). Such an approach has already  
 363 been used to calculate synthetic ENA images that replicate key features of the Cassini  
 364 INCA observations from the spacecraft's first Titan flyby, TA (Tippens et al., 2024). Our  
 365 model framework adapts these authors' approach for use at Europa and Callisto. Be-  
 366 cause this method avoids calculating the trajectories of energetic parent protons that never  
 367 enter the moon's atmosphere or bear toward a pixel of the ENA detector, it can rapidly  
 368 generate synthetic ENA images. In the following, we provide an overview of this model's

369 major features. For a more detailed discussion of individual model elements, the reader  
 370 is referred to Tippens et al. (2024).

371 The energy range (for H: 0.5–300 keV) of the JENI instrument is already avail-  
 372 able in the peer-reviewed literature (Galli et al., 2022); however, parameters such as the  
 373 angular range of the FOV or the number of pixels in each direction are not yet exactly  
 374 specified (Mitchell et al., 2016). Therefore, the properties of the ENA detector in our  
 375 model are similar to those of the Ion and Neutral Camera (INCA) that was mounted upon  
 376 the Cassini spacecraft, which has flight-proven, publicly available capabilities (Mitchell  
 377 et al., 1993; Krimigis et al., 2004). In the model, the detector surface is represented by  
 378 a segment of a spherical cap, where the FOV spans 90° in azimuth and 120° in eleva-  
 379 tion. Each pixel has a different line of sight (LOS) that extends radially outward. The  
 380 position and orientation of the boresight vector and four corner pixels uniquely specify  
 381 the pointing of the model detector. The ENA flux detected by any pixel on the detec-  
 382 tor is given by the sum of the ENA flux contributions emitted by individual parent pro-  
 383 tons along its associated LOS.

384 Since ENAs travel (roughly) along straight lines, any parent proton that contributes  
 385 to the ENA image must possess a velocity vector which points toward the detector along  
 386 a LOS at a certain point in time. Any LOS that does not intersect the atmosphere is  
 387 assigned zero ENA flux. For pixels that face the atmosphere, the LOS is extended un-  
 388 til it encounters the far boundary of the neutral envelope or the surface of the moon. Fig-  
 389 ure 1 displays a schematic of this backtracing technique, with the straight black line il-  
 390 lustrating a LOS. For a LOS which intersects the surface of the moon, only the ENAs  
 391 produced along the LOS segment *between* the moon and the detector can contribute to  
 392 the flux into the corresponding pixel. As shown in Figure 1, the interval of each LOS within  
 393 the atmosphere is discretized into segments of length  $\Delta\ell$ . The value of  $\Delta\ell$  is chosen to  
 394 be shorter than the atmospheric scale height at the respective moon: we set  $\Delta\ell = 0.015R$   
 395 in both cases (where  $R = R_E$  at Europa and  $R = R_C$  at Callisto). This value corre-  
 396 sponds to a segment length of  $\Delta\ell = 23.4$  km at Europa and  $\Delta\ell = 36.2$  km at Callisto.  
 397 Since the atmospheric scale height in our model is 230 km =  $0.095R$  at Callisto and 100 km =  
 398  $0.064R$  at Europa,  $\Delta\ell$  comfortably resolves this length scale at both moons.

399 ENA imaging instruments such as INCA and JENI cannot provide each ENA’s ex-  
 400 act kinetic energy due to downlink limitations. Their full sensitivity range is rather de-

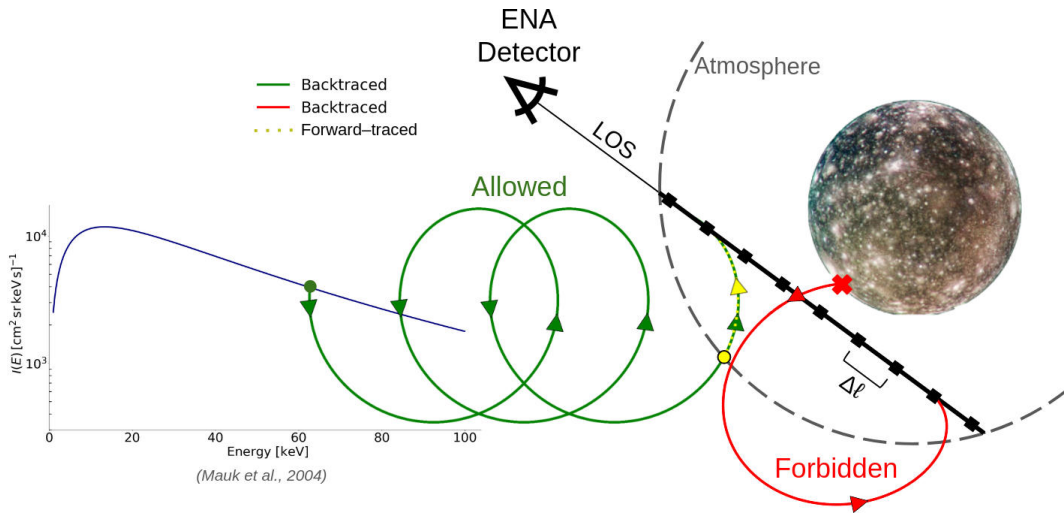


**Figure 1.** Depiction of the backtracing model used to calculate synthetic ENA images of the magnetosphere-atmosphere interactions at Europa and Callisto (adapted from Tippens et al., 2024). The eye-like element corresponds to the ENA detector. The black line emanating from the ENA detector represents a sample line of sight (LOS). The interval of the LOS within the moon’s atmosphere (thick black line) is discretized into segments of length  $\Delta\ell$ . The red and green curves represent respective “forbidden” and “allowed” trajectories of parent protons backtraced from a LOS segment to determine the ambient intensity, with the arrowheads denoting their instantaneous velocity vectors. The observed intensity distribution  $I(E)$  of the ambient energetic proton flux (blue curve) is sampled at the energy  $E$  of the parent proton (with an allowed trajectory) when it reaches the uniform fields outside of the moon’s interaction region. Subsequently, any proton with an allowed trajectory is returned to the top of the atmosphere (yellow dot) and traced forward in time to calculate ENA generation (yellow, dotted line).

composed into several energy channels, usually spanning tens of keV (e.g., Krimigis et al., 2004; Mitchell et al., 2005). The intensity of atmospheric ENA emissions is maximized at parent proton energies  $E$  between 10 keV and 40 keV at Callisto and between 40 keV and 70 keV at Europa. At both moons, the ENA flux emitted from the atmosphere falls off above and below these energies (Haynes et al., 2023). Building upon this result, our model detector measures the ENA flux in a (hypothetical) energy channel  $5 \text{ keV} \leq E \leq 75 \text{ keV}$  that captures the peak energy of ENA emissions at *both* Europa and Callisto. Using the same energy range at both moons also allows for direct comparison of the synthetic ENA images, thereby facilitating the identification of common physical processes that shape the image morphology. Since the gyroradius of a proton grows by a

411 factor of  $\sqrt{15}$  from 5 keV to 75 keV, we segment this energy channel into eight linearly  
 412 equidistant parent proton (and associated ENA) energies  $E_j$  such that  $E_j = 5 \text{ keV} +$   
 413  $j \cdot 10 \text{ keV}$ , where  $j \in \{0, \dots, 7\}$ . The initial energy  $E_j$  assigned to each backtraced par-  
 414 ent proton (mass  $m_p$ ) when launched from a LOS determines its speed  $|\dot{\mathbf{r}}| = \sqrt{2E_j/m_p}$   
 415 at the launch point. Because an ENA emitted into the detector has the same velocity  
 416 vector as its parent proton at the moment of charge exchange, the backtraced proton is  
 417 given an initial velocity  $\dot{\mathbf{r}}$  that points toward the detector. Charge exchange interactions  
 418 only result in ENA production if the energetic parent ion is singly charged. Analogous  
 419 to Haynes et al. (2023), we consider only ENA production by energetic magnetospheric  
 420 protons. Given the large number of cases that need to be analyzed for protons alone, we  
 421 refrain from including the two heavier ion species (sulfur and oxygen) in this study.

422 From the center of each LOS segment  $\Delta\ell$  within the atmosphere, eight parent pro-  
 423 tons at energies  $E_j$  (where  $j \in \{0, \dots, 7\}$ ) are launched and traced backwards in time,  
 424 i.e., with a negative timestep  $\Delta t < 0$ . The backtracing process does not consider any  
 425 interactions between protons and neutral gas, and no ENAs are produced yet. This pro-  
 426 cedure is used exclusively to identify parent protons that contribute to the synthetic ENA  
 427 image. The magnitude of their contributions is determined in a subsequent step of the  
 428 model. Parent protons are traced until they either (a) impact the moon, or (b) reach the  
 429 undisturbed plasma at the outer faces of the model domain. Fate (a) represents a “for-  
 430 bidden” trajectory; when traced forward in time ( $\Delta t > 0$ ), such a parent proton would  
 431 have to travel through the solid body of the moon in order to reach its launch point on  
 432 the LOS (e.g., red trajectory in Figure 1). Ions which take forbidden trajectories are deleted  
 433 from the model and contribute no flux to the synthetic ENA image. In other words, the  
 434 model does not consider ENA generation through surface sputtering (Pontoni et al., 2022;  
 435 Szabo et al., 2024). At both moons, a backtraced proton may travel along Jovian mag-  
 436 netospheric field lines out of the local interaction region, bounce at its mirror point, and  
 437 return to Europa’s or Callisto’s immediate environment. In the forward-tracing picture,  
 438 the distance downstream (i.e., in positive  $x$  direction) where bouncing protons at ener-  
 439 gies  $E \leq 75 \text{ keV}$  would return to the interaction region is larger than  $30R_C$  at Callisto  
 440 (Liuzzo et al., 2019b) and exceeds  $10R_E$  at Europa (Paranicas et al., 2009; Nordheim  
 441 et al., 2022). Therefore, such bouncing protons cannot hit the moon’s surface upon re-  
 442 turn and become “forbidden”. Rather, they fall into category (b).

Fate (b) corresponds to an “allowed” trajectory, that is, a parent proton which propagates forward in time ( $\Delta t > 0$ ) from the ambient magnetospheric plasma and reaches its launch point on the LOS (e.g., green trajectory in Figure 1). In the considered energy range, the gyroradii  $r_g$  for energetic parent protons at Europa always satisfy  $r_g \ll R_E$ . The largest gyroradii of parent protons in our model ( $r_g \approx 4.10 R_C$ ) occur at  $E_7 = 75$  keV in the weak magnetospheric field near Callisto ( $|\mathbf{B}_0| = 4$  nT) when located at the center of Jupiter’s plasma sheet. Even this value of  $r_g$  is less than half of the distance between the outer faces of the model domain and the surface of the moon ( $14 R_C$ , see also section 2.1 and Haynes et al., 2023). Thus, a parent proton that reaches an outer face of the model domain at Europa or Callisto cannot return to hit the surface —neither through gyration nor through bouncing— and possesses an allowed trajectory.

The energetic magnetospheric protons in the model are treated as macroparticles, each of them representing the differential flux carried by a large number of real protons. For each allowed proton trajectory, the energetic ion spectrum  $I(E)$  observed outside of the moon’s interaction region (blue curve in Figure 1) is sampled at the energy  $E$  of the parent proton when reaching the outer faces of the model domain. In general, the value of  $E$  is different from the proton’s energy  $E_j$  at launch: along its trajectory, the particle is accelerated by the fields. We adopt the approach of Haynes et al. (2023), Addison et al. (2021, 2022), and Liuzzo et al. (2022) and use the spectra  $I(E)$  observed by the Galileo and Juno spacecrafts during their flybys of both moons. Paranicas et al. (2002) give the ambient energetic proton spectra sampled near Europa during the E12 and E26 flybys. These encounters occurred when the moon was at the center of and near maximum distance below the Jovian plasma sheet, respectively. When Callisto is located at the center of the sheet, we utilize the energetic proton spectrum from Mauk et al. (2004), labeled G8 PS/A in their study. At Callisto’s maximum excursion below the sheet, we use the same spectrum downscaled by a factor of 10 at all energies (for further justification, see Liuzzo et al., 2022; Haynes et al., 2023).

Galileo measured the pitch angle distribution (PAD) of energetic protons outside of Europa’s interaction region, and Mauk et al. (2004) determined it to be isotropic to within 25%. However, Juno measurements of the proton PAD at Europa’s orbit revealed a field-aligned distribution, with about 50% more flux at pitch angles of  $\alpha = 0^\circ$  or  $\alpha = 180^\circ$  than at  $\alpha = 90^\circ$  (Sarkango et al., 2023). The global ENA model of Haynes et al. (2023) revealed that intensity distribution of ENA flux through a spherical detector around

476 Europa remains qualitatively unchanged when including such a field-aligned PAD instead  
 477 of an isotropic PAD. Their results show that the effect of the anisotropic PAD is largely  
 478 quantitative, altering the emission pattern by no more than 25% at any location on the  
 479 detector sphere. At Callisto's orbital distance, Galileo observations show that the en-  
 480 ergetic proton PAD for  $5 \text{ keV} \leq E \leq 75 \text{ keV}$  is largely isotropic (Mauk et al., 2004);  
 481 this is further corroborated by Juno observations of the  $E = 117 \text{ keV}$  proton PAD in  
 482 the same region (Shen et al., 2022). In our study, we treat the PAD of the impinging pro-  
 483 tons at both moons as isotropic. However, investigating the influence of anisotropies in  
 484 the PAD on synthetic ENA images may constitute a valuable follow-up study.

485 Each backtraced parent proton with an allowed trajectory is assigned an initial dif-  
 486 ferential flux  $J_I = I(E)$  by sampling the ambient distribution (blue curve in Figure 1).  
 487 To calculate such a parent proton's production of ENAs, we follow its (previously cal-  
 488 culated) trajectory from the outer faces of the model domain to the top of the moon's  
 489 atmosphere at  $|\mathbf{r}| = 2R$  (yellow point in Figure 1) in *forward time*, that is, with  $\Delta t >$   
 490 0. Only a tiny fraction of the atmospheric neutral gas is located above this altitude, and  
 491 hence, ENA emissions at  $|\mathbf{r}| > 2R$  can safely be neglected (Haynes et al., 2023). For  
 492 an isotropic PAD, the macroparticle's flux  $J_I$  at the outer faces of the model domain is  
 493 related to its flux at the top of the atmosphere  $J_\tau$  via

$$J_\tau = \frac{E_\tau}{E_I} J_I \quad , \quad (1)$$

494 where  $E_I$  and  $E_\tau$  are its energies at these two locations (Kollmann et al., 2019; Haynes  
 495 et al., 2023; Tippens et al., 2024). This relationship follows from the conservation of phase  
 496 space density in collisionless environments (Liouville's Theorem), i.e., it is valid as long  
 497 as the proton macroparticle travels *outside* of Europa's or Callisto's atmosphere. Equa-  
 498 tion (1) is also applied to update a parent proton's differential flux when gyration causes  
 499 it to veer out of and subsequently re-enter the atmosphere. For example, when Callisto  
 500 is located near the center of the Jovian plasma sheet, large gyroradii allow the parent  
 501 protons to leave and re-enter the moon's neutral envelope many times (see Figure 13 in  
 502 Haynes et al., 2023).

503 With the parent proton's differential flux (i.e., its numerical "weight")  $J_\tau$  at the  
 504 top of the atmosphere determined by equation (1), we subsequently model its produc-  
 505 tion of ENAs. This step relies on the highly forward-scattered nature of charge exchange:  
 506 in the energy range considered, a proton macroparticle loses only around 1 eV during such

507 an interaction (e.g., Lindsay & Stebbings, 2005), a mere 0.02% of even the smallest con-  
 508 sidered energy at launch ( $E_0 = 5$  keV). Thus, energy loss due to charge exchange does  
 509 not appreciably change a proton macroparticle’s trajectory, and the trajectory backtraced  
 510 from the launch point ( $\Delta t < 0$ ) is identical to the proton’s forward-traced trajectory  
 511 as it generates ENAs in the atmosphere ( $\Delta t > 0$ ). Starting from the top of the atmo-  
 512 sphere (yellow dot in Figure 1), we follow the parent proton with a positive timestep ( $\Delta t >$   
 513 0) along its path within the neutral envelope (dotted yellow trajectory segment in Fig-  
 514 ure 1) to calculate the attenuation  $\Delta J$  of its differential flux  $J$ , described by

$$\Delta J = -J \sigma(E) n_n(\mathbf{r}) |\Delta \mathbf{s}| \quad , \quad (2)$$

515 analogous to the approach of Wulms et al. (2010), Kabanovic et al. (2018), Tippens et  
 516 al. (2022, 2024) and Haynes et al. (2023). In equation (2),  $n_n(\mathbf{r})$  is the neutral density  
 517 at the proton’s position  $\mathbf{r}$ , the step length reads  $\Delta \mathbf{s} = \dot{\mathbf{r}} \Delta t$ , and  $\sigma(E)$  is the energy-  
 518 dependent cross section for charge exchange between protons and atmospheric neutrals  
 519 (Lindsay & Stebbings, 2005).

520 Along the segment of the parent proton’s trajectory within the atmosphere, its nu-  
 521 matical weight  $J$  is continuously attenuated according to equation (2). One ENA is pro-  
 522 duced during each timestep  $\Delta t > 0$ , with the ENA “yield” (i.e., differential flux rep-  
 523 resented by the ENA) in each timestep given by  $Y = -\Delta J$  (Haynes et al., 2023). Each  
 524 ENA is created with a velocity vector equal to the momentary velocity of the parent pro-  
 525 ton. The ENA produced when the parent proton ultimately returns to its launch point  
 526 is the lone one emitted along the chosen LOS into the detector. Only this ENA contributes  
 527 to the synthetic image; the ENAs produced earlier are discarded. We use the same at-  
 528 mospheric O<sub>2</sub> profiles for ENA generation as included in AIKEF at each moon (see sec-  
 529 tion 2.1). Analogous to Haynes et al. (2023), the ENA production model does not in-  
 530 corporate charge exchange between energetic protons and the CO<sub>2</sub> component of Cal-  
 531 listo’s atmosphere; the CO<sub>2</sub> column density is a factor of 25 below that of molecular oxy-  
 532 gen (Carlson, 1999). Since the cross sections for charge exchange with CO<sub>2</sub> are only a  
 533 factor of 2–3 larger than those for O<sub>2</sub> at a given energy (Lindsay et al., 2005), our model  
 534 does not take into account the CO<sub>2</sub> contribution to the ENA images. Subsequent reion-  
 535 ization and renaturalization of the ENAs after their creation is not considered in our model.  
 536 Since several authors were able to reproduce the INCA observations from the TA Titan  
 537 flyby without treating this effect (Wulms et al., 2010; Kabanovic et al., 2018; Tippens  
 538 et al., 2024), we defer such an expansion of the model to a future study.

Analogous to Tippens et al. (2024), the total ENA flux into the pixel at the base of each LOS is determined by summing the contributions from each parent proton energy  $E_j$  at each segment  $\Delta\ell$ , and then summing the contributions for all segments along that LOS (see equations (7) and (8) in that study). This procedure is carried out for each pixel. Finally, the synthetic ENA image is constructed like a mosaic using the calculated ENA flux emitted into each individual pixel. The process to generate a synthetic ENA image is summarized by the flowchart in Figure 2. To facilitate comparison between the synthetic ENA images and actual observations by a spacecraft imager, we carry out the same two post-processing steps on the synthetic images as Tippens et al. (2024). First, the images are downscaled to the  $32 \times 32$  pixel grid of the INCA detector, corresponding to an angular resolution of  $3.75^\circ \times 2.81^\circ$  (e.g., Krimigis et al., 2004). The angular resolution of the detector in our model is  $1^\circ$  in both azimuth and elevation. The downscaling process mimics the nature of the larger pixels on a real ENA detector: unlike the pixels in our model, each pixel of an actual instrument can detect incoming ENAs within a small cone of velocity vectors around the associated LOS (see section 2 of Tippens et al., 2024, for details). While the angular resolution of JENI is not yet available in the peer-reviewed literature, the targeted value of  $2^\circ$  per pixel is substantially higher than that of INCA (Mitchell et al., 2016). Since the synthetic images are generated at an angular resolution well below even this targeted value, it is readily possible to downscale our results onto the pixel grid of JENI once its parameters are available. The downscaling procedure does not introduce any morphological changes to the the synthetic ENA images, but only slightly blurs them.

Second, a point spread function (PSF) is applied to account for the slight “bleed-over” of the ENA flux emitted toward a certain pixel into adjacent pixels. This effect is caused by scattering of incident ENAs from the foils within the instrument (Krimigis et al., 2004). Due to its thinner foils, this effect is expected to be significantly less for JENI than for INCA (Mitchell et al., 2016). For the INCA instrument, the PSF is a product of two Gaussian distributions specified by the standard deviations in azimuthal and elevational directions (Krimigis et al., 2004). Within the range of values available in the literature, the choice of these standard deviations has little influence on the features visible in the synthetic ENA image: the PSF only slightly smears out the ENA signal across adjacent pixels (see also Tippens et al., 2024). In this study, we use values for the standard deviations provided by Dialynas et al. (2013); see also Table 2 in Tippens et al. (2024).

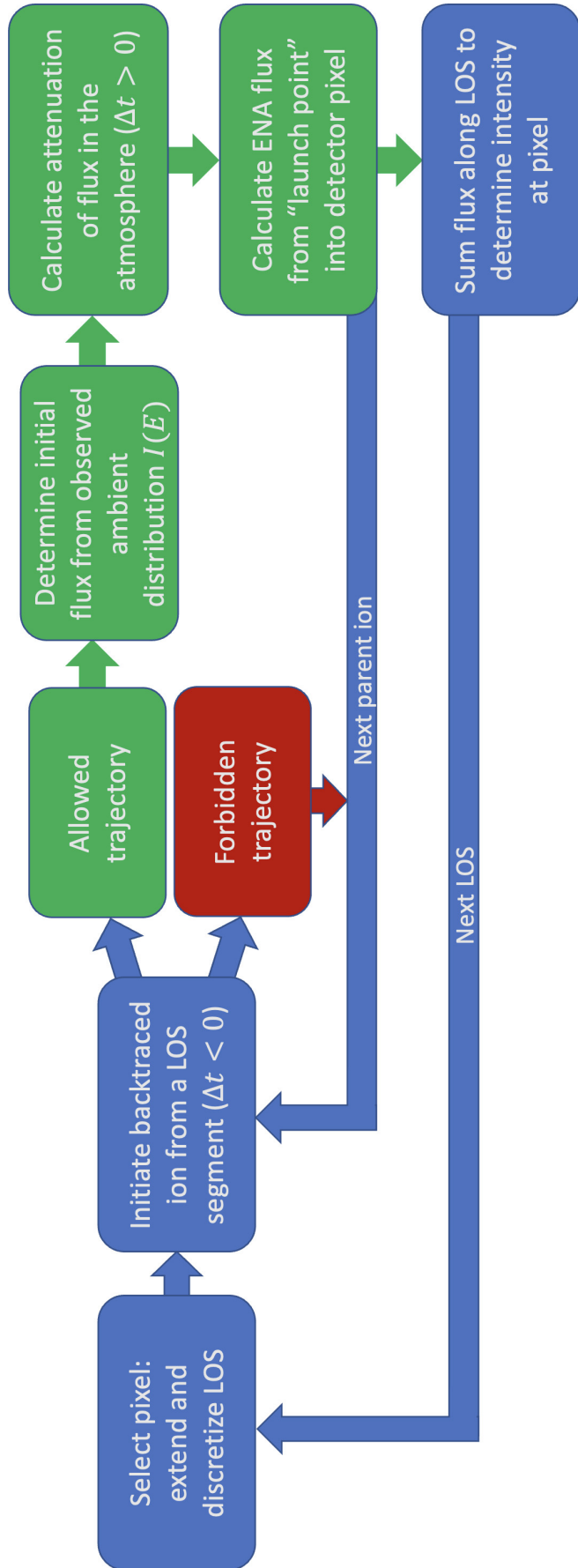


**Figure 2.** Logical structure of the backtracing model used to calculate synthetic ENA images at Europa and Callisto (adapted from Tippens et al., 2024).

For Europa and Callisto, we generate a set of synthetic ENA images sampling a multitude of viewing directions for uniform and draped fields, both at the center and at maximum distance below Jupiter's magnetospheric plasma sheet. We consider six detector positions, all located at a distance of  $3R$  from the center of each moon, with the boresight vector pointing radially inward: the detector is placed above the upstream  $(-3R, 0, 0)$  and downstream  $(3R, 0, 0)$  apices, the Jupiter-averted  $(0, -3R, 0)$  and Jupiter-facing  $(0, 3R, 0)$  apices, and the north  $(0, 0, 3R)$  and south  $(0, 0, -3R)$  poles. When Europa and Callisto are at the center of the Jovian plasma sheet, the magnetospheric background field  $\mathbf{B}_0$  is taken to be southward (see section 2.1). In this case, the detectors at  $(0, 0, \pm 3R)$  look along or anti-parallel to  $\mathbf{B}_0$ , and the boresight vectors of the other four detectors are oriented perpendicular to  $\mathbf{B}_0$ . In contrast, when each moon is at its maximum distance below the center of the Jovian plasma sheet, the ambient field  $\mathbf{B}_0$  possesses non-negligible components along all three axes of the SIS. Due to the nearly perpendicular inclination of  $\mathbf{B}_0$  against the north-south axis when Callisto is at maximum distance below the sheet, we consider four additional viewing geometries relative to  $\mathbf{B}_0$  in this case. These four model detectors are again positioned at a distance of  $3R$  from the center of Callisto, looking radially toward its center. In two of these setups, the detector is positioned on the straight line through the center of the moon that is parallel to  $\mathbf{B}_0$ ; the detector's boresight is oriented parallel or anti-parallel to  $\mathbf{B}_0$ . In the other two setups, the detector is contained in the plane through the center of Callisto that is perpendicular to  $\mathbf{B}_0$ : specifically, we place the detector on the intersection of this plane and the  $y = 0$  plane. At Europa, we do not consider the analogous detector configurations since the ambient field  $\mathbf{B}_0$  remains southward to within  $28.5^\circ$  even at maximum distance below the plasma sheet.

Because the path length  $|\Delta\mathbf{s}|$  in equation (2) is proportional to the timestep ( $\Delta\mathbf{s} = \dot{\mathbf{r}} \Delta t$  where  $\Delta t > 0$ ), the choice of  $\Delta t$  maps into the intensity of ENA emissions in the synthetic images. Our model utilizes the *same* timestep everywhere within the atmosphere: this ensures that the “brightness” of the synthetic ENA image is scaled by the same factor  $\Delta t$  at each pixel. Due to the degree of freedom introduced by the choice of  $\Delta t$ , the absolute “brightness” of our synthetic ENA images cannot be determined through this model. However, since the same timestep is used everywhere inside the atmosphere, the *relative* intensities of features in the ENA images can be constrained by our method. In other words, our approach can predict the *morphology* of the ENA images expected at Europa or Callisto. Once a single ENA image has been taken by a spacecraft at ei-

ther of these moons, the timestep in our model can be calibrated to reproduce the observed brightness and to make quantitative predictions of absolute fluxes for subsequent encounters. For Titan, this has been successfully demonstrated by Tippens et al. (2024). Everywhere outside the atmosphere, we apply a value of  $\Delta t = T_{g0}/100$ , where  $T_{g0} = 2\pi m_p/(e|\mathbf{B}_0|)$  is the gyroperiod of a proton in the undisturbed background field  $\mathbf{B}_0$ . Within Europa's or Callisto's atmosphere, we use a timestep of  $\Delta t = T_{g0}/1000$ . This choice ensures that the distance traveled by a proton during each timestep remains below the atmospheric scale height at either moon. Even for Callisto at the center of Jupiter's plasma sheet (where the gyroperiod is the longest), the largest possible distance traveled during a timestep,  $|\Delta \mathbf{s}| = |\dot{\mathbf{r}} \Delta t| \approx (\sqrt{2E_7/m_p})(T_{g0}/1000)$ , is still only about 62 km, around a quarter of the atmospheric scale height used in our model.

### 616 3 Results and Discussion

#### 617 3.1 Analysis of Synthetic ENA Images at Callisto

##### 618 3.1.1 Callisto at the Center of the Jovian Plasma Sheet

619 Figure 3 depicts synthetic ENA images at Callisto when the moon is at the center  
 620 of the Jovian plasma sheet. We consider six viewing geometries, represented by the  
 621 gray detector elements. Panels (a)–(f) each show the synthetic ENA images in uniform  
 622 fields (left) and in draped fields (right), all with increasing detector *elevation* on the hor-  
 623 izontal axis and decreasing detector *azimuth* on the vertical axis. This “landscape” ar-  
 624 rangement of the image frames is consistent with the approach frequently used to dis-  
 625 play INCA observations from Cassini's Titan flybys (e.g., Mitchell et al., 2005; Brandt  
 626 et al., 2012; Tippens et al., 2024), where the detector's FOV is rotated by 90° clockwise  
 627 about the boresight from the “portrait” orientation suggested by the detector coordi-  
 628 nate system. For each detector position, the boresight vector is aligned with an axis of  
 629 the Satellite Interaction System. Panels 3(a) and 3(d) use the detector placed on the  $x$   
 630 axis at  $(\mp 3R_C, 0, 0)$ . Panels 3(b) and 3(e) display synthetic ENA images with the de-  
 631 tector positioned along the  $y$  axis at  $(0, \mp 3R_C, 0)$ ; panels 3(c) and 3(f) have the detec-  
 632 tor on Callisto's north-south axis, placed at  $(0, 0, \mp 3R_C)$ . The boresight vector always  
 633 points radially toward the center of the moon.

634 In uniform fields, the synthetic ENA images taken north and south of Callisto ( $z =$   
 635  $\pm 3R_C$ ) both show a ring of elevated ENA flux surrounding the limb of the moon (left

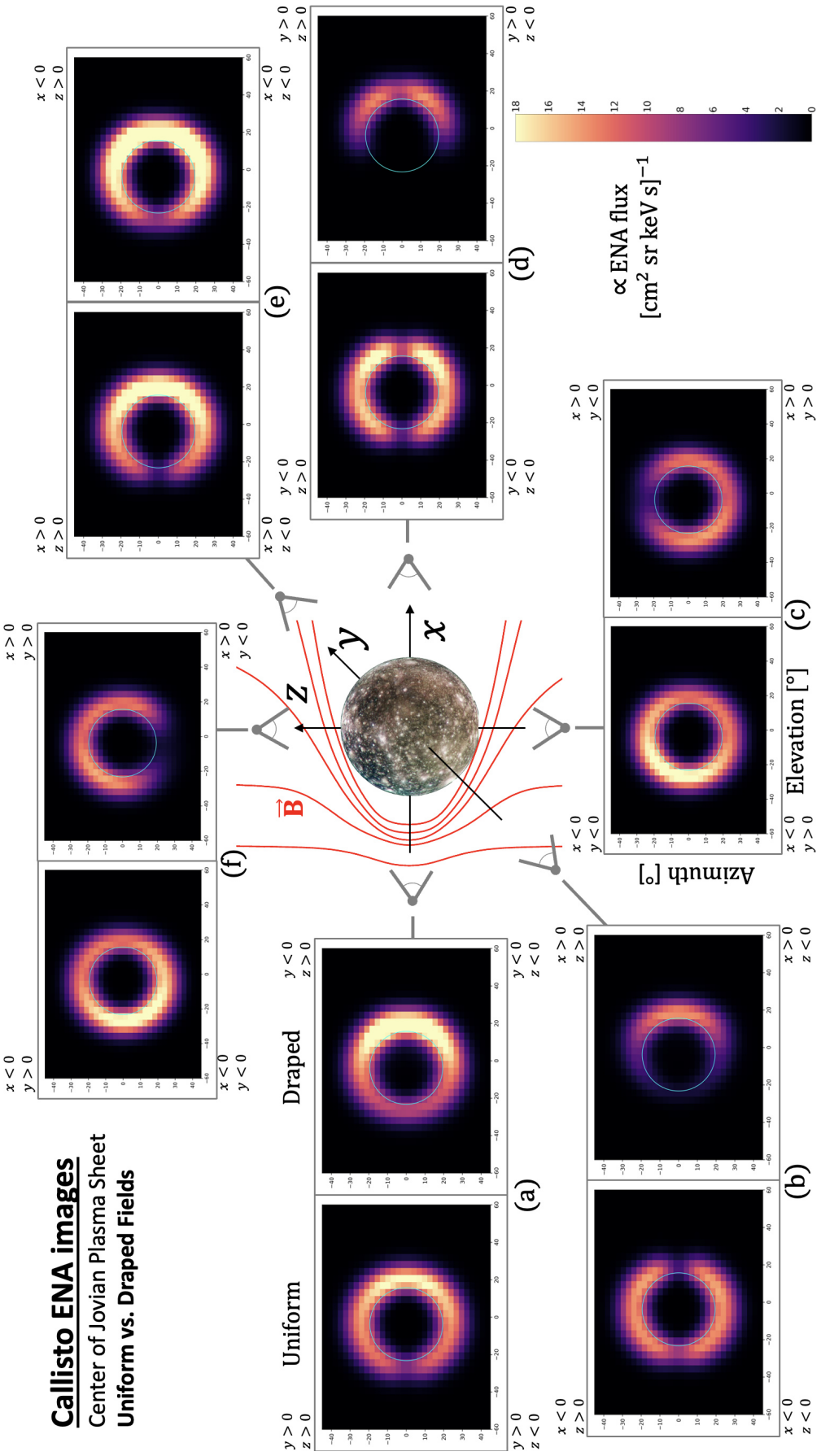


**Figure 3.** Synthetic ENA images in uniform and draped fields at Callisto when the moon is near the center of the Jovian plasma sheet. In each panel, synthetic ENA images are arranged with detector elevation on the horizontal axis and detector azimuth on the vertical axis for both uniform (left) and draped (right) magnetospheric fields. A depiction of the draped magnetic field lines near Callisto is included in red; the ambient magnetospheric field in this configuration is oriented southward. In each synthetic ENA image, the disc of the moon is represented by the light blue circle. Every panel is connected to a gray detector symbol that illustrates the viewing geometry used to create the respective images. For each of the six setups, the model detector is placed at  $2R_C$  altitude and the bore sight vector points toward the center of Callisto: in panel (a), the detector points in  $(+x)$  and is located at  $(-3R_C, 0, 0)$ ; in panel (b), the detector points in  $(+y)$  and is located at  $(0, -3R_C, 0)$ ; in panel (c), the detector points in  $(+z)$  and is located at  $(0, 0, 3R_C)$ ; and in panel (d), the detector points in  $(-x)$  and is located at  $(0, 3R_C, 0)$ ; and in panel (e), the detector points in  $(-y)$  and is located at  $(0, 0, -3R_C)$ . The labels in the four corners of each panel indicate which region of the Satellite Interaction System corresponds to the associated quadrant of the images. The values of the ENA flux for our choice of  $\Delta t$  (see section 2.2) are indicated by the color bar in the bottom right-hand corner, where bright yellow corresponds to an intense signal, and black corresponds to none.

sub-panels in Figures 3(c) and 3(f)). The left side of each image displays ENA flux emanating from the atmosphere above Callisto's disc in the  $x < 0$  half space, and the right side depicts ENA flux from the  $x > 0$  half space. The top half of the images in Figure 3(c) shows the FOV segment that receives flux from the Jupiter-averted half space, and the bottom half corresponds to the Jupiter-facing half space. In Figure 3(f), the locations of the Jupiter-facing and Jupiter-averted half spaces are flipped, with the top half now corresponding to  $y > 0$ . The ENA flux emitted by a parent proton at a certain point on a LOS is proportional to the local atmospheric density (see equation 2), so the highest ENA fluxes are recorded by pixels looking just outside of the moon's disc where the associated LOS column contains the most neutral gas. For such a LOS, its path length through the atmosphere is also maximized compared to one intersecting Callisto's surface or passing the disc at higher altitudes. The scale height of Callisto's atmosphere in our model is approximately  $0.1R_C$ , which would correspond to only a pixel or two in radial extent from the disc of the moon. However, these rings appear to span multiple scale heights in the images from Figures 3(c) and 3(f): this broadening is caused by the application of the PSF, which slightly spreads the ENA flux from the pixels near the moon's surface to neighboring ones (see also Tippens et al., 2024).

At the center of the Jovian plasma sheet, the magnetospheric field  $\mathbf{B}_0$  near Callisto is oriented southward (see Table 1 of Haynes et al., 2023). At the moment of charge exchange, parent protons must have velocity vectors which are nearly aligned or anti-aligned with  $\mathbf{B}_0$  to contribute to the ring of elevated ENA flux observed from south and north of the moon (left images in Figures 3(c) and 3(f), respectively). Since ENA generation mainly occurs within one atmospheric scale height of Callisto's surface (Haynes et al., 2023), the angle between a (uniform) magnetospheric field line and such a parent proton's velocity vector  $\xi_C$  falls within a range of approximately

$$\xi_C \in \left\{ \arcsin\left(\frac{R_C}{3R_C}\right), \arcsin\left(\frac{R_C + 0.1R_C}{3R_C}\right) \right\} \approx \{19.5^\circ, 21.5^\circ\} , \quad (3)$$

where  $0.1R_C$  is the atmospheric scale height in our model (see section 2.1) and  $3R_C$  is the distance between the detector and the moon's center. Hence, the lines of sight which constitute the ring in both Figure 3(c) and Figure 3(f) are confined between two cones with apices at the detector, axes aligned with the boresight vector, and opening angles of  $19.5^\circ$  and  $21.5^\circ$ .

666 Protons with velocity vectors outside this cone also produce ENAs. However, these  
 667 cannot be observed by the detectors in Figures 3(c) and 3(f). In uniform fields, parent  
 668 protons contributing to the ring in panel 3(c) must have pitch angles of  $\alpha \approx \xi_C$ , i.e.,  
 669 they mainly approach Callisto from the north. Likewise, protons contributing to the ring  
 670 in panel 3(f) must have pitch angles of  $\alpha \approx 180^\circ - \xi_C \approx 158.5^\circ$ , indicating they ap-  
 671 proach the moon from the south. The angle  $\xi_C$  thus determines the angular size of the  
 672 ring in the synthetic ENA images. In Figures 3(c) and 3(f), the ring of high ENA flux  
 673 intersects the azimuth axis (i.e., where elevation is  $0^\circ$ ) between angles of  $\pm(21^\circ - 26^\circ)$ ,  
 674 similar to the value predicted by expression (3). This estimation does not take into ac-  
 675 count the  $\mathbf{E}_0 \times \mathbf{B}_0$  drift velocity: even for parent protons at the lower bound of our en-  
 676 ergy range ( $E_0 = 5$  keV), the  $\mathbf{E}_0 \times \mathbf{B}_0$  drift speed is at least four times slower than their  
 677 translation and/or gyration velocities  $\sqrt{2E_0/m_p}$  (see also Haynes et al., 2023).

678 In uniform fields, the ENA flux intensity within the rings in Figures 3(c) and 3(f)  
 679 peaks at the upstream apex and decreases by 40%–50% moving toward the downstream  
 680 apex along Callisto’s Jupiter-facing and Jupiter-averted flanks. This decrease is caused  
 681 by the ram-wake asymmetry in the moon’s atmospheric O<sub>2</sub> density: as described by equa-  
 682 tion (3) of Haynes et al. (2023), the O<sub>2</sub> number density peaks at the ramside apex and  
 683 decreases with angular distance when moving toward the wakeside. When approaching  
 684 the wakeside apex, the atmospheric density in the model drops rapidly to zero (see also  
 685 Liuzzo et al., 2015, for further discussion). However, no corresponding gap in ENA flux  
 686 is formed above the wakeside apex. A LOS which intersects this region also extends through  
 687 portions of Callisto’s atmosphere *outside* the  $z = 0$  plane where the atmospheric den-  
 688 sity does not vanish; parent protons entering such regions contribute to the ENA flux  
 689 observed above the wakeside apex of the moon’s disk in uniform fields (Figures 3(c) and  
 690 3(f)). Furthermore, a possible gap in ENA flux above the wakeside apex would be par-  
 691 tially repopulated by flux from neighboring pixels through application of the PSF.

692 For all six viewing geometries, the ENA flux into the detector drops to zero for pix-  
 693 els *inside* the disc of the moon (i.e., the light blue circle; see Figure 3). The mechanism  
 694 responsible for producing this depletion is distinct between ENA images taken by a de-  
 695 tector in the  $z = 0$  plane (panels 3(a), 3(b), 3(d), 3(e)) and those with the detector po-  
 696 sitioned at  $z = \pm 3R_C$  (panels 3(c), 3(f)). For the latter, the velocity vectors of any par-  
 697 ent protons which could populate Callisto’s disc with ENA flux are largely anti-aligned  
 698 or aligned with the ambient magnetic field, to within  $19.5^\circ$  (the lower threshold for  $\xi_C$ ,

see expression (3)). Any hypothetical ENAs reaching the detector at  $(0, 0, \pm 3R_C)$  within Callisto's disc would have to be produced on the opposite side of the moon, traveling inside a cone with its apex at the detector and an opening angle of  $19.5^\circ$ . However, such a cone is "corked" by the body of Callisto; that is, any ENAs emitted along a LOS *inside* this cone impact the moon before reaching the detector. In consequence, there is no ENA flux emitted along lines of sight which intersect Callisto's disc in panels 3(c) and 3(f).

In contrast, for the detector locations in the  $z = 0$  plane (left images in Figures 3(a), 3(b), 3(d), and 3(e)), the boresight vectors are *normal* to the (uniform) ambient field  $\mathbf{B}_0$ . Similar to Figures 3(c) and 3(f), the angle between a given LOS and the ambient magnetic field determines the pitch angle of the parent protons which emit ENAs along that LOS. Parent protons which intersect a LOS within a cone around the boresight (opening angle  $19.5^\circ$ ) would have pitch angles  $\alpha$  between  $90^\circ - 19.5^\circ = 70.5^\circ$  and  $90^\circ + 19.5^\circ = 109.5^\circ$ . However, observable ENAs would have to be produced *between* Callisto and the detector. Even for a parent proton with the lowest energy considered (i.e.,  $E_0 = 5$  keV), the gyroradius  $(\sqrt{2E_0 m_p} \sin \alpha) / (e|\mathbf{B}_0|)$  within this range of pitch angles is about  $(1.0 - 1.1)R_C$ , an order of magnitude larger than the atmospheric scale height. Therefore, when a proton gyrates into the atmosphere between Callisto and the detector, it does not have sufficient space to turn such that it can emit an ENA along a LOS toward the detector (largely in the radial direction). Parent protons can access the atmosphere with velocity vectors bearing toward a detector on the opposite side of the moon; however, analogous to the scenario described for the detectors located at  $(0, 0, \pm 3R_C)$ , the body of the moon "corks" the cone of lines of sight intersecting the moon's disc, blocking any ENAs produced by such protons. As a result, Callisto's disc is also depleted of ENA flux for detectors in the  $z = 0$  plane (Figures 3(a), 3(b), 3(d), and 3(e)) .

When draping is included for the two detectors at  $z = \pm 3R_C$  (see right side of Figures 3(c) and 3(f)), a "gap" in ENA flux is introduced to the ring in the Jupiter-averted segment of the image ( $y < 0$ ). The formation of this gap can largely be attributed to parent proton deflection by the asymmetric magnetic pile-up region near Callisto. A depiction of the enhanced magnetic field, as calculated by AIKEF, is displayed for the  $z = 0$  and  $x = 0$  planes of the SIS in Figures 4(a) and 4(b), respectively. Figure 4(a) demonstrates how the pile-up region stretches to  $y \approx -2R_C$ , wrapping around the Jupiter-averted, upstream quadrant of the moon in the equatorial plane (see also Liuzzo et al.,

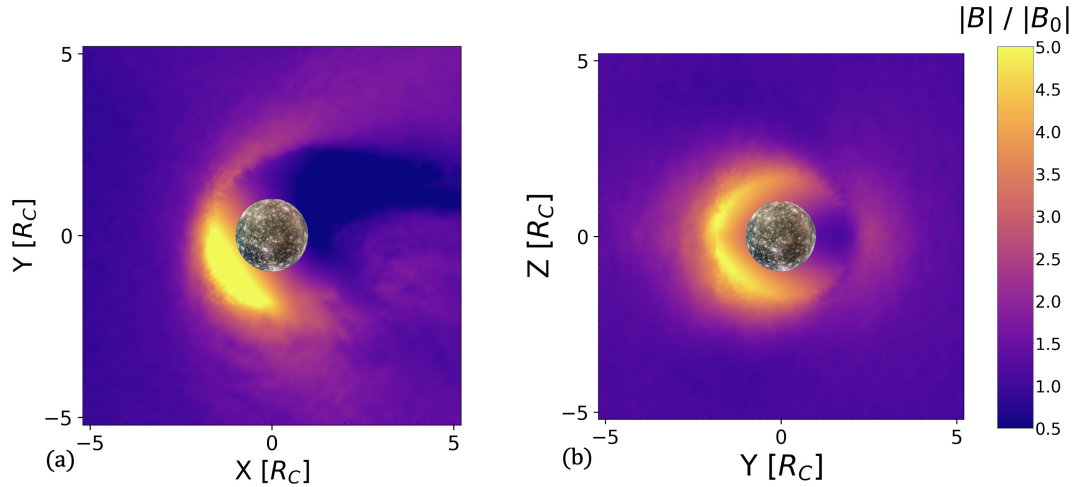


**Figure 4.** Depiction of the magnetic field magnitude  $|\mathbf{B}|$  in the vicinity of Callisto. Panel (a) shows the  $z = 0$  plane, containing the upstream flow velocity  $\mathbf{u}_0$  and the ambient electric field vector  $\mathbf{E}_0 = -\mathbf{u}_0 \times \mathbf{B}_0$ . Panel (b) shows the  $x = 0$  plane that contains  $\mathbf{E}_0$  and  $\mathbf{B}_0$ , looking toward upstream. The magnetic field values shown by the colormaps are normalized to the ambient magnetospheric field strength  $|\mathbf{B}_0| = 4$  nT (see Table 1 of Haynes et al., 2023), and the colorbar on the right applies to both panels.

2015, 2017). As can be seen in Figure 4(b), the region of enhanced  $|\mathbf{B}|$  reaches polar latitudes in the northern and southern hemispheres and wraps around Callisto in a highly asymmetric way, mostly confined to the Jupiter-averted half space ( $y < 0$ ). When the fields are uniform, the proton population contributing to the ring of elevated ENA flux in Figures 3(c) and 3(f) propagates with largely field-aligned or anti-aligned pitch angles. In draped fields, the pile-up region diverts some of these protons away from Callisto's atmosphere; that is, it prevents a portion of the ambient proton distribution from emitting ENAs into the detector. This introduces the gap visible in the ring structure of Figure 3(f). As shown in Figure 4(b), Callisto's Jupiter-averted limb ( $y < 0$ ) is protected to a higher degree by the compressed field lines than the Jupiter-facing one ( $y > 0$ ). Compared to the case of uniform fields, this drives an asymmetric reduction of the ENA flux into the ring, generating the crescent-like feature seen in Figures 3(c) and 3(f). When Callisto's plasma interaction is taken into account, the ENA flux within these crescent features is reduced by up to 25%, compared to the values recorded by these pixels in uniform fields (Figures 3(c) and 3(f)). This reduction is similar in magnitude to that of the ENA flux through a spherical detector encompassing Callisto's entire atmosphere:

748 Haynes et al. (2023) found that field line draping diminishes the ENA flux intensity through  
 749 the detector sphere by 20%–50%, depending on the location on the sphere.

750 We now discuss the emission features in the synthetic ENA images with boresight  
 751 vectors perpendicular to the ambient magnetic field  $\mathbf{B}_0$ . Figures 3(a), 3(b), 3(d), and  
 752 3(e) display our results for these cases. In these panels, the  $z > 0$  half space corresponds  
 753 to the top half of the image. When the fields are uniform, a similar image morphology  
 754 is visible from all four vantages: a ring of elevated ENA flux surrounds Callisto’s disc,  
 755 interrupted by narrow gaps in the moon’s equatorial plane ( $z = 0$ ). The number and  
 756 location of these gaps depend on the detector’s position in the  $z = 0$  plane. As can be  
 757 seen in Figures 3(a) and 3(d), equatorial gaps in the ring of elevated ENA flux are present  
 758 on both sides of the moon for the detector at  $(+3R_C, 0, 0)$ , but only one occurs (in the  
 759  $x > 0$  half space) when the detector is located upstream at  $(-3R_C, 0, 0)$ . Similarly in  
 760 Figures 3(b) and 3(e), two equatorial gaps are present when the detector is located at  
 761  $(0, -3R_C, 0)$ , but only one ( $x > 0$ ) for the detector at  $(0, +3R_C, 0)$ .

762 The gaps in the ring of elevated ENA flux can be attributed to “shielding” by Cal-  
 763 listo due to the  $\mathbf{E}_0 \times \mathbf{B}_0$  drift (bearing toward downstream) and the parent protons’ sense  
 764 of gyration. The mechanism for this shielding is depicted for the backtracing picture in  
 765 Figure 5, where energetic protons are launched with  $\Delta t < 0$  from different lines of sight  
 766 that intersect Callisto’s atmosphere near its limb on both sides. In panel 5(a), we con-  
 767 sider ENA detectors positioned at  $(\pm 3R_C, 0, 0)$ , and in panel 5(b) the detectors are at  
 768  $(0, \pm 3R_C, 0)$ . For the detector located downstream ( $x = +3R_C$ ), as illustrated in Fig-  
 769 ure 5(a), parent protons backtraced from the LOS in the  $y < 0$  half space are near the  
 770 largest negative  $y$  value of their gyration when launched. Such protons will quickly im-  
 771 pact the moon, demonstrated by the forbidden (red) trajectory near the Jupiter-averted  
 772 apex. In the forward-tracing picture, these parent protons are blocked by Callisto’s sur-  
 773 face before reaching the LOS near the moon’s anti-Jovian apex with a tangential veloci-  
 774 ty vector.

775 Again for the detector at  $x = +3R_C$  (Figure 5(a)), most parent protons cannot  
 776 reach a LOS connecting to the equatorial atmosphere for  $y > 0$  with a tangential ve-  
 777 locity vector: in the backtracing picture, many such protons would impact the surface  
 778 of Callisto after nearly a full gyration. Backtraced trajectories similar to the one shown  
 779 for  $y > 0$  may be allowed (and emit ENA flux toward the detector at  $x = 3R_C$ ) if they

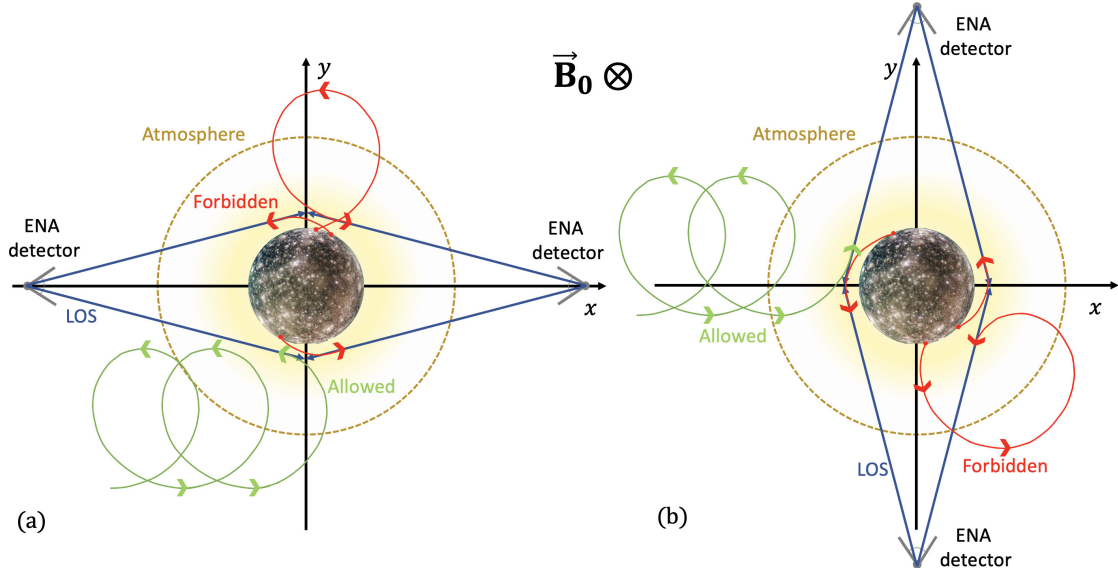


**Figure 5.** Schematic illustration of the shielding of parent protons with pitch angles  $\alpha \approx 90^\circ$  and energies  $E \approx 10$  keV by Callisto's surface, displayed in the  $z = 0$  plane. Several lines of sight (blue) are extended within this plane from the detector toward the limb of Callisto's atmosphere on either side of the moon. Backtraced parent protons are launched from a LOS and evolved with a negative timestep ( $\Delta t < 0$ ). Panel (a) illustrates the shielding for the ENA detectors positioned upstream and downstream of the moon at  $(\mp 3R_C, 0, 0)$ , as seen in Figures 3(a) and 3(d). Panel (b) illustrates the geometry for detectors at  $(0, \mp 3R_C, 0)$ , corresponding to Figures 3(b) and 3(e). Each of the four detectors is represented by gray elements. For the energy range considered, proton gyroradii are between  $1.1R_C$  and  $4.1R_C$  (see Table 2 in Haynes et al., 2023).

780 intersect the LOS in the  $x < 0$  half space. However, ENA generation by such protons  
 781 would occur at much higher altitudes (i.e., within much lower neutral densities) than in  
 782 the example displayed. Thus, such protons emit little ENA flux into the detector. In con-  
 783 sequence, there are equatorial gaps in the ring on both sides of the moon for the syn-  
 784 thetic ENA image taken downstream of Callisto (Figure 3(d)).

785 When the detector is positioned at  $(-3R_C, 0, 0)$  and the fields are treated as uni-  
 786 form, an analogous process occurs for a LOS intersecting the limb of Callisto's atmosphere  
 787 in the  $y > 0$  half space (see Figure 5(a)). In this viewing geometry, the parent protons  
 788 only bear toward the detector when located near the sub-Jovian "crests" of their tra-  
 789 jectories. Therefore, a proton backtraced from the LOS in the  $y > 0$  half space impacts  
 790 the surface of the moon shortly after launch, as illustrated in the upper-left quadrant

of Figure 5(a). However, for the same detector position, a LOS connecting to Callisto's limb in the  $y < 0$  half space is *not* shielded by the moon. As demonstrated by the allowed (green) trajectory backtraced from such a LOS in Figure 5(a), such parent protons only approach (but do not hit) the surface of Callisto as they emit ENAs along the LOS. Thus, the ring of elevated ENA flux observed at  $(-3R_C, 0, 0)$  only has a single equatorial gap in the  $y > 0$  half space (see Figure 3(a)).

For uniform fields, the same dichotomy in the number of gaps is visible for the synthetic ENA images taken at  $(0, \pm 3R_C, 0)$ , as seen in Figures 3(e) and 3(b). When the detector is positioned at  $y = -3R_C$ , parent protons backtraced from a LOS in the  $x < 0$  half space quickly gyrate into Callisto, despite being carried toward upstream by the (small)  $\mathbf{E}_0 \times \mathbf{B}_0$  drift velocity. In the  $x > 0$  half space, backtraced parent protons may complete nearly a full gyration before impacting the moon during their drift toward upstream. Trajectories displaced slightly farther toward  $y < 0$  than our sample trajectory may avoid Callisto while making a weak contribution to the ENA flux into the associated pixel. For a detector located at  $y = +3R_C$ , the sample proton backtraced from the LOS in the  $x > 0$  half space completes only a small fraction of a gyration before impacting Callisto's surface due to the  $\mathbf{E}_0 \times \mathbf{B}_0$  drift and its sense of gyration. In turn, the proton backtraced from the LOS in the  $x < 0$  half space drifts away from the moon on an allowed trajectory (green), illustrating why the ring of elevated ENA flux in Figure 3(e) remains *uninterrupted* for  $x < 0$ .

When draping is included, the ring of high ENA flux disappears from the  $x < 0$  and  $y < 0$  half spaces in panels 3(b) and 3(d), respectively. In contrast, the ENA images in panels 3(a) and 3(e) share a similar morphology between the uniform and draped cases. The changes introduced in the images taken at  $(0, -3R_C, 0)$  and  $(3R_C, 0, 0)$  can largely be attributed to the asymmetric region of enhanced magnetic field displayed in Figure 4: as found by Haynes et al. (2023), parent protons with pitch angles near  $90^\circ$  are deflected away from the moon by the extended pile-up region. Since this region is largely confined to the upstream portion of the  $y < 0$  half space, proton deflection mainly occurs on Callisto's Jupiter-averted side. Parent protons are therefore unable to reach this portion of Callisto's atmosphere, so they cannot emit ENAs into the detectors located at  $(0, -3R_C, 0)$  and  $(3R_C, 0, 0)$ . Thus, localized depletions are introduced to the ring of elevated ENA flux on the Jupiter-averted side of the moon by the draped fields in Figures 3(b) and 3(d).

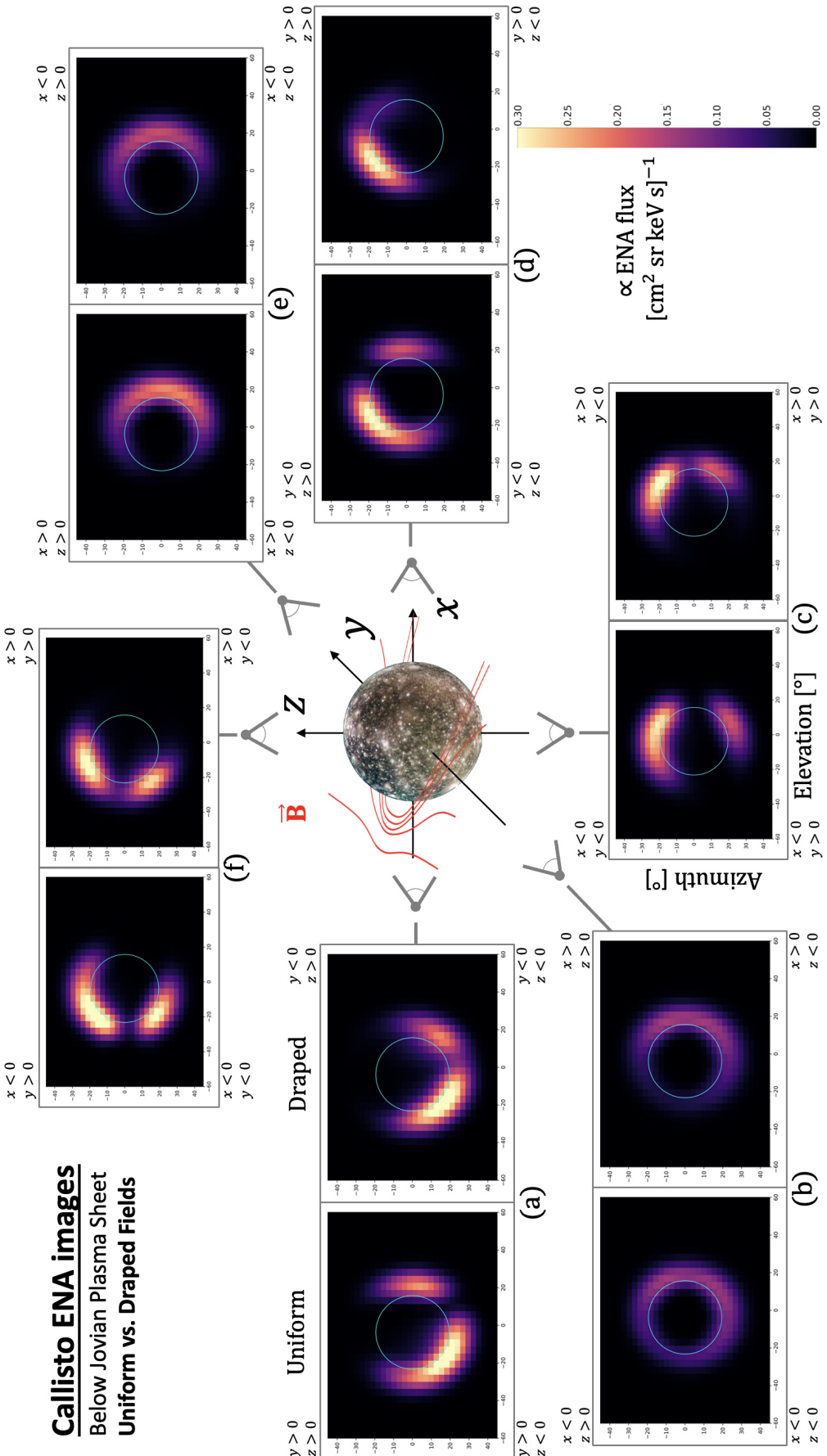


**Figure 6.** Synthetic ENA images of the magnetosphere-atmosphere interaction at Callisto when the moon is at maximum distance below the center of the Jovian plasma sheet. The layout of the figure is analogous to that of Figure 3. In each panel (a)–(f), synthetic ENA images in uniform (left) and draped (right) magnetospheric fields are arranged with detector elevation on the horizontal axis and detector azimuth on the vertical axis. The disc of the moon is represented by the light blue circle in each image. The four corners of each panel are labeled according to the octants of the Satellite Interaction System. The modeled ENA flux for our choice of  $\Delta t$  (see section 2.2) is indicated by the colorbar in the bottom right-hand corner of the figure, the range of which is 1/60 that of the colorbar in Figure 3. Each panel is connected to a gray detector symbol that illustrates the viewing geometry used to create the respective synthetic ENA images. A sketch of the draped magnetic field lines near Callisto is included in red; the ambient magnetospheric field  $\mathbf{B}_0$  in this configuration forms an angle of only  $10^\circ$  with the  $z = 0$  plane.

824        **3.1.2 Callisto Below the Jovian Plasma Sheet**

825        Figure 6 displays synthetic ENA images for Callisto when the moon is at maximum  
 826        distance below the center of the Jovian plasma sheet. The figure is arranged in the same  
 827        way as Figure 3. The ambient magnetic field  $\mathbf{B}_0 = (9.0, 35.3, -6.6)$  nT points mostly  
 828        in the (+y) direction. The field lines form an angle of only  $10^\circ$  with Callisto's equato-  
 829        rial plane ( $z = 0$ ). The projections of the field vectors onto the equatorial plane are slightly  
 830        tilted toward downstream, forming an angle of  $\eta = 14.6^\circ$  with the (+y) axis. For de-  
 831        tectors located at  $(0, -3R_C, 0)$  and  $(0, +3R_C, 0)$ , i.e., Figures 6(b) and 6(e), the respec-  
 832        tive boresight vectors are nearly aligned and anti-aligned with the ambient magnetic field.  
 833        This is also the case for the detectors in Figures 3(f) and 3(c). For uniform fields, the  
 834        images in Figure 3 depict a complete ring of elevated ENA flux. In contrast to this, Fig-  
 835        ure 6(e) shows a crescent pattern of elevated ENA flux mostly in Callisto's upstream hemi-  
 836        sphere, with a gap around the downstream side of the moon. The ring of elevated ENA  
 837        flux in Figure 6(b) does not have any gaps, but it is still non-uniform: the lowest flux  
 838        values occur upstream ( $x < 0$ ) and are shifted slightly northward from the equatorial  
 839        plane ( $z > 0$ ). Similar to Figure 3, little to no ENA flux is recorded within Callisto's  
 840        disc at any of the six detector positions.

841        Even the small tilt  $\eta$  of the magnetic field vectors toward downstream produces a  
 842        disparity in proton accessibility between lines of sight extended into the  $x < 0$  and  $x >$   
 843        0 hemispheres. To illustrate this, Figure 7 shows the geometry of the tilted magnetic field  
 844        lines in the  $z = 0$  plane. For this example, the detector is positioned at  $(0, +3R_C, 0)$ ,  
 845        corresponding to Figure 6(e). In panel 7(a), two lines of sight are extended within this  
 846        plane into the upstream ( $x < 0$ ) hemisphere: one runs tangent to Callisto's surface, form-  
 847        ing an angle of  $\beta_C = \arcsin(1/3) = 19.5^\circ$  with the detector's boresight vector  $(0, -1, 0)$ .  
 848        The other one is tangential to the upper boundary of the model atmosphere at  $|\mathbf{r}| = 2R_C$   
 849        and is inclined against the boresight by  $\beta = \arcsin(2/3) = 41.8^\circ$ . In panel 7(b), the  
 850        two corresponding lines of sight (and associated angles) in the  $x > 0$  hemisphere are  
 851        shown. These four lines of sight represent the minimum ( $\beta_C$ ) and maximum ( $\beta$ ) devi-  
 852        ations from the boresight direction for ENA trajectories detectable outside of Callisto's  
 853        disc on either side of the moon.

854        Again neglecting the small  $\mathbf{E}_0 \times \mathbf{B}_0$  drift velocity, the angle  $\xi$  between a LOS and  
 855        the magnetospheric field lines determines (in uniform fields) the pitch angle  $\alpha$  that a par-

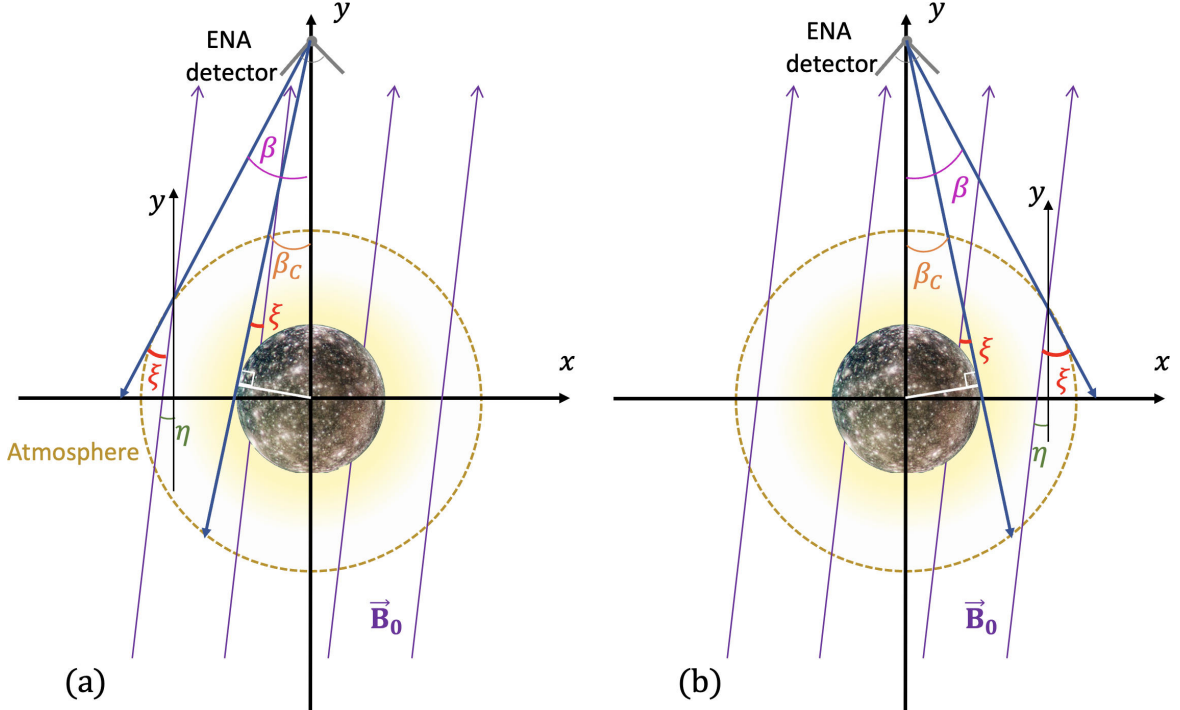


**Figure 7.** Schematic depicting the asymmetric shielding of parent protons by Callisto due to the tilted magnetospheric field  $\mathbf{B}_0$ , shown in the  $z = 0$  plane. For the detector located at  $(0, +3R_C, 0)$ , the range of possible angles  $\xi$  (red) between a LOS and the ambient field  $\mathbf{B}_0$  is compared between the upstream ( $x < 0$ ) and downstream ( $x > 0$ ) hemispheres in panels (a) and (b), respectively. Jovian magnetosospheric field lines are displayed in purple, with the tilt angle  $\eta \approx 14.3^\circ$  between  $\mathbf{B}_0$  and the  $(+y)$  axis. The detector is represented by the conjoined gray line segments, with a blue LOS extended toward the innermost and outermost edges of the atmospheric neutral gas outside of Callisto's disc on (a) the upstream side and (b) the downstream side. These lines of sight form angles of  $\beta_C$  (inner edge, orange arc) and  $\beta$  (outer edge, magenta arc) against the boresight vector  $(0, 0, -1)$ , respectively. The dashed yellow circle represents the upper boundary of our model atmosphere.

856 ent proton must have in order to emit an ENA into that pixel on the detector. Using  
 857 figure 7(a), we can calculate the range of  $\xi$  for lines of sight extended toward the upstream  
 858 half space ( $x < 0$ ). Since the magnetic field lines are tilted *toward* such a LOS in this  
 859 half space, the angle  $\xi$  ranges from  $\beta_C - \eta = 4.9^\circ$  to  $\beta - \eta = 27.2^\circ$ . The range of pitch  
 860 angles for parent protons that can emit ENAs along these lines is identical to the range  
 861 of  $\xi$ , namely  $\alpha \in \{4.9^\circ, 27.2^\circ\}$ . In contrast, the range of  $\xi$  for a LOS extended toward  
 862 the downstream ( $x > 0$ ) half space is from  $\beta_C + \eta = 34.1^\circ$  to  $\beta + \eta = 56.4^\circ$ , with the

same range for pitch angles given by  $\alpha \in \{34.1^\circ, 56.4^\circ\}$ . In the  $x > 0$  half space, the magnetic field lines are tilted *against* this detector's lines of sight. Therefore, the set of all  $\xi$  values are elevated by  $2\eta$  compared to the  $x < 0$  half space (Figure 7(a) versus 7(b)). Thus, in the downstream half space, the pitch angles of protons contributing to the ENA image are closer to  $\alpha = 90^\circ$  than in the upstream half space (where they are closer to  $\alpha = 0^\circ$ ). The gyroradius is proportional to  $\sin \alpha$ . Because of this, parent protons bearing toward a LOS in the  $x > 0$  half space (with near-perpendicular pitch angles and larger gyroradii) are more likely to impact the moon's surface before reaching the LOS than those traveling (with a steeper pitch angle) toward a LOS with the same tilt against the boresight but in the  $x < 0$  half space. In consequence, when the detector is positioned at  $(0, +3R_C, 0)$ , the ENA flux into the ring peaks in the  $x < 0$  half space where the associated parent ions possess the smaller range of gyroradii, whereas a reduction in flux is formed for  $x > 0$  (Figure 6(e)). When the detector is located at  $(0, -3R_C, 0)$ , a LOS extending into the  $x < 0$  half space makes a *larger* angle  $\xi$  against the magnetic field lines than one with the same tilt against the boresight  $(0, 1, 0)$  in the  $x > 0$  half space. Thus, the ENA flux into the ring is reduced for  $x < 0$ , as seen in Figure 6(b). When the fields are uniform, the slight north-south asymmetry in the ENA emission pattern of Figure 6(b) may be caused by the tilt of  $\mathbf{B}_0$  against the  $z = 0$  plane and the nonzero  $\mathbf{E}_0 \times \mathbf{B}_0$  drift.

In order to verify that the non-uniformities of the ENA flux into the rings from Figures 6(b) and 6(e) are caused by the tilt between the detector boresight and  $\mathbf{B}_0$ , Figure 8 displays four additional pairs of synthetic ENA images for Callisto located at maximum distance below the center of the Jovian plasma sheet. For all images in Figure 8, the detector is again located on a sphere of radius  $3R_C$  around the moon, with the boresight vector pointing toward its center. The elevation and azimuth axes for these images are parallel to the longitude and latitude circles of the West Longitude system (see, e.g., Section 2 of Haynes et al., 2023) which run through the detector's position. In these images, the detectors' boresight vectors are oriented parallel to  $\mathbf{B}_0$  (Figure 8(b)), anti-parallel to  $\mathbf{B}_0$  (Figure 8(d)), and perpendicular to  $\mathbf{B}_0$  (Figures 8(a) and 8(c)). The detectors in Figures 8(a) and 8(c) are both located in the  $y = 0$  plane, upstream and downstream of Callisto, respectively.

Due to the small tilt ( $17.5^\circ$ ) of the magnetic field lines against the boresight vector in Figure 6, the viewing geometries in Figures 8(b) and 8(d) are only slightly differ-

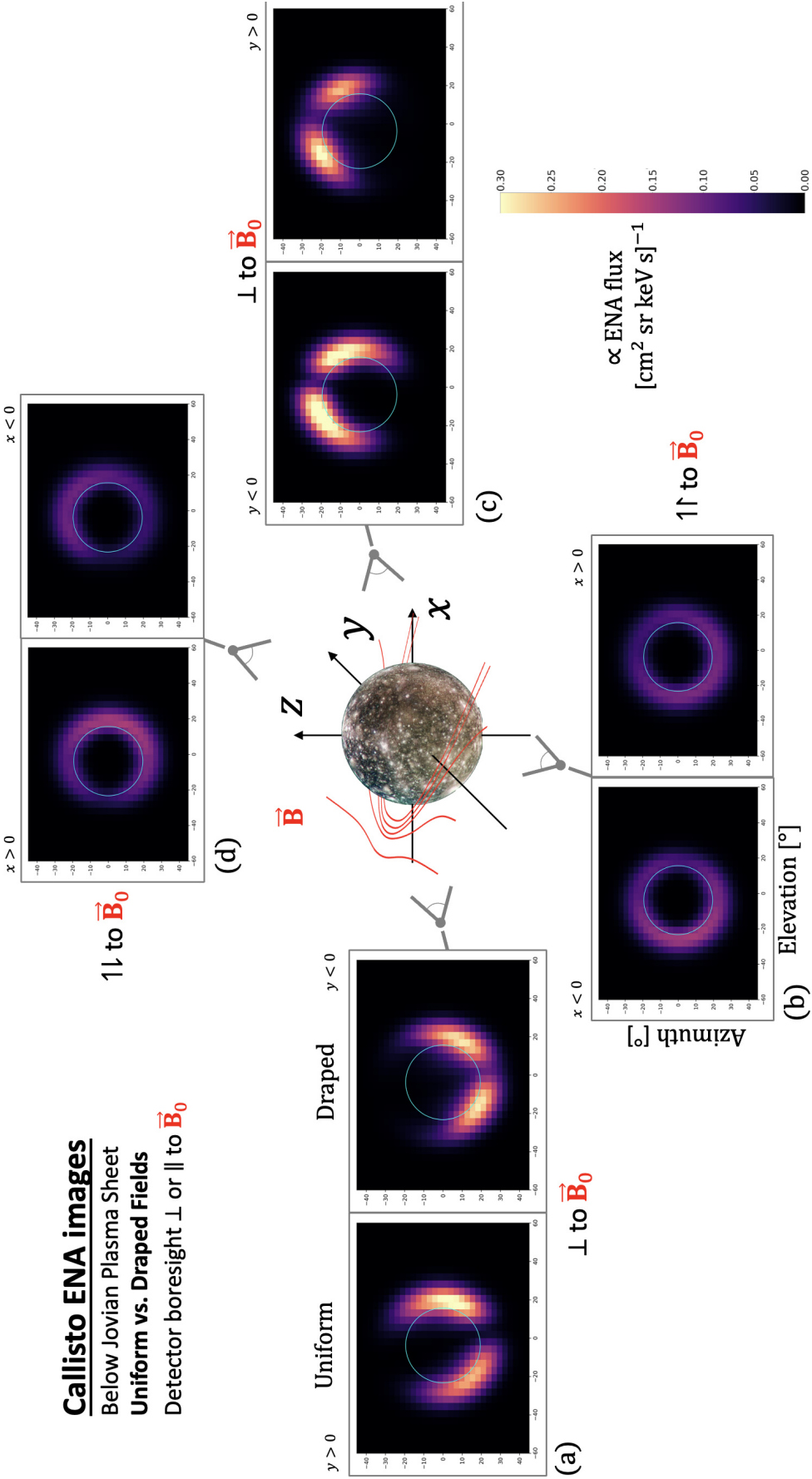


**Figure 8.** Synthetic ENA images at Callisto when the moon is at maximum distance below the center of the Jovian plasma sheet, for boresight vectors aligned with  $\vec{B}_0$  (panel (b)), anti-aligned with  $\vec{B}_0$  (panel (d)), and perpendicular to  $\vec{B}_0$  (panels (a) and (c)). In the counter-clockwise direction (starting with panel (a)), the detector positions read:  $(-1.77, 0, -2.42) R_C$ ,  $(-0.72, -2.86, 0.53) R_C$ , and  $(0.72, 2.86, -0.53) R_C$ . At all positions, the detector is placed on a sphere of radius  $3R_C$ . For the two boresight orientations perpendicular to the background field, the detector is positioned in the  $y = 0$  plane, upstream of the moon in panel (a) and downstream of it in panel (c). Synthetic ENA images in uniform (left) and draped (right) magnetospheric fields are arranged with detector elevation on the horizontal axis and detector azimuth on the vertical axis. The detectors' azimuth and elevation axes are respectively parallel to the latitude and longitude circles of the West Longitude system which intersect the detector at that point on the sphere. The boresight vector always points toward the center of the moon. The top corners of each panel are labeled to roughly indicate the sectors of the Satellite Interaction System. The modeled ENA flux for our choice of  $\Delta t$  (see section 2.2) is indicated by the colorbar in the bottom right-hand corner of the figure, with a scale equal to that used for Figure 6. Each panel is attached to a gray detector symbol that approximately shows the viewing geometry used to create the respective synthetic ENA images. The draped magnetic field lines near Callisto are included in red.

896 ent from those in Figures 6(b) and 6(e). Even still, the morphologies of the respective  
 897 ENA images are qualitatively different. For the case of a uniform, southward magneto-  
 898 spheric field at the center of the plasma sheet, the two detectors with boresight vectors  
 899 parallel or anti-parallel to  $\mathbf{B}_0$  record a highly similar ENA emission pattern to that seen  
 900 in Figure 8 (see Figures 3(c) and 3(f)). Thus, regardless of the ambient field orientation,  
 901 the morphology of the ENA emissions recorded by detectors with boresight vectors pre-  
 902 cisely parallel or anti-parallel to  $\mathbf{B}_0$  is determined by the density profile of Callisto's at-  
 903 mosphere. When introducing the  $17.5^\circ$  angle between the boresight vector and the mag-  
 904 netic field lines (going from Figure 8(b) to Figure 6(b)), the reduction in the ring flips  
 905 from the upstream to the downstream side. Comparing Figures 8(d) and 6(e) shows the  
 906 ENA flux is still maximized in the upstream hemisphere, but an extended gap is carved  
 907 out of the ring on the downstream side. The similarity between the ENA images obtained  
 908 for the “center” (Figure 3) and “below” (Figure 8) cases with boresight vectors paral-  
 909 lel (and anti-parallel) to  $\mathbf{B}_0$  shows that drastic morphological changes are driven by the  
 910 slight misalignment between the boresight and  $\mathbf{B}_0$ .

911 In uniform magnetospheric fields, only localized “patches” of high ENA flux oc-  
 912 cur along the moon's limb when the boresight vector is contained in the  $y = 0$  plane  
 913 (Figures 6(a), 6(c), 6(d), and 6(f)). When the fields are uniform,  $\mathbf{B}_0$  is oriented approx-  
 914 imately perpendicular to the detectors' boresight vectors in these setups. Therefore, the  
 915 bulk of the ENA flux contributing to these four images is due to parent protons with pitch  
 916 angles near  $90^\circ$ . When Callisto is at maximum distance below the Jovian plasma sheet,  
 917 the ambient field is an order of magnitude stronger than at the center of the sheet (see  
 918 Table 1 of Haynes et al., 2023). Parent proton gyroradii are reduced by the same fac-  
 919 tor, so that the scale of gyration in our considered energy range is only about  $(0.1\text{--}0.5)R_C$ .  
 920 In consequence, only localized regions of Callisto's atmosphere remain highly accessible  
 921 to the impinging parent protons (see also Figures 6 and 8 in Liuzzo et al., 2022). Pro-  
 922 tons that can still access the atmosphere produce isolated patches of elevated ENA flux  
 923 near the moon's limb, as seen in Figures 6(a), 6(c), 6(d), and 6(f).

924 When Callisto is at maximum distance below the Jovian plasma sheet, the induced  
 925 magnetic dipole moment is near its peak strength (e.g., Zimmer et al., 2000; Hartkorn  
 926 & Saur, 2017). In order to isolate the contribution of this induction signal to the ENA  
 927 emission morphology in Figure 6, we have generated a separate series of ENA images for  
 928 a mere superposition of  $\mathbf{B}_0$  and the induced dipole. This series is discussed in Appendix

929 A. Compared to the case of uniform fields (left images in Figure 6), the induced dipole  
 930 field imparts only minor modifications to the ENA emission morphology for any of the  
 931 six viewing geometries considered. The right panels in Figure 6 show synthetic ENA im-  
 932 ages when the plasma interaction with Callisto’s atmosphere and induced dipole is taken  
 933 into account. Comparison to the results from Appendix A reveals that the image mor-  
 934 phologies obtained for any of the six viewing geometries are very similar to those obtained  
 935 in the “superposition” scenario. Thus, when Callisto is exposed to the dilute magneto-  
 936 spheric flow far below Jupiter’s plasma sheet, the influence of the field line draping and  
 937 pile-up on the ENA images is mainly quantitative in nature. The effect of the plasma  
 938 interaction can be isolated from the contribution of the induced dipole (without plasma  
 939 currents) only if precise knowledge on the upstream conditions and the 3D atmospheric  
 940 structure at the time of image acquisition is available. Due to the strong similarities be-  
 941 tween the ENA images for the superposition setup (right sub-panels in Figure A1) and  
 942 those including the plasma interaction currents (right panels in Figure 6), the following  
 943 discussion uses the term “non-uniform fields” to jointly refer to these two scenarios.

944 Far below the Jovian plasma sheet, non-uniformities in the fields near Callisto in-  
 945 troduce appreciable modifications to the ENA image morphology only when the detec-  
 946 tor is located at  $(+3R_C, 0, 0)$ : the patch of elevated ENA flux around the sub-Jovian  
 947 ( $y > 0$ ) hemisphere that forms in uniform fields is strongly attenuated, as seen in Fig-  
 948 ure 6(d). While this feature is already weakened in the “superposition” case (Figure A1(d)),  
 949 it is removed almost entirely when draping is included in addition (Figure 6(d)). At the  
 950 other five detector locations, the changes introduced by non-uniform fields are rather sub-  
 951 tle. When the boresight vector is parallel or perpendicular to  $\mathbf{B}_0$  (right images in Fig-  
 952 ure 8), the synthetic ENA images are again highly similar between uniform and draped  
 953 fields. For all ten viewing geometries (Figures 6 and 8), the maximum ENA intensities  
 954 in the images remain within 15% of their values in uniform fields when draping is included.

955 The changes brought about by the non-uniform fields stem from the altered acces-  
 956 sibility pattern of Callisto’s atmosphere for precipitating parent protons (see Liuzzo et  
 957 al., 2019b, 2022). The similarity between synthetic ENA images produced for uniform  
 958 and non-uniform fields in Figures 6 and 8 is consistent with the subtle influence of drap-  
 959 ing (or the induced dipole in isolation) on the global ENA emission pattern; see Figure  
 960 15 of Haynes et al. (2023). Thus, when Callisto is far outside of the Jovian plasma sheet,  
 961 the presence of any non-uniformities in the fields may be difficult to probe unless the view-

962     ing geometry is carefully selected: only for one of our chosen detector locations do such  
 963     non-uniformities play a significant role in shaping the ENA image (i.e., Figure 6(d)). At  
 964     the other detector locations considered, the modifications to the images are likely dif-  
 965     ficult to discern against the “background” ENA emissions generated by the Jovian mag-  
 966     netosphere (e.g., Mauk et al., 2003).

967       We do not generate synthetic ENA images for Callisto at maximum distance above  
 968     the center of the Jovian plasma sheet. In this case, the ambient field orientation and the  
 969     orientation of the induced dipole are mirrored compared to the “below” case. This will  
 970     also flip some structures in the synthetic ENA images, but it will not introduce any novel  
 971     morphological features. The same approach is taken in our study of ENA emissions at  
 972     Europa. We also note that using a smaller atmospheric scale height at Callisto (e.g., Liang  
 973     et al., 2005) would merely shrink the radial extension of the features in the synthetic im-  
 974     ages.

### 975       3.2 Analysis of Synthetic ENA Images at Europa

#### 976       3.2.1 Europa at the Center of the Jovian Plasma Sheet

977       Figure 9 shows synthetic ENA images at Europa when the moon is at the center  
 978     of the Jovian plasma sheet. The figure is arranged in an analogous fashion to Figures  
 979     3 and 6. For all ENA images in Figure 9, the detector is located at a distance of  $3R_E$   
 980     from the origin (i.e., at an altitude of  $2R_E$ ), with a boresight vector directed toward the  
 981     center of the moon. The ambient magnetospheric field  $\mathbf{B}_0$  points southward in this case.  
 982     The field magnitude at Europa ( $|\mathbf{B}_0| = 410 \text{ nT}$ ) is two orders of magnitude higher than  
 983     in the “center” case at Callisto. Even for the lowest energy considered, the proton ve-  
 984     locity  $\sqrt{2E_0/m_p}$  ( $\approx 979 \text{ km/s}$ ) outpaces the  $\mathbf{E}_0 \times \mathbf{B}_0$  drift ( $100 \text{ km/s}$ ) by about an or-  
 985     der of magnitude.

986       For the detectors positioned above Europa’s poles at  $(0, 0, \pm 3R_E)$ , a ring of ele-  
 987     vated ENA flux surrounding the moon’s disc is recorded, though extremely faint in the  
 988     downstream hemisphere (Figures 9(f) and 9(c)). For these two images, the boresight vec-  
 989     tor is aligned or anti-aligned with  $\mathbf{B}_0$ , respectively. Analogous to Callisto (Figures 3(c)  
 990     and 3(f)), parent protons which contribute to the elevated ENA flux in this ring feature  
 991     must travel through the atmosphere above Europa’s limb with velocity vectors nearly  
 992     parallel or anti-parallel to  $\mathbf{B}_0$ . The ENA flux intensity within the ring peaks at the ram-

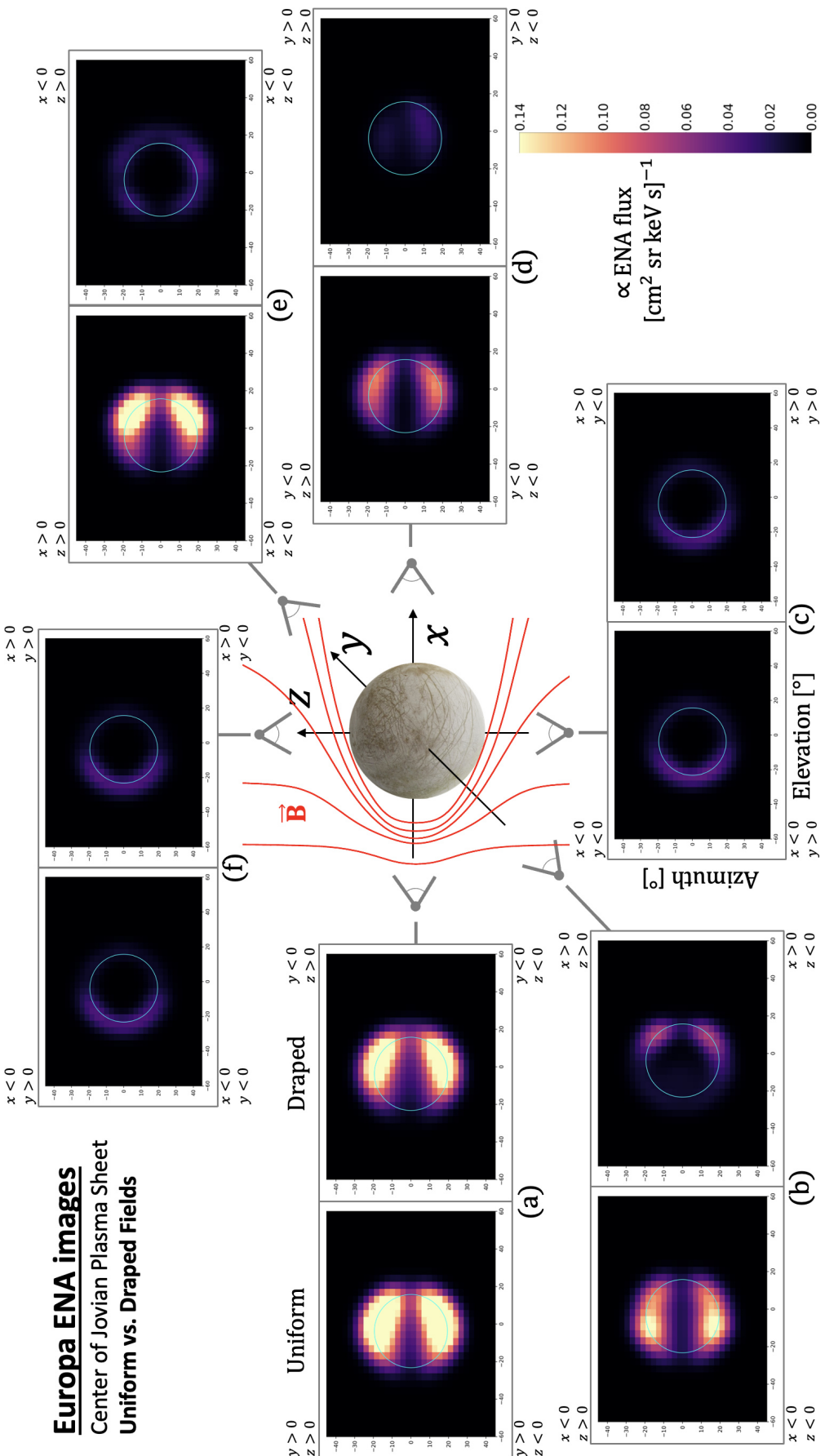


**Figure 9.** Synthetic ENA images of the magnetosphere-atmosphere interaction at Europa when the moon is at the center of the Jovian plasma sheet. The layout of the figure is analogous to that of Figures 3 and 6. In every panel (a)–(f), synthetic ENA images in uniform (left) and draped (right) magnetospheric fields are arranged with detector elevation on the horizontal axis and detector azimuth on the vertical axis. Europa's disc is depicted by the light blue circle in each image. The four corners of each panel are labeled corresponding to the half spaces of the Satellite Interaction System. The colorbar indicates the values of the ENA flux for our choice of  $\Delta t$  (see section 2.2). Each panel is connected to a gray detector symbol that shows the viewing geometry of the respective synthetic ENA images. A sketch of the draped magnetic field lines near Europa is included in red; the ambient field  $\mathbf{B}_0$  in this configuration is oriented southward, like it is for Callisto in Figure 3.

993 side apex and decreases by a factor of four moving to the downstream hemisphere, where  
 994 it is approximately constant. In our model, the number density of Europa’s atmosphere  
 995 is maximized above the ramside apex and decreases (in the upstream hemisphere) when  
 996 moving angularly away from this point toward downstream. The detectors in Figures  
 997 9(c) and 9(f) capture a side-on view of the atmospheric density profile, and hence, the  
 998 emissions display a similar morphology. The two detectors located at  $(0, \pm 3R_E, 0)$  also  
 999 view the asymmetric neutral profile side-on (Figures 9(e) and 9(b)). Thus, the intensity  
 1000 of the ENA emissions in these images decreases when moving from the ramside apex to-  
 1001 ward downstream ( $x > 0$ ). In contrast, the detectors positioned at  $(\pm 3R_E, 0, 0)$  do not  
 1002 perceive the ram-wake asymmetry in the atmosphere since the neutral density is rota-  
 1003 tionally symmetric about the  $x$  axis (Haynes et al., 2023).

1004 The synthetic ENA images taken in Europa’s equatorial plane ( $z = 0$ ) display re-  
 1005 gions of high ENA flux which significantly penetrate into the moon’s disc in uniform fields  
 1006 (see Figure 9). For instance, the detector at  $(-3R_E, 0, 0)$  records the peak in ENA flux  
 1007 *on* Europa’s disc. ENA generation largely occurs within one atmospheric scale height  
 1008 ( $100\text{ km} \approx 0.07R_E$ ) of the moon’s surface (Haynes et al., 2023). Parent protons in our  
 1009 energy range have gyroradii of around  $0.02\text{--}0.06 R_E$ , i.e., in contrast to Callisto, these  
 1010 are much smaller than the size of the moon. Thus, protons with pitch angles near  $\alpha =$   
 1011  $90^\circ$  may readily emit ENAs along a LOS that intersects the atmosphere *between* Europa’s  
 1012 surface and the detector at  $2R_E$  altitude, thereby populating the moon’s disc with ENA  
 1013 flux. The detectors located above Europa’s north and south poles also do not record any  
 1014 ENA flux within the moon’s disc (Figures 9(f) and 9(c)), akin to the process described  
 1015 for Figures 3(c) and 3(f) in section 3.1.

1016 When the detector is located in the equatorial plane (Figures 9(a), 9(b), 9(d), and  
 1017 9(e)), the observed ENA flux in uniform fields is clustered into two “patches” that are  
 1018 symmetric with respect to the equator ( $z = 0$ ). For these viewing geometries, the am-  
 1019 bient field  $\mathbf{B}_0$  is normal to the boresight vector. A similarly segmented (but less confined)  
 1020 ENA emission morphology has been revealed at Callisto when *below* the Jovian plasma  
 1021 sheet, again observed by detectors in the plane perpendicular to the magnetic field (Fig-  
 1022 ures 8(a) and 8(c)). However, when Callisto is at the *center* of the plasma sheet, detec-  
 1023 tors with boresight vectors perpendicular to  $\mathbf{B}_0$  see largely uninterrupted rings of ele-  
 1024 vated ENA flux that encircle the moon’s disc (see Figures 3(a), 3(b), 3(d), and 3(e)). At  
 1025 the center of the sheet, the ambient magnetic field is an order of magnitude weaker than

when Callisto is at maximum distance below the plasma sheet.  $|\mathbf{B}_0|$  is increased by another order of magnitude at Europa compared to the Callisto scenario below the plasma sheet. Hence, the segmentation of the ENA emission features near Europa's or Callisto's disc increases with growing ambient field strength (i.e., with decreasing gyroradii  $r_g$ ). In uniform fields, parent protons contributing to the ENA emissions observed by a detector with its boresight perpendicular to  $\mathbf{B}_0$  possess pitch angles near  $90^\circ$ . Thus, for these viewing geometries, the size of the gyroradius (compared to the moon's radius) largely shapes the ENA emission morphology.

In uniform fields, the maximum values of the ENA flux in each image depend strongly on the detector's position. For detectors within the equatorial plane ( $z = 0$ ), the highest ENA fluxes are measured upstream of Europa (Figure 9(a)), and the peak values drop by about a factor of three moving longitudinally around the moon to its downstream side (Figures 9(b), 9(e), and 9(d)). Haynes et al. (2023) found a consistent trend within the band of elevated ENA flux recorded by a spherical detector encompassing Europa's atmosphere. The “global” ENA model also revealed that at a given longitude on the detector sphere, the ENA emissions peak within the equatorial band and fall by a factor of six moving to northern or southern polar latitudes. This decrease in emissions with latitude is similarly consistent with Figure 9: at all four detectors within the equatorial plane (Figures 9(a), 9(b), 9(d), 9(e)), the peak ENA flux is approximately 2–6 times greater than that recorded by the detectors above Europa's north and south poles (Figures 9(c) and 9(f)). However, we also point out that the global ENA detector does not “filter” the ENA emissions in velocity space in the manner that a realistic ENA imaging instrument does. The conceptual differences between these approaches caution a quantitative comparison between the two model outputs.

When the fields are treated as uniform, the locations of the patches in Figures 9(a), 9(b), 9(d), and 9(e) are markedly skewed toward one side of the moon's disc, asymmetric with respect to the  $z$  axis and bearing resemblance to “pac-man”. For instance, the patches of high ENA flux in Figure 9(a) are separated in azimuth (vertical axis) by only two pixels at the Jupiter-averted edge of the disc ( $y < 0$ , right side), but by at least ten at the Jupiter-facing edge ( $y > 0$ , left side). The mechanism driving this dichotomy is illustrated in Figure 10, where we display the four equatorial detectors from Figure 9. The detectors located upstream/downstream are shown in light blue, and the detectors positioned above the sub/anti-Jovian apices are represented in magenta. For each

of the detectors, trajectory segments of two protons which contribute to the ENA image depicted in the same color: for example, the two protons in blue could emit ENAs toward both the upstream and downstream detectors.

These trajectory arcs illustrate how a proton's sense of gyration affects the altitudes from which it may emit ENAs into these four detectors. For a southward ambient field  $\mathbf{B}_0$ , the parent protons gyrate counter-clockwise in planes of constant  $z$  when viewed from the north, as depicted by the blue and magenta arcs. When the ENA detector is positioned upstream (i.e., left blue detector in Figure 10), parent protons can attain a velocity vector parallel to a LOS at lower altitudes on the Jupiter-averted ( $y < 0$ ) side

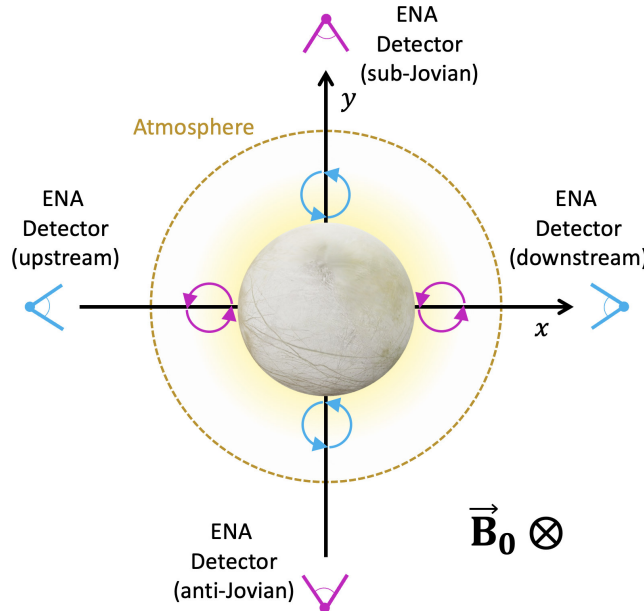


**Figure 10.** Schematic illustrating the gyromotive effect which drives the asymmetric “pacman” morphology of the ENA emissions recorded by detectors in Europa’s equatorial plane ( $z = 0$ ). The figure depicts a plane of constant  $z$  where  $z \neq 0$ : bright ENA emissions do not occur in the  $z = 0$  plane itself (see Figure 9). For each detector of a given color, the proton gyration arcs in the same color could emit ENAs along a LOS and contribute to the dichotomy in emission morphology seen for that viewing geometry. For instance, the two light blue proton trajectory segments could generate ENA emissions into the detectors located both upstream and downstream of Europa. Note that the gyroradii illustrated here are *not* to scale but are enlarged compared to the size of the moon. The dashed yellow circle represents the upper boundary of Europa’s atmosphere in our model.

than on the Jupiter-facing side, since those on the Jupiter-facing side bear *away* from the detector when nearest Europa's surface. In consequence, the patch of elevated ENA flux is more extended in the Jupiter-averred half space than in the Jupiter-facing one (see Figure 9(a)). This asymmetry in the altitude of ENA production and the associated morphological features flip for the image taken from downstream (right blue detector in Figure 10): as illustrated by the light blue arcs, parent protons can now emit an ENA along a LOS at a lower altitude in the Jupiter-facing half space than in the Jupiter-averred half space, causing the patches of elevated ENA flux to be more pronounced on the  $y > 0$  side of Europa's disc in Figure 9(d).

An analogous dichotomy afflicts the ENA image taken by the detector at  $(0, +3R_E, 0)$ : protons access lines of sight with tangential velocity vectors at lower altitudes in the upstream half space than in the downstream one (see magenta elements of Figure 10). This contributes to the shift of the patches toward upstream for the detector in Figure 9(e). According to Figure 10, a similar "pac-man" feature would be expected for the ENA image taken above the anti-Jovian apex, with the patches slightly shifted toward downstream ( $x > 0$ ). However, the equator-facing boundaries of the patches in Figure 9(b) are nearly parallel to the ( $z = 0$ ) plane. In this case, the visibility of the "pac-man" effect is obscured as a result of two competing processes: (i) the contribution of gyration (Figure 10) tends to shift regions of elevated ENA flux toward downstream; (ii) Europa's atmospheric density is lower in the downstream half space than upstream, thereby counteracting the shift in ENA flux caused by gyration. In contrast to this, when the detector is located above the sub-Jovian apex (Figure 9(e)), both (i) and (ii) tend to enhance the ENA emissions in the upstream half space, making the "pac-man" feature clearly discernible.

When Europa is at the center of the Jovian plasma sheet, field line draping imparts significant modifications to the intensity and/or morphology in three of the four ENA images taken in the equatorial plane ( $z = 0$ ). When the fields are draped, the images taken from  $(0, \pm 3R_E, 0)$  both exhibit an 85% reduction in flux in the upstream ( $x < 0$ ) half-space, with only a slight (below 20%) weakening in the downstream half space (Figures 9(e) and 9(b)). As a result, the peak ENA flux in the right panel of Figure 9(b) now lies in the downstream half space. The detector positioned downstream at  $(0, 0, 3R_E)$  becomes nearly depleted of ENA flux when draping is included, with the remaining ENA flux observed entirely within the moon's disc (Figure 9(d)). In contrast, the detector lo-

cated upstream of the moon (Figure 9(a)) still records fluxes in the patches which remain within 20% of their values in uniform fields. The strong modifications to the upstream portions of the ENA images in panels 9(b) and 9(e) are associated with the magnetic field enhancement in Europa's ramside pile-up region, where the field strength increases to about  $1.6|\mathbf{B}_0|$  (see, e.g., Figure 3(g) in Haynes et al., 2023). For these two detectors, a LOS extended beyond Europa's limb passes through the upstream atmosphere within the ramside pile-up region, which has a reduced accessibility to protons with pitch angles near  $90^\circ$ . The process of proton deflection by the pile-up region is exemplified in Figure 8 of Haynes et al. (2023). The drastic attenuation of the ENA fluxes seen by the downstream detector (Figure 9(d)) stems from field line draping, analogous to Callisto (see section 3.1.1).

When field line draping is incorporated, the ENA flux pattern and intensity observed by the two polar detectors are nearly unaltered from their appearance in uniform fields (Figures 9(c) and 9(f)). In contrast to this, field line draping at Callisto qualitatively affects the morphology of the observable ENA emissions for these two viewing geometries (Figures 3(f) and 3(c)). The Alfvénic Mach number  $M_A$  at Callisto ( $M_A = 3.45$ ) is substantially larger than at Europa ( $M_A = 0.68$ ; see Table 1 in Haynes et al., 2023). Therefore, the draped field lines above Callisto's polar caps are more strongly inclined against the  $z$  axis than at Europa, with the flow-aligned component  $B_x$  reaching  $1.5|\mathbf{B}_0|$  at Callisto and remaining below  $0.5|\mathbf{B}_0|$  at Europa (see Figures 3(a) and 3(c) in Haynes et al., 2023). Thus, the draped field lines above Europa's poles are more aligned with the (straight) background field lines of  $\mathbf{B}_0$  than at Callisto, and the trajectories of parent protons with steep pitch angles are less severely impacted at Europa. This explains the weak influence of draping on the ENA images taken above Europa's poles, where the fluxes are altered by no more than 15%.

### 3.2.2 Europa Below the Jovian Plasma Sheet

Figure 11 displays synthetic ENA images in uniform (left sub-panels) and draped fields (right sub-panels) at Europa when the moon is at maximum distance below the Jovian plasma sheet. The figure is arranged in an analogous manner to Figure 9. In this configuration, the ambient magnetospheric field  $\mathbf{B}_0 = (4.0, 209.0, -385.0)$  nT is still oriented mostly southward, making an angle of  $\arctan |B_{y,0}/B_{z,0}| \approx 28.5^\circ$  against the  $(-z)$  axis. The flow-aligned component  $B_{x,0}$  is less than 1% of  $|\mathbf{B}_0|$ , so the magnetic field

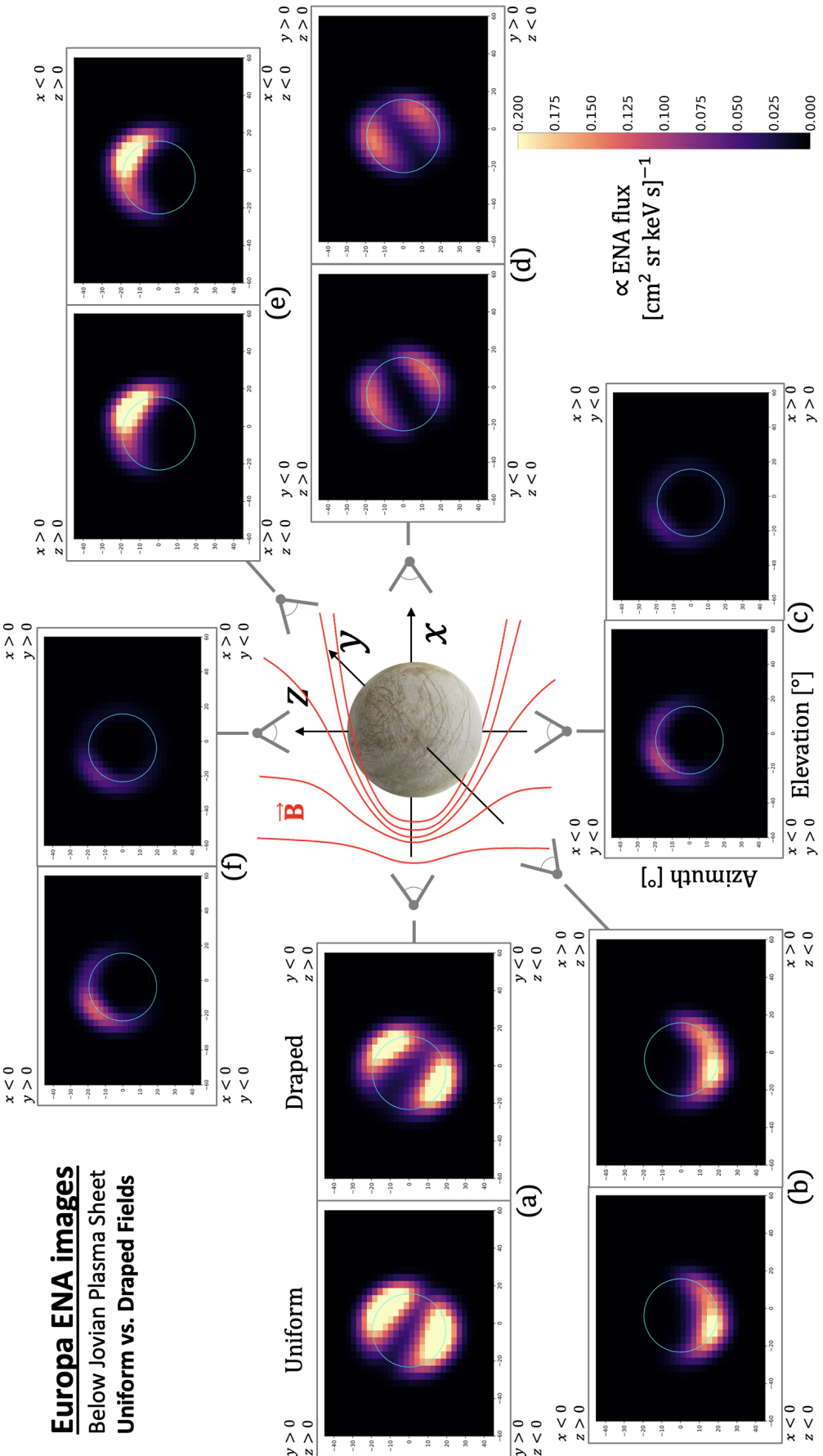


**Figure 11.** Synthetic ENA images at Europa when the moon is at maximum distance below the center of the Jovian plasma sheet. The layout of the figure is analogous to that of Figures 3, 6 and 9, with detector elevation on the horizontal axis and detector azimuth on the vertical axis. Europa's disc is represented by the light blue circle. The four corners of each panel are again labeled according to the sectors of the Satellite Interaction System. The values of the ENA flux for our choice of  $\Delta t$  (see section 2.2) are represented by the colorbar. A sketch of the draped magnetic field lines near Europa is included in red. The ambient field reads  $\mathbf{B}_0 = (4.0, 209.0, -385.0)$  nT, i.e., it is still oriented mainly southward.

lines are approximately parallel to the  $x = 0$  plane. The ambient field strength is only about 7% greater than at the center of the plasma sheet. Therefore, parent proton gyroradii are nearly the same in the scenarios from Figures 9 and 11.

When the fields are treated as uniform, the detectors positioned north and south of Europa record elevated ENA flux within a crescent-shaped region around the moon's disc (Figures 11(f) and 11(c)). The projection of the ambient field  $\mathbf{B}_0$  onto the  $x = 0$  plane makes an angle of  $\tilde{\eta} = 28.5^\circ$  against the  $(-z)$  axis and is inclined toward Jupiter. Hence, the lines of sight extended into the sub-Jovian and anti-Jovian hemispheres have a different range of inclinations against the magnetic field. This creates a geometric situation analogous to that shown in Figure 7. For the detector located north of Europa (Figure 11(f)), the geometry from Figure 7(a) now occurs in the  $y > 0$  half space: the lines of sight which extend toward Europa's limb make a smaller angle against the field lines of  $\mathbf{B}_0$  on the Jupiter-facing side of the moon than on the Jupiter-averred side, thereby driving an elevated ENA flux recorded in the  $y > 0$  portion of the image. A scenario analogous to Figure 7(b) takes place in the Jupiter-averred ( $y < 0$ ) half space, where the range of angles between the LOS and  $\mathbf{B}_0$  is increased by  $2\tilde{\eta}$ . Therefore, the gyroradii of parent protons in the  $y < 0$  half space are greater than in the  $y > 0$  half space by at least a factor of 3, and protons reaching altitudes within one atmospheric scale height are more prone to impacting the surface in the  $y < 0$  hemisphere. Hence, the  $y < 0$  region of the image in Figure 11(f) is largely devoid of ENA flux. Conversely, when the detector is south of Europa (Figure 11(c)), the geometry of Figure 7(a) and thus the "favorable" side for ENA detection can be found in the Jupiter-averred half space. Lines of sight extending into the Jupiter-facing half space make larger angles against the magnetic field. Therefore, the  $y > 0$  region of the image is depleted of ENA flux.

When Europa is at maximum distance below the Jovian plasma sheet, the detectors positioned upstream and downstream of the moon again reveal two patches of elevated ENA flux above the north and south poles, partially populating the moon's disc (Figures 11(a) and 11(d), respectively). In the "pac-man" morphology seen at the center of the plasma sheet, the gap of low flux was aligned with Europa's equator. However, the gap in Figures 9(a) and 9(d) is rotated around the boresight vectors  $(\pm 1, 0, 0)$ . For instance, in Figure 11(a), the gap forms an angle of  $26^\circ$  against the horizontal ( $0^\circ$  azimuth) axis of the image. This rotation corresponds to the tilt  $\tilde{\eta}$  of the magnetic field lines projected onto the  $x = 0$  plane against the north-south direction, which causes

an analogous rotation of the proton gyroplanes against Europa's equator. In consequence, the gap in the "pac-man" feature is rotated against the horizontal axes of the images by approximately the same angle  $\tilde{\eta}$ . When Europa is at maximum distance below Jupiter's plasma sheet, the global ENA model of Haynes et al. (2023) revealed a similar rotation of the band of elevated ENA flux against the moon's equatorial plane: these authors found the tilt of  $\vec{B}_0$  to be responsible for the rotation.

In contrast to the images taken at the center of Jupiter's plasma sheet, the detectors positioned at  $(0, \pm 3R_E, 0)$  record only *a single* patch of elevated ENA flux (Figures 11(e) and 11(b)). This feature is located in the northern hemisphere for the detector on the sub-Jovian side of Europa (Figure 11(e)), and in the southern hemisphere for the detector on the anti-Jovian side (Figure 11(b)). To investigate the processes that may produce the dichotomy between these two ENA images, we calculate the range of pitch

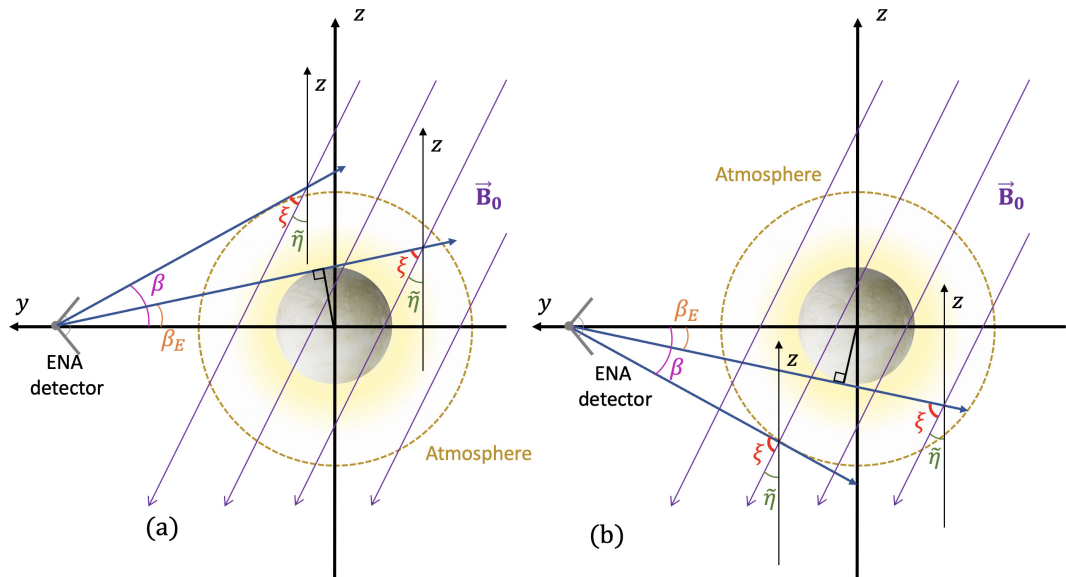


**Figure 12.** Schematic exemplifying the asymmetric range of angles  $\xi$  (red) between  $\vec{B}_0$  and a LOS extended from the sub-Jovian detector (Figure 11(e)) into the northern (panel (a)) and southern (panel (b)) half spaces, shown in the  $x = 0$  plane. Magnetospheric field lines projected into the  $x = 0$  plane are presented in purple, with the tilt angle of  $\tilde{\eta} = 28.5^\circ$  against the  $(-z)$  axis represented in green. The detector is again conveyed by the gray line segments, and the upper boundary of Europa's atmosphere in the model is indicated by the dashed yellow circle. The maximum angle  $\beta$  (magenta) and minimum angle  $\beta_E$  (orange) between the boresight vector and a LOS outside of Europa's disc are also included.

1178 angles for parent protons reaching a LOS in either the northern half space (Figure 12(a))  
 1179 or southern half space (Figure 12(b)). As exemplified by Figure 12(a), the angle  $\xi$  be-  
 1180 tween the magnetic field lines and a LOS is bounded between  $90^\circ - (\tilde{\eta} + \beta) = 19.7^\circ$   
 1181 and  $90^\circ - (\tilde{\eta} + \beta_E) = 42.0^\circ$  in the north. Here  $\beta_E$  and  $\beta$  represent the minimum and  
 1182 maximum opening angles (measured against the boresight) for a LOS intersecting Eu-  
 1183 opa’s atmosphere outside the moon’s disc, respectively. The range of  $\xi$  values is iden-  
 1184 tical to the range of pitch angles for parent protons that can contribute to the northern  
 1185 half of the ENA image:  $\alpha \in \{19.7^\circ, 42.0^\circ\}$ . Protons with such pitch angles are trans-  
 1186 lating southward, so the gyroplanes are tilted “downward” in the geometry of Figure 12.  
 1187 The range of pitch angles also implies that protons approaching from the south cannot  
 1188 contribute to the northern portion of the ENA image.

1189 In contrast, south of Europa  $\xi$  ranges between  $90^\circ + \beta_E - \tilde{\eta} = 81.0^\circ$  and  $90^\circ +$   
 1190  $\beta - \tilde{\eta} = 103.3^\circ$ , corresponding to pitch angles of  $\alpha \in \{81.0^\circ, 90.0^\circ\}$  for a proton com-  
 1191 ing from the north and  $\alpha \in \{90.0^\circ, 103.3^\circ\}$  for a proton coming from the south (Fig-  
 1192 ure 12(b)). Protons approaching from the north must pass the solid body of Europa be-  
 1193 fore entering the  $z < 0$  half space, making them prone to absorption prior to connect-  
 1194 ing to a LOS in the south (due to their nonzero gyroradii). In addition, when emitting  
 1195 an ENA in the south, the guiding center of such a proton can be no closer to the sur-  
 1196 face than  $(1/\cos \tilde{\eta} - 1) R_E \approx 0.14 R_E$ . Even for the largest proton gyroradii in our model  
 1197 ( $r_g = 0.06 R_E$  at  $E_7 = 75$  keV), these particles travel only through Europa’s dilute up-  
 1198 per atmosphere. Hence, they make only weak contributions to the ENA flux. Conversely,  
 1199 protons coming from the south can emit ENAs into the detector only below the LOS which  
 1200 is perpendicular to  $\mathbf{B}_0$ . The minimum altitude of this “critical” LOS is  $(3 \sin \tilde{\eta} - 1) R_E \approx$   
 1201  $0.43 R_E$ . Thus, these protons remain far outside the most dense part of the atmosphere  
 1202 and can contribute only a weak ENA flux. These effects explain the absence of substan-  
 1203 tial ENA flux in the lower half of the image from Figure 11(e). Analogously, for the de-  
 1204 tector located at  $(0, -3R_E, 0)$ , protons that produce detectable ENAs in the *northern*  
 1205 half space have a reduced atmospheric accessibility compared to the southern half space,  
 1206 thereby contributing to the depletion in ENA flux for  $z > 0$  in Figure 11(b).

1207 Similar to Callisto, the induced dipole field at Europa is near its peak strength when  
 1208 the moon is at its maximum distance from the center of the Jovian plasma sheet. We  
 1209 have again generated synthetic ENA images for a mere superposition of  $\mathbf{B}_0$  and the moon’s  
 1210 induced dipole, as discussed in Appendix B. Compared to the case of uniform fields, the

induction signal imparts minor changes ( $\leq 10\%$ ) to the detectable ENA flux, while leaving the morphology of the synthetic images unaltered. Similar to our findings at Callisto for the corresponding case, the weak field line draping at Europa only slightly adjusts the observable ENA emissions from their appearance with the superposition of the dipole and  $\mathbf{B}_0$  (see also Appendix B). Thus, we discuss both the “superposition” scenario (right panels in Figure B1) and the “plasma interaction” scenario (right panels in Figure 11) in conjunction, again referring to them jointly with the term “non-uniform fields”.

Comparison between the left and right panels in Figures 11 and B1 reveals no distinct morphological differences between the ENA images for uniform and non-uniform fields. The thermal plasma density upstream of Europa falls by about 80% moving from the center to maximum distance below the Jovian plasma sheet (e.g., Roth et al., 2014). In consequence, the magnetic field perturbations generated by the plasma interaction are weakened in magnitude by about a factor of two (compare, e.g., Figures 3(g) and 3(h) in Haynes et al., 2023). Even below the center of the Jovian plasma sheet, the ambient field near Europa still points mainly southward. Therefore, the induced field is weak compared to the magnetospheric field (e.g., Zimmer et al., 2000) and produces only minor perturbations to the observable ENA emissions (see Appendix B). Hence, when Europa is at maximum distance below the Jovian plasma sheet, the influence of any non-uniformities in the moon’s electromagnetic environment may be challenging to discern in ENA images.

#### 4 Summary and Concluding Remarks

We have established a model to characterize the morphology of ENA emissions at Europa and Callisto, as observable by a spacecraft detector. Such ENAs are generated through charge exchange interactions between energetic magnetospheric ions and atmospheric neutral gas. Each ENA travels along a tangent line to its parent ion’s trajectory at the moment of charge exchange. The dynamics of the energetic parent ions are governed by the electromagnetic fields near each moon. Thus, in contrast to a magnetometer which provides the field vectors only along the spacecraft trajectory, the ENA emissions at both moons are encoded with information about the fields on a global scale. The first ENA camera to chart the morphology of detectable ENA emissions at Europa and

1242 Callisto is currently en route to Jupiter aboard the JUICE spacecraft (Grasset et al., 2013;  
 1243 Galli et al., 2022; Tosi et al., 2024).

1244 We employ the AIKEF hybrid model (Müller et al., 2011) to determine the three-  
 1245 dimensional structure of the draped electromagnetic fields near Europa and Callisto. These  
 1246 fields are then incorporated into a tracing tool for the energetic parent ions to calculate  
 1247 synthetic ENA images. For the synthetic ENA images generated in this paper, this tool  
 1248 launches energetic parent protons along the detector's lines of sight and traces them back-  
 1249 wards in time. The ENA flux emitted by these protons into every detector pixel is sub-  
 1250 sequently assembled into a synthetic ENA image, in a similar fashion to a mosaic.

1251 To emulate image acquisition by an actual ENA detector, we consider a (hypothet-  
 1252 ical) energy channel spanning from  $E = 5 \text{ keV}$  to  $E = 75 \text{ keV}$ . In order to study the  
 1253 ENA emission morphology from multiple vantages, we position detectors with boresight  
 1254 vectors oriented parallel/anti-parallel and perpendicular to the ambient magnetospheric  
 1255 field  $\mathbf{B}_0$ , as well as inclined against it. In all our synthetic ENA images, the detector's  
 1256 boresight vector points radially inward toward the center of the moon, that is, it is con-  
 1257 tained in a plane through the center. Each detector is placed outside of the atmosphere  
 1258 at an altitude of two moon radii from the surface. We generate sets of ENA images for  
 1259 Europa and Callisto located at the center and at maximum distance below the Jovian  
 1260 plasma sheet. In this way, we assess the variability of ENA observations. For each of these  
 1261 two configurations, we produce synthetic ENA images for both uniform and draped fields,  
 1262 revealing the influence of non-uniformities in Europa's and Callisto's electromagnetic en-  
 1263 vironments on the detectable ENA emissions. To isolate the impact of the induced field  
 1264 from each moon's subsurface ocean and/or ionosphere on the ENA images, we carry out  
 1265 additional runs using a mere superposition of the ambient magnetospheric field  $\mathbf{B}_0$  with  
 1266 the induced dipole. We report our major findings as follows:

- 1267 • Charge exchange between energetic magnetospheric protons and atmospheric neu-  
 1268 trals produces distinct ENA emissions at Europa and Callisto that may be detected  
 1269 by a spacecraft outside each moon's atmosphere. In (hypothetically) uniform elec-  
 1270 tromagnetic fields, the observable ENA flux populates segments of a ring along  
 1271 Europa's or Callisto's disc. The radial and angular extents of these segments de-  
 1272 pend on the orientation of the detector's boresight vector with respect to the back-

1273 ground field  $\mathbf{B}_0$  as well as the ambient field strength  $|\mathbf{B}_0|$  which determines the  
 1274 gyroradii of the parent protons.

- 1275 • When the detector's boresight is perpendicular to the ambient field  $\mathbf{B}_0$ , the frag-  
 1276 mentation of the ENA emission features into distinct segments of elevated flux grows  
 1277 with ambient field magnitude. This increased fragmentation is caused by the re-  
 1278 duction of the parent proton gyroradii with respect to the size of the moon as  $|\mathbf{B}_0|$   
 1279 gets stronger. Locations within the ring where the ENA flux is enhanced are de-  
 1280 termined by the parent protons' sense of gyration and the direction of their  $\mathbf{E}_0 \times$   
 1281  $\mathbf{B}_0$  drift.
- 1282 • In uniform fields, parent protons with steep pitch angles generate a ring of elevated  
 1283 ENA flux around Europa's or Callisto's disc. The uninterrupted ring is observ-  
 1284 able by detectors that have boresight vectors aligned or anti-aligned with  $\mathbf{B}_0$ . Ab-  
 1285 sorption by Europa's or Callisto's solid body depletes the disc itself of observable  
 1286 ENA flux.
- 1287 • When the detector boresight is neither parallel/anti-parallel nor perpendicular to  
 1288 the ambient field  $\mathbf{B}_0$ , parent protons contributing to segments of elevated ENA  
 1289 flux in the image have different gyroradii on either side of the moon. Absorption  
 1290 of a fraction of these protons at the surface results in a reduced ENA flux on the  
 1291 side where larger gyroradii are required, yielding a hemispheric asymmetry in the  
 1292 intensity of detectable ENA flux.
- 1293 • When Europa or Callisto are near the center of the Jovian plasma sheet, the in-  
 1294 teraction with the impinging flow generates the strongest field perturbations and  
 1295 is most effective at deflecting energetic proton trajectories (see also Haynes et al.,  
 1296 2023). However, draping is visible in the ENA images only for certain viewing ge-  
 1297ometries. For instance, when Callisto is at the center of the sheet, the asymme-  
 1298 try in the magnetic pile-up region cuts away a segment of elevated flux in ENA  
 1299 images taken from above the moon's geographic poles. When either moon is at  
 1300 maximum distance below the Jovian plasma sheet, non-uniformities in the fields  
 1301 are generated by both the plasma interaction and the induction signal. However,  
 1302 these non-uniform fields leave the morphology of the features in the ENA images  
 1303 largely unchanged and have only a minor, quantitative impact on the intensity of  
 the observed emissions. Thus, for the upcoming JUICE encounters of Europa and

1305 Callisto, the viewing geometry must be carefully selected to observe signatures of  
 1306 the plasma interaction or any induced fields with ENA imaging.

- 1307 • Asymmetries in the atmospheric neutral density are discernible in ENA images  
 1308 at both moons. Such asymmetries are predicted by models of Europa's and Cal-  
 1309 listo's neutral envelopes (e.g., Addison et al., 2021; Carberry Mogan et al., 2023;  
 1310 Oza et al., 2019). Hence, ENA imaging has the potential to remotely character-  
 1311 ize atmospheric asymmetries at both moons on a global scale.
- 1312 • At both moons, the induced magnetic field from the subsurface ocean and/or iono-  
 1313 sphere makes only subtle, quantitative contributions to the ENA emission mor-  
 1314 phology.

1315 In the future, the model presented here can be applied to support the planning and  
 1316 analysis of ENA observations along scheduled JUICE flybys of Callisto and Europa. In  
 1317 particular, our approach allows us to compare the morphology of ENA emissions from  
 1318 the magnetosphere-atmosphere interactions at both moons to the emission pattern of  
 1319 ENAs released from their surfaces (see also Pontoni et al., 2022; Szabo et al., 2024). How-  
 1320 ever, the current version of the model provides information only on the morphology, but  
 1321 not the absolute intensities of the features in the ENA images. This will change as soon  
 1322 as initial observations of the ENA emissions at Europa and Callisto become available to  
 1323 calibrate the model.

## 1324 **Appendix A Influence of Callisto's Induced Dipole on the Morphol-** 1325 **ogy of Synthetic ENA Images**

1326 Figure A1 shows synthetic ENA images for Callisto at maximum distance below  
 1327 the center of the Jovian plasma sheet. The layout of the figure is the same as in Figure  
 1328 6. These images are calculated with uniform electromagnetic fields (left plots) and com-  
 1329 pared to those calculated for a superposition of the background field  $\mathbf{B}_0$  with the induced  
 1330 dipole (right plots). This setup represents an “intermediate case” between uniform and  
 1331 draped fields, since no plasma interaction currents are included. Therefore, comparison  
 1332 between the left and right panels in Figure A1 allows the isolation of modifications to  
 1333 the ENA images caused by Callisto's induced dipole field specifically. In addition, com-  
 1334 parison to the images for draped fields in Figure 6 reveals changes introduced by the plasma  
 1335 interaction.

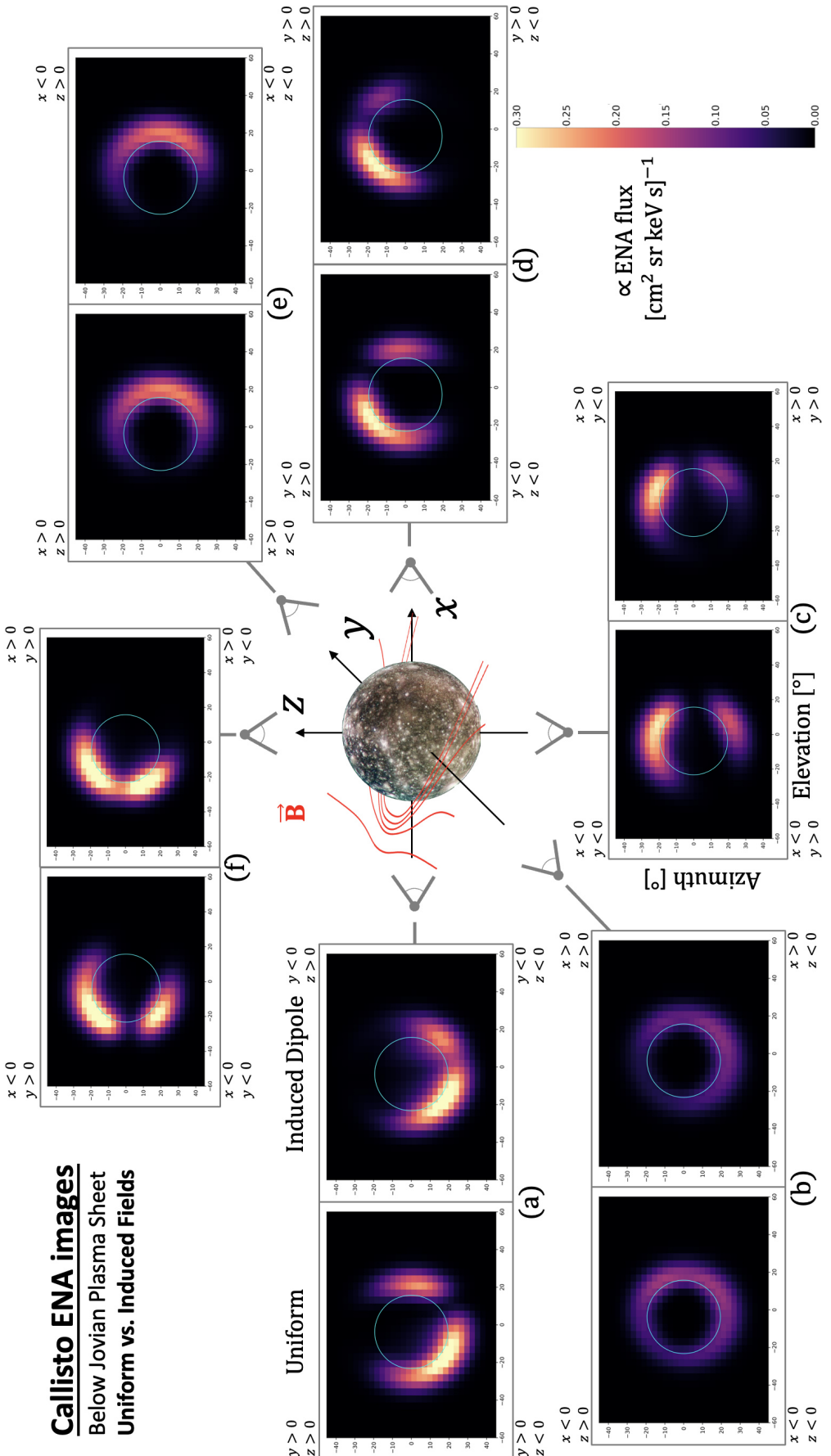


**Figure A1.** Synthetic ENA images illustrating the effect of the induced dipole when Callisto is at maximum distance below the center of the Jovian plasma sheet. The layout of the figure is the same as that of Figure 6. The ENA images on the left side of each panel are for uniform fields (i.e., these are identical to the left images in Figure 6), and the right images are calculated using the superposition of the ambient magnetospheric field  $\mathbf{B}_0$  and the induced dipole moment for this configuration is given by  $\mathbf{M}_{\text{ind}} = (-0.63, -2.50, 0) \cdot 10^{27} \text{ J/nT}$ . None of the images shown here include contributions from parent proton trajectories. The detector is positioned at  $|\mathbf{r}| = 3R_C$ , and the boresight vector always bears toward the center of the moon.

1336        The differences between ENA images with uniform fields and the induced dipole  
1337        field are largely *not* morphological, but quantitative in nature. The induced dipole mod-  
1338        ifies the magnetospheric field near Callisto by more than 50% only in isolated regions  
1339        just above the surface (e.g., Liuzzo et al., 2015). In consequence, adding the dipole field  
1340        to  $\mathbf{B}_0$  has a largely minor impact on the accessibility of the moon's atmosphere to en-  
1341        ergetic parent protons (Liuzzo et al., 2019b). Only in panel A1(d), the “patch” of ele-  
1342        vated ENA flux visible in the  $y > 0$  half space for uniform fields is strongly diminished  
1343        in extension and magnitude when Callisto's induced dipole field is included. The global  
1344        model of Haynes et al. (2023) revealed that Callisto's induced dipole redistributes a small  
1345        portion of the ENA flux produced by parent protons with pitch angles near 90°. This  
1346        effect contributes to the differences between the left and right ENA images in Figure A1(d).

1347 **Appendix B Influence of Europa's Induced Dipole on the Morphology  
1348 of Synthetic ENA Images**

1349       Figure B1 displays synthetic ENA images for Europa at maximum distance below  
1350 the center of the Jovian plasma sheet. Images in the left sub-panels are calculated with  
1351 the ambient magnetospheric field  $\mathbf{B}_0$  and electric field  $\mathbf{E}_0 = -\mathbf{u}_0 \times \mathbf{B}_0$ , that is, they  
1352 are identical to the left images in Figure 11. Images in the right sub-panels are calcu-  
1353 lated using a superposition of  $\mathbf{B}_0$  and Europa's induced dipole field. Similar to our find-  
1354 ings at Callisto, the induced dipole at Europa imparts minor quantitative changes on the  
1355 synthetic ENA images, but leaves the morphology of the emission patterns largely un-  
1356 changed. For detectors above the moon's north and south poles, the peak intensity of  
1357 the ENA emissions is reduced by nearly a factor of two with the inclusion of the induced  
1358 dipole field (panels B1(c) and B1(f)). However, this reduction is confined to only a few  
1359 pixels in each image. For the detectors in Europa's equatorial plane ( $z = 0$ ), the peak  
1360 intensity of the ENA flux is modified by 10% or less when the inductive response is in-  
1361 cluded. Because the magnetospheric field  $\mathbf{B}_0$  is predominantly southward at Europa's  
1362 orbit, the induced dipole adjusts the field near the moon by no more than  $|\mathbf{B}_0|/5$  (see,  
1363 e.g., Figures 7 and 9 in Addison et al., 2023). Therefore, proton trajectories accessing  
1364 Europa's atmosphere deviate only slightly from their paths through uniform fields, ex-  
1365 plaining the similarity between the right and left images of each panel in Figure B1.

1366 **Acknowledgments**

1367       The authors acknowledge financial support through NASA's *Solar System Work-*  
1368 *ings Program* 2019, grant # 80NSSC21K0152 as well as *Solar System Workings Program*  
1369 2020, grants # 80NSSC22K0097 and # 80NSSC23K0351. This body of work was not  
1370 written or contributed to in any part by an artificial intelligence engine such as GPT.

1371 **Open Research Section**

1372       Data supporting the production and conclusions of this work can be obtained from  
1373 Haynes et al. (2024).

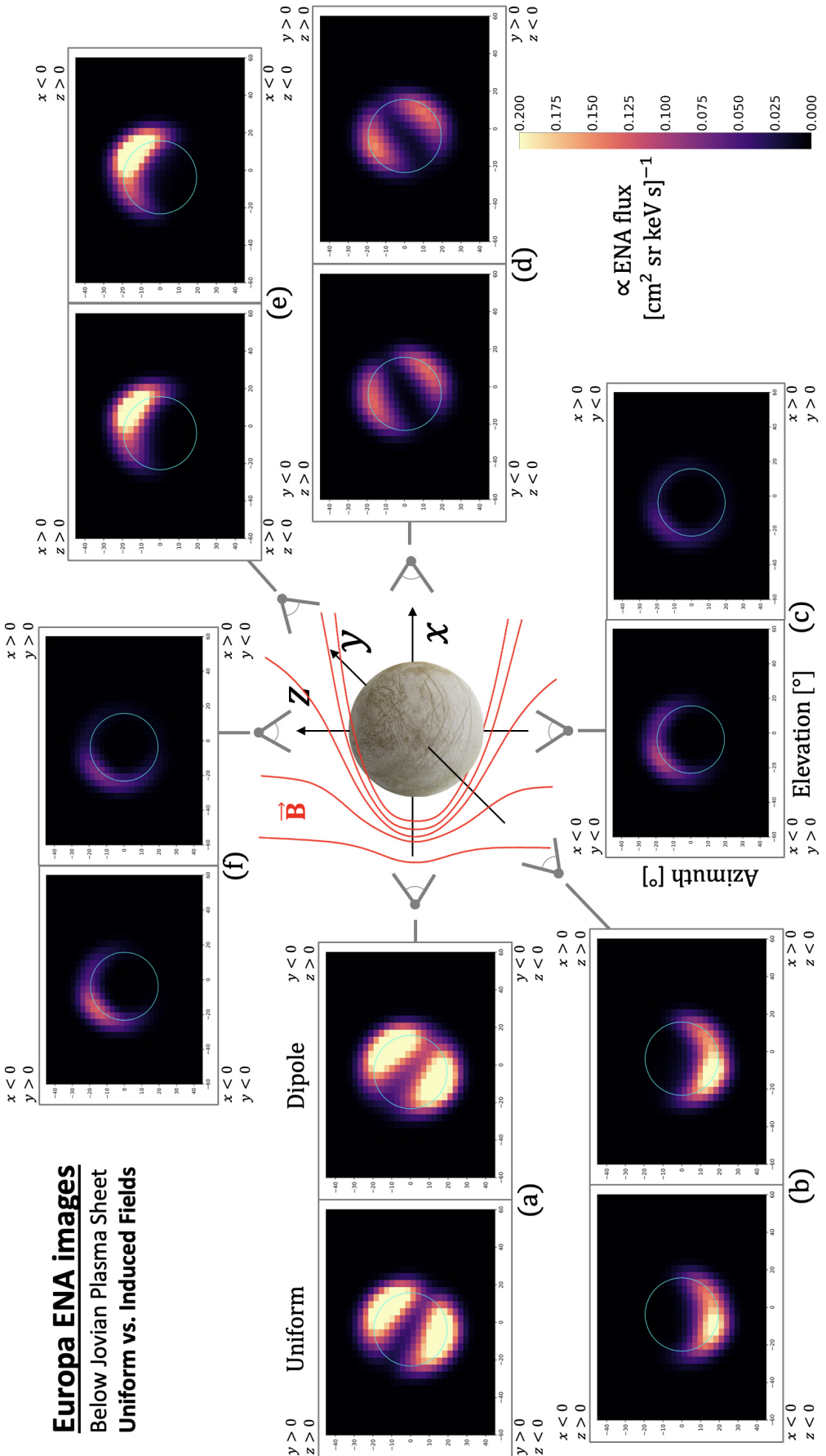


**Figure B1.** Synthetic ENA images depicting the influence of the induced dipole moment on Europa's plasma sheet. The layout of the figure is identical to that of Figure A1. The ENA images on the left side of each panel are for uniform fields; i.e., these are identical to the left images in Figure 11. The right-side images are calculated using a mere superposition of the ambient magnetospheric field  $\mathbf{B}_0$  and the induced dipole field. The induced dipole moment in this configuration reads  $\mathbf{M}_{\text{ind}} = (-0.01, -3.97, 0) \cdot 10^{27} \text{ J/nT}$ . None of the images shown in this figure include contributions from plasma currents to the trajectories of parent protons.

1374      **References**

- 1375      Addison, P., Haynes, C. M., Stahl, A. M., Liuzzo, L., & Simon, S. (2024). Magnetic  
 1376      Signatures of the Interaction Between Europa and Jupiter's Magnetosphere  
 1377      During the Juno Flyby. *Geophysical Research Letters*, 51(2), e2023GL106810.  
 1378      Retrieved from <https://agupubs.onlinelibrary.wiley.com/doi/abs/10.1029/2023GL106810> (e2023GL106810 2023GL106810) doi: <https://doi.org/10.1029/2023GL106810>
- 1381      Addison, P., Liuzzo, L., Arnold, H., & Simon, S. (2021). Influence of Eu-  
 1382      ropa's Time-Varying Electromagnetic Environment on Magnetospheric  
 1383      Ion Precipitation and Surface Weathering. *Journal of Geophysical Re-*  
 1384      *search: Space Physics*, 126(5), e2020JA029087. Retrieved from <https://agupubs.onlinelibrary.wiley.com/doi/abs/10.1029/2020JA029087> (e2020JA029087 2020JA029087) doi: <https://doi.org/10.1029/2020JA029087>
- 1387      Addison, P., Liuzzo, L., & Simon, S. (2022). Effect of the Magnetospheric Plasma  
 1388      Interaction and Solar Illumination on Ion Sputtering of Europa's Surface Ice.  
 1389      *Journal of Geophysical Research: Space Physics*, 127(2), e2021JA030136.  
 1390      Retrieved from <https://agupubs.onlinelibrary.wiley.com/doi/abs/10.1029/2021JA030136> (e2021JA030136 2021JA030136) doi: <https://doi.org/10.1029/2021JA030136>
- 1393      Addison, P., Liuzzo, L., & Simon, S. (2023). Surface-Plasma Interactions at Europa  
 1394      in Draped Magnetospheric Fields: The Contribution of Energetic Electrons to  
 1395      Energy Deposition and Sputtering. *Journal of Geophysical Research: Space*  
 1396      *Physics*, 128(8), e2023JA031734. doi: <https://doi.org/10.1029/2023JA031734>
- 1397      Arnold, H., Liuzzo, L., & Simon, S. (2019). Magnetic Signatures of a Plume at Eu-  
 1398      ropa during the Galileo E26 Flyby. *Geophysical Research Letters*, 46(3), 1149–  
 1399      1157. doi: [10.1029/2018GL081544](https://doi.org/10.1029/2018GL081544)
- 1400      Arnold, H., Liuzzo, L., & Simon, S. (2020). Plasma Interaction Signatures  
 1401      of Plumes at Europa. *Journal of Geophysical Research: Space Physics*,  
 1402      125(1), e2019JA027346. Retrieved from <https://agupubs.onlinelibrary.wiley.com/doi/abs/10.1029/2019JA027346> (e2019JA027346  
 1403      10.1029/2019JA027346) doi: [10.1029/2019JA027346](https://doi.org/10.1029/2019JA027346)
- 1405      Arnold, H., Simon, S., & Liuzzo, L. (2020). Applying Ion Energy Spec-  
 1406      trograms to Search for Plumes at Europa. *Journal of Geophysical Re-*

- 1407           *search: Space Physics, 125(9), e2020JA028376.*           Retrieved from <https://agupubs.onlinelibrary.wiley.com/doi/abs/10.1029/2020JA028376>  
 1408  
 1409  
 1410
- 1411       Bagenal, F., & Delamere, P. A. (2011). Flow of mass and energy in the magne-  
 1412       tospheres of Jupiter and Saturn. *Journal of Geophysical Research (Space*  
 1413       *Physics), 116*, A05209. doi: 10.1029/2010JA016294
- 1414       Bagenal, F., Sidrow, E., Wilson, R. J., Cassidy, T. A., Dols, V., Crary, F. J., ... Pa-  
 1415       terson, W. R. (2015, November). Plasma conditions at Europa's orbit. *Icarus,*  
 1416       *261*, 1-13. doi: 10.1016/j.icarus.2015.07.036
- 1417       Bagenal, F., Wilson, R. J., Siler, S., Paterson, W. R., & Kurth, W. S. (2016). Sur-  
 1418       vey of Galileo plasma observations in Jupiter's plasma sheet. *Journal of Geo-*  
 1419       *physical Research: Planets, 121*(5), 871-894. Retrieved from <https://agupubs.onlinelibrary.wiley.com/doi/abs/10.1002/2016JE005009> doi: <https://doi.org/10.1002/2016JE005009>
- 1422       Bhattacharyya, D., Clarke, J. T., Montgomery, J., Bonfond, B., Gérard, J.-C., &  
 1423       Grodent, D. (2018). Evidence for Auroral Emissions From Callisto's Footprint  
 1424       in HST UV Images. *Journal of Geophysical Research: Space Physics, 123*(1),  
 1425       364-373. Retrieved from <https://agupubs.onlinelibrary.wiley.com/doi/abs/10.1002/2017JA024791> doi: <https://doi.org/10.1002/2017JA024791>
- 1427       Bonfond, B., Saur, J., Grodent, D., Badman, S. V., Bisikalo, D., Shematovich,  
 1428       V., ... Radioti, A. (2017). The tails of the satellite auroral footprints at  
 1429       Jupiter. *Journal of Geophysical Research: Space Physics, 122*(8), 7985-7996.  
 1430       Retrieved from <https://agupubs.onlinelibrary.wiley.com/doi/abs/10.1002/2017JA024370> doi: <https://doi.org/10.1002/2017JA024370>
- 1432       Brandt, P., Dialynas, K., Dandouras, I., Mitchell, D., Garnier, P., & Krimigis, S.  
 1433       (2012). The distribution of Titan's high-altitude (out to 50,000km) exo-  
 1434       sphere from energetic neutral atom (ENA) measurements by Cassini/INCA.  
 1435       *Planetary and Space Science, 60*(1), 107-114.           Retrieved from <https://www.sciencedirect.com/science/article/pii/S0032063311001541> (Titan  
 1436       Through Time: A Workshop on Titan's Formation, Evolution and Fate) doi:  
 1437       <https://doi.org/10.1016/j.pss.2011.04.014>
- 1439       Breer, B. R., Liuzzo, L., Arnold, H., Andersson, P. N., & Simon, S. (2019). En-

- ergetic Ion Dynamics in the Perturbed Electromagnetic Fields near Europa.  
*Journal of Geophysical Research (Space Physics)*, 124(9), 7592–7613. doi:  
10.1029/2019JA027147

Carberry Mogan, S. R., Liuzzo, L., Poppe, A. R., Simon, S., Szalay, J. R., Tucker, O. J., & Johnson, R. E. (2023). Callisto's atmosphere: The oxygen enigma. *Journal of Geophysical Research: Planets*, 128(9), e2023JE007894. Retrieved from <https://agupubs.onlinelibrary.wiley.com/doi/abs/10.1029/2023JE007894> (e2023JE007894 2023JE007894) doi: <https://doi.org/10.1029/2023JE007894>

Carberry Mogan, S. R., Tucker, O. J., Johnson, R. E., Roth, L., Alday, J., Vorburger, A., ... Oza, A. V. (2022). Callisto's Atmosphere: First Evidence for H<sub>2</sub> and Constraints on H<sub>2</sub>O. *Journal of Geophysical Research: Planets*, 127(11), e2022JE007294. Retrieved from <https://agupubs.onlinelibrary.wiley.com/doi/abs/10.1029/2022JE007294> (e2022JE007294 2022JE007294) doi: <https://doi.org/10.1029/2022JE007294>

Carlson, R. (1999). A Tenuous Carbon Dioxide Atmosphere on Jupiter's Moon Callisto. *Science*, 283(5403), 820-821. Retrieved from <https://www.science.org/doi/abs/10.1126/science.283.5403.820> doi: 10.1126/science.283.5403.820

Carlson, R., Smythe, W., Baines, K., Barbinis, E., Becker, K., Burns, R., ... Weissman, P. (1996, October). Near-Infrared Spectroscopy and Spectral Mapping of Jupiter and the Galilean Satellites: Results from Galileo's Initial Orbit. *Science*, 274(5286), 385-388. doi: 10.1126/science.274.5286.385

Cervantes, S., & Saur, J. (2022). Constraining Europa's Subsolar Atmosphere With a Joint Analysis of HST Spectral Images and Galileo Magnetic Field Data. *Journal of Geophysical Research: Space Physics*, 127(9), e2022JA030472. Retrieved from <https://agupubs.onlinelibrary.wiley.com/doi/abs/10.1029/2022JA030472> (e2022JA030472 2022JA030472) doi: <https://doi.org/10.1029/2022JA030472>

Clark, G., Mauk, B., Paranicas, C., Haggerty, D. K., Kollmann, P., Rymer, A. M., ... Szalay, J. R. (2019, December). Energetic particle observations in Jupiter's polar magnetosphere: new discoveries by Juno. In *Agu fall meeting abstracts* (Vol. 2019, p. P42A-01).

- 1473 Clark, G., Mauk, B. H., Kollmann, P., Paranicas, C., Bagenal, F., Allen, R. C., ...  
 1474 Westlake, J. H. (2020). Heavy Ion Charge States in Jupiter's Polar Mag-  
 1475 netosphere Inferred From Auroral Megavolt Electric Potentials. *Journal of*  
*1476 Geophysical Research: Space Physics*, 125(9), e2020JA028052. Retrieved  
*1477* from <https://agupubs.onlinelibrary.wiley.com/doi/abs/10.1029/2020JA028052> (e2020JA028052 2020JA028052) doi: <https://doi.org/10.1029/2020JA028052>
- 1480 Cohen, C. M. S., Stone, E. C., & Selesnick, R. S. (2001). Energetic ion obser-  
 1481 vations in the middle Jovian magnetosphere. *Journal of Geophysical Re-*  
*1482 search: Space Physics*, 106(A12), 29871-29881. Retrieved from <https://agupubs.onlinelibrary.wiley.com/doi/abs/10.1029/2001JA000008> doi:  
*1483* <https://doi.org/10.1029/2001JA000008>
- 1485 Connerney, J. E. P., Kotsiaros, S., Oliverson, R. J., Espley, J. R., Joergensen,  
 1486 J. L., Joergensen, P. S., ... Levin, S. M. (2018). A New Model of Jupiter's  
 1487 Magnetic Field From Juno's First Nine Orbits. *Geophysical Research Let-*  
*1488 ters*, 45(6), 2590-2596. Retrieved from <https://agupubs.onlinelibrary.wiley.com/doi/abs/10.1002/2018GL077312> doi: <https://doi.org/10.1002/2018GL077312>
- 1490 Connerney, J. E. P., Timmins, S., Herceg, M., & Joergensen, J. L. (2020). A  
 1491 Jovian Magnetodisc Model for the Juno Era. *Journal of Geophysical Re-*  
*1492 search: Space Physics*, 125(10), e2020JA028138. Retrieved from <https://agupubs.onlinelibrary.wiley.com/doi/abs/10.1029/2020JA028138> (e2020JA028138 2020JA028138) doi: <https://doi.org/10.1029/2020JA028138>
- 1496 Connerney, J. E. P., Timmins, S., Oliverson, R. J., Espley, J. R., Joergensen, J. L.,  
 1497 Kotsiaros, S., ... Levin, S. M. (2022). A New Model of Jupiter's Magnetic  
 1498 Field at the Completion of Juno's Prime Mission. *Journal of Geophys-*  
*1499 ical Research: Planets*, 127(2), e2021JE007055. Retrieved from <https://agupubs.onlinelibrary.wiley.com/doi/abs/10.1029/2021JE007055> (e2021JE007055 2021JE007055) doi: <https://doi.org/10.1029/2021JE007055>
- 1502 Cunningham, N. J., Spencer, J. R., Feldman, P. D., Strobel, D. F., France, K., &  
 1503 Osterman, S. N. (2015). Detection of Callisto's oxygen atmosphere with the  
 1504 Hubble Space Telescope. *Icarus*, 254, 178-189. Retrieved from <https://www.sciencedirect.com/science/article/pii/S0019103515001219> doi:

- 1506 https://doi.org/10.1016/j.icarus.2015.03.021
- 1507 Dandouras, J., & Amsif, A. (1999). Production and imaging of energetic neutral  
1508 atoms from Titan's exosphere: a 3-D model. *Planetary and Space Science*,  
1509 47(10), 1355-1369. Retrieved from <https://www.sciencedirect.com/science/article/pii/S0032063399000574> doi: [https://doi.org/10.1016/S0032-0633\(99\)00057-4](https://doi.org/10.1016/S0032-0633(99)00057-4)
- 1510 de Kleer, K., Milby, Z., Schmidt, C., Camarca, M., & Brown, M. E. (2023, Feb.).  
1511 The Optical Aurorae of Europa, Ganymede, and Callisto. *The Planetary Sci-  
1512 ence Journal*, 4(2), 37. Retrieved from <https://dx.doi.org/10.3847/PSJ/acb53c> doi: 10.3847/PSJ/acb53c
- 1513 Dialynas, K., Krimigis, S. M., Mitchell, D. G., Roelof, E. C., & Decker, R. B. (2013,  
1514 nov.). A three-coordinate system (ecliptic, galactic, ismf) spectral analysis of  
1515 heliospheric ena emissions using cassini/inca measurements. *The Astrophysi-  
1516 cal Journal*, 778(1), 40. Retrieved from <https://dx.doi.org/10.1088/0004-637X/778/1/40> doi: 10.1088/0004-637X/778/1/40
- 1517 Galli, A., Vorburger, A., Carberry Mogan, S. R., Roussos, E., Stenberg Wieser, G.,  
1518 Wurz, P., ... Liuzzo, L. (2022). Callisto's Atmosphere and Its Space Envi-  
1519 ronment: Prospects for the Particle Environment Package on Board JUICE.  
1520 *Earth and Space Science*, 9(5), e2021EA002172. Retrieved from <https://agupubs.onlinelibrary.wiley.com/doi/abs/10.1029/2021EA002172>  
(e2021EA002172 2021EA002172) doi: <https://doi.org/10.1029/2021EA002172>
- 1521 Galli, A., Vorburger, A., Wurz, P., Pommerol, A., Cerubini, R., Jost, B., ...  
1522 Thomas, N. (2018, Jun.). 0.2 to 10 keV electrons interacting with water  
1523 ice: Radiolysis, sputtering, and sublimation. *Planet. Space Sci.*, 155, 91-98.  
1524 doi: 10.1016/j.pss.2017.11.016
- 1525 Grasset, O., Dougherty, M., Coustenis, A., Bunce, E., Erd, C., Titov, D., ... Van  
1526 Hoolst, T. (2013). JUpiter ICy moons Explorer (JUICE): An ESA mission  
1527 to orbit Ganymede and to characterise the Jupiter system. *Planetary and  
1528 Space Science*, 78, 1-21. Retrieved from <https://www.sciencedirect.com/science/article/pii/S0032063312003777> doi: <https://doi.org/10.1016/j.pss.2012.12.002>
- 1529 Gurnett, D. A., Persoon, A. M., Kurth, W. S., Roux, A., & Bolton, S. J. (2000).  
1530 Plasma densities in the vicinity of Callisto from Galileo plasma wave ob-

- 1539      servations.     *Geophysical Research Letters*, 27(13), 1867-1870.     Retrieved  
1540      from <https://agupubs.onlinelibrary.wiley.com/doi/abs/10.1029/2000GL003751>     doi: <https://doi.org/10.1029/2000GL003751>

1541

1542      Hall, D. T., Feldman, P. D., McGrath, M. A., & Strobel, D. F.    (1998, may).   The  
1543      Far-Ultraviolet Oxygen Airglow of Europa and Ganymede.   *The Astrophysical  
1544      Journal*, 499(1), 475.   Retrieved from <https://dx.doi.org/10.1086/305604>  
1545      doi: 10.1086/305604

1546

1547      Hall, D. T., Strobel, D. F., Feldman, P. D., McGrath, M. A., & Weaver, H. A.  
1548      (1995, February).   Detection of an oxygen atmosphere on Jupiter's moon Eu-  
ropa.   *Nature*, 373, 677-679.   doi: 10.1038/373677a0

1549

1550      Harris, C. D. K., Jia, X., Slavin, J. A., Toth, G., Huang, Z., & Rubin, M.  
1551      (2021).       Multi-Fluid MHD Simulations of Europa's Plasma Interaction  
1552      Under Different Magnetospheric Conditions.       *Journal of Geophysical Re-  
1553      search: Space Physics*, 126(5), e2020JA028888.       Retrieved from <https://agupubs.onlinelibrary.wiley.com/doi/abs/10.1029/2020JA028888>  
1554      (e2020JA028888 2020JA028888)     doi: <https://doi.org/10.1029/2020JA028888>

1555

1556      Hartkorn, O., & Saur, J.    (2017).   Induction signals from Callisto's ionosphere and  
1557      their implications on a possible subsurface ocean.       *Journal of Geophysical  
1558      Research: Space Physics*, 122(11), 11,677-11,697.       Retrieved from <https://agupubs.onlinelibrary.wiley.com/doi/abs/10.1002/2017JA024269>     doi:  
1559      <https://doi.org/10.1002/2017JA024269>

1560

1561      Haynes, C. M., Tippens, T., Addison, P., Liuzzo, L., Poppe, A. R., & Simon, S.  
1562      (2023).       Emission of Energetic Neutral Atoms from the Magnetosphere-  
1563      Atmosphere Interactions at Callisto and Europa.       *Journal of Geophysical  
1564      Research: Space Physics*, 128, e2023JA031931.     doi: 10.1029/2023JA031931

1565

1566      Haynes, C. M., Tippens, T., Simon, S., & Liuzzo, L.    (2024).   Data for "Constraints  
1567      on the Observability of Energetic Neutral Atoms from the Magnetosphere-  
1568      Atmosphere Interactions at Callisto and Europa" by Haynes et al., 2024  
1569      [Data set].       *Zenodo*, <https://doi.org/10.5281/zenodo.13840145>.     doi:  
1570      [10.5281/zenodo.13840145](https://doi.org/10.5281/zenodo.13840145)

1571

1572      Huybrighs, H. L. F., Blöcker, A., Roussos, E., van Buchem, C., Futaana, Y., Holm-  
1573      berg, M. K. G., ... Witasse, O.    (2023).   Europa's Perturbed Fields and  
1574      Induced Dipole Affect Energetic Proton Depletions During Distant Alfvén

- 1572 Wing Flybys. *Journal of Geophysical Research: Space Physics*, 128(9),  
 1573 e2023JA031420. Retrieved from <https://agupubs.onlinelibrary.wiley.com/doi/abs/10.1029/2023JA031420> (e2023JA031420 2023JA031420) doi:  
 1574 <https://doi.org/10.1029/2023JA031420>
- 1575 Kabanovic, S., Feyerabend, M., Simon, S., Meeks, Z., & Wulms, V. (2018, March).  
 1576 Influence of asymmetries in the magnetic draping pattern at Titan on the  
 1577 emission of energetic neutral atoms. *Planet. Space Sci.*, 152, 142-164. doi:  
 1578 [10.1016/j.pss.2017.12.017](https://doi.org/10.1016/j.pss.2017.12.017)
- 1579 Khurana, K. K. (1997). Euler potential models of Jupiter's magnetospheric field.  
 1580 *Journal of Geophysical Research (Space Physics)*, 102, 11295–11306. doi: 10  
 1581 .1029/97JA00563
- 1582 Khurana, K. K., Kivelson, M. G., Stevenson, D. J., Schubert, G., Russell, C. T.,  
 1583 Walker, R. J., & Polanskey, C. (1998). Induced magnetic fields as evidence for  
 1584 subsurface oceans in Europa and Callisto. *Nature*, 395(6704), 777–780. doi:  
 1585 [10.1038/27394](https://doi.org/10.1038/27394)
- 1586 Khurana, K. K., Mitchell, D. G., Arridge, C. S., Dougherty, M. K., Russell,  
 1587 C. T., Paranicas, C., ... Coates, A. J. (2009). Sources of rotational sig-  
 1588 nals in Saturn's magnetosphere. *J. Geophys. Res.*, 114, A02211. doi:  
 1589 [10.1029/2008JA013312](https://doi.org/10.1029/2008JA013312)
- 1590 Kivelson, M. G., Bagenal, F., Kurth, W. S., Neubauer, F. M., Paranicas, C., &  
 1591 Saur, J. (2004). Magnetospheric interactions with satellites. In F. Bagenal,  
 1592 T.E. Dowling and W.B. McKinnon (Ed.), *Jupiter. The planet, satellites and*  
 1593 *magnetosphere* (pp. 513–536). Cambridge Univ. Press.
- 1594 Kivelson, M. G., Khurana, K. K., Russell, C. T., Volwerk, M., Walker, R. J., & Zim-  
 1595 mer, C. (2000). Galileo Magnetometer Measurements: A Stronger Case for  
 1596 a Subsurface Ocean at Europa. *Science*, 289(5483), 1340–1343. Retrieved  
 1597 from <https://science.sciencemag.org/content/289/5483/1340> doi:  
 1598 [10.1126/science.289.5483.1340](https://doi.org/10.1126/science.289.5483.1340)
- 1599 Kivelson, M. G., Khurana, K. K., Stevenson, D. J., Bennett, L., Joy, S., Russell,  
 1600 C. T., ... Polanskey, C. (1999). Europa and Callisto: Induced or intrinsic  
 1601 fields in a periodically varying plasma environment. *Journal of Geophysical*  
 1602 *Research (Space Physics)*, 104(A3), 4609–4626. doi: 10.1029/1998JA900095
- 1603 Kivelson, M. G., Khurana, K. K., & Volwerk, M. (2009). Europa's Interaction  
 1604

- 1605 with the Jovian Magnetosphere. In R. T. Pappalardo, W. B. McKinnon, &  
 1606 K. K. Khurana (Eds.), *Europa, edited by robert t. pappalardo, william b. mckin-  
 1607 non, krishan k. khurana ; with the assistance of rené dotson with 85 collaborat-  
 1608 ing authors. university of arizona press, tucson, 2009. the university of arizona  
 1609 space science series isbn: 9780816528448, p.545* (p. 545).
- 1610 Kliore, A. J., Anabtawi, A., Herrera, R. G., Asmar, S. W., Nagy, A. F., Hin-  
 1611 son, D. P., & Flasar, F. M. (2002). Ionosphere of Callisto from Galileo  
 1612 radio occultation observations. *Journal of Geophysical Research: Space  
 1613 Physics*, 107(A11), SIA 19-1-SIA 19-7. Retrieved from <https://agupubs.onlinelibrary.wiley.com/doi/abs/10.1029/2002JA009365> doi:  
 1614 <https://doi.org/10.1029/2002JA009365>
- 1615 Kollmann, P., Hill, M. E., McNutt, R. L., Brown, L. E., Allen, R. C., Clark, G., ...  
 1616 Szalay, J. R. (2019, may). Suprathermal ions in the outer heliosphere. *The  
 1617 Astrophysical Journal*, 876(1), 46. Retrieved from <https://dx.doi.org/10.3847/1538-4357/ab125f> doi: 10.3847/1538-4357/ab125f
- 1618 Krimigis, S. M., Mitchell, D. G., Hamilton, D. C., Livi, S., Dandouras, J., Jaskulek,  
 1619 S., ... Williams, D. J. (2004, September). Magnetosphere Imaging Instrument  
 1620 (MIMI) on the Cassini Mission to Saturn/Titan. *Space Science Reviews*, 114,  
 1621 233–329, doi: 10.1007/s11214-004-1410-8.
- 1622 Liang, M.-C., Lane, B. F., Pappalardo, R. T., Allen, M., & Yung, Y. L. (2005).  
 1623 Atmosphere of callisto. *Journal of Geophysical Research: Planets*, 110(E2).  
 1624 Retrieved from <https://agupubs.onlinelibrary.wiley.com/doi/abs/10.1029/2004JE002322> doi: <https://doi.org/10.1029/2004JE002322>
- 1625 Lindsay, B. G., & Stebbings, R. F. (2005, December). Charge transfer cross sec-  
 1626 tions for energetic neutral atom data analysis. *Journal of Geophysical Research  
 1627 (Space Physics)*, 110, A12213. doi: 10.1029/2005JA011298
- 1628 Lindsay, B. G., Yu, W. S., & Stebbings, R. F. (2005, Mar). Cross sections for  
 1629 charge-changing processes involving kilo-electron-volt H and H<sup>+</sup> with CO and  
 1630 CO<sub>2</sub>. *Phys. Rev. A*, 71, 032705. Retrieved from <https://link.aps.org/doi/10.1103/PhysRevA.71.032705> doi: 10.1103/PhysRevA.71.032705
- 1631 Liuzzo, L., Feyenabend, M., Simon, S., & Motschmann, U. (2015, November). The  
 1632 impact of Callisto's atmosphere on its plasma interaction with the Jovian mag-  
 1633 netosphere. *Journal of Geophysical Research (Space Physics)*, 120, 9401-9427.  
 1634

- 1638 doi: 10.1002/2015JA021792
- 1639 Liuzzo, L., Poppe, A. R., Addison, P., Simon, S., Nénon, Q., & Paranicas, C. (2022).  
 1640 Energetic Magnetospheric Particle Fluxes onto Callisto's Atmosphere. *Journal*  
 1641 *of Geophysical Research: Space Physics*, n/a(n/a), e2022JA030915. Retrieved  
 1642 from <https://agupubs.onlinelibrary.wiley.com/doi/abs/10.1029/2022JA030915> (e2022JA030915 2022JA030915) doi: <https://doi.org/10.1029/2022JA030915>
- 1643 Liuzzo, L., Poppe, A. R., Nénon, Q., Simon, S., & Addison, P. (2024). Constraining the Influence of Callisto's Perturbed Electromagnetic Environment on Energetic Particle Observations. *Journal of Geophysical Research: Space Physics*, 129(2), e2023JA032189. Retrieved from <https://agupubs.onlinelibrary.wiley.com/doi/abs/10.1029/2023JA032189> (e2023JA032189 2023JA032189) doi: <https://doi.org/10.1029/2023JA032189>
- 1644 Liuzzo, L., Simon, S., & Feyerabend, M. (2018). Observability of Callisto's Inductive Signature During the JUpiter ICY Moons Explorer Mission. *Journal of Geophysical Research: Space Physics*, 123(11), 9045–9054. Retrieved from <https://agupubs.onlinelibrary.wiley.com/doi/abs/10.1029/2018JA025951> doi: <https://doi.org/10.1029/2018JA025951>
- 1645 Liuzzo, L., Simon, S., Feyerabend, M., & Motschmann, U. (2016). Disentangling plasma interaction and induction signatures at Callisto: The Galileo C10 flyby. *Journal of Geophysical Research: Space Physics*, 121(9), 8677–8694. Retrieved from <http://dx.doi.org/10.1002/2016JA023236> doi: [10.1002/2016JA023236](https://doi.org/10.1002/2016JA023236)
- 1646 Liuzzo, L., Simon, S., Feyerabend, M., & Motschmann, U. (2017). Magnetic signatures of plasma interaction and induction at Callisto: The Galileo C21, C22, C23, and C30 flybys. *Journal of Geophysical Research: Space Physics*, 122(7), 7364–7386. doi: [10.1002/2017JA024303](https://doi.org/10.1002/2017JA024303)
- 1647 Liuzzo, L., Simon, S., & Regoli, L. (2019a). Energetic electron dynamics near Callisto. *Planetary and Space Science*, 179, 104726. Retrieved from <http://www.sciencedirect.com/science/article/pii/S0032063319302430> doi: <https://doi.org/10.1016/j.pss.2019.104726>
- 1648 Liuzzo, L., Simon, S., & Regoli, L. (2019b). Energetic ion dynamics near Callisto. *Planetary and Space Science*, 166, 23–53. Retrieved from <https://doi.org/10.1016/j.pss.2019.104726>

- 1671                    [www.sciencedirect.com/science/article/pii/S0032063318301648](http://www.sciencedirect.com/science/article/pii/S0032063318301648)       doi:  
 1672                    <https://doi.org/10.1016/j.pss.2018.07.014>
- 1673                    Mauk, B. H., Allegrini, F., Bagenal, F., Bolton, S. J., Clark, G., Connerney, J. E. P.,  
 1674                    ... Rymer, A. M. (2020). Energetic Neutral Atoms From Jupiter's Po-  
 1675                    lar Regions. *Journal of Geophysical Research: Space Physics*, 125(12),  
 1676                    e2020JA028697. Retrieved from <https://agupubs.onlinelibrary.wiley.com/doi/abs/10.1029/2020JA028697> (e2020JA028697 2020JA028697) doi:  
 1677                    <https://doi.org/10.1029/2020JA028697>
- 1679                    Mauk, B. H., Clark, G., Allegrini, F., Bagenal, F., Bolton, S. J., Connerney, J. E. P.,  
 1680                    ... Rymer, A. M. (2020). Juno Energetic Neutral Atom (ENA) Remote Mea-  
 1681                    surements of Magnetospheric Injection Dynamics in Jupiter's Io Torus Regions.  
 1682                    *Journal of Geophysical Research: Space Physics*, 125(5), e2020JA027964.  
 1683                    Retrieved from <https://agupubs.onlinelibrary.wiley.com/doi/abs/10.1029/2020JA027964> (e2020JA027964 2020JA027964) doi: <https://doi.org/10.1029/2020JA027964>
- 1686                    Mauk, B. H., Mitchell, D., Krimigis, S., Roelof, E., & Paranicas, C. (2003, Febru-  
 1687                    ary). Energetic neutral atoms from a trans-Europa gas torus at Jupiter.  
 1688                    *Nature*, 421(6926), 920—922. Retrieved from <https://doi.org/10.1038/nature01431> doi: 10.1038/nature01431
- 1690                    Mauk, B. H., Mitchell, D., McEntire, R., Paranicas, C., Roelof, E., Williams, D., ...  
 1691                    Lagg, A. (2004). Energetic ion characteristics and neutral gas interactions  
 1692                    in Jupiter's magnetosphere. *Journal of Geophysical Research: Space Physics*,  
 1693                    109(A9). doi: 10.1029/2003JA010270
- 1694                    Mitchell, D. G., Brandt, P. C., Roelof, E. C., Dandouras, J., Krimigis, S. M., &  
 1695                    Mauk, B. H. (2005). Energetic Neutral Atom Emissions from Titan Interac-  
 1696                    tion with Saturn's Magnetosphere. *Science*, 308(5724), 989-992. Retrieved  
 1697                    from <https://www.science.org/doi/abs/10.1126/science.1109805> doi:  
 1698                    10.1126/science.1109805
- 1699                    Mitchell, D. G., Brandt, P. C., Westlake, J. H., Jaskulek, S. E., Andrews, G. B.,  
 1700                    & Nelson, K. S. (2016). Energetic particle imaging: The evolution of tech-  
 1701                    niques in imaging high-energy neutral atom emissions. *Journal of Geophys-  
 1702                    ical Research: Space Physics*, 121(9), 8804-8820. Retrieved from <https://agupubs.onlinelibrary.wiley.com/doi/abs/10.1002/2016JA022586> doi:  
 1703                    10.1002/2016JA022586

- 1704 https://doi.org/10.1002/2016JA022586
- 1705 Mitchell, D. G., Cheng, A. F., Krimigis, S. M., Keath, E. P., Jaskulek, S. E., Mauk,  
 1706 B. H., ... Drake, V. A. (1993). INCA: the ion neutral camera for energetic  
 1707 neutral atom imaging of the Saturnian magnetosphere. *Optical Engineering*,  
 1708 32(12), 3096 – 3101. Retrieved from <https://doi.org/10.1117/12.155609>  
 1709 doi: 10.1117/12.155609
- 1710 Mitchell, D. G., Krimigis, S. M., Cheng, A. F., Hsieh, S.-L., Jaskulek, S. E., Keath,  
 1711 E. P., ... Williams, D. J. (1996). Imaging-neutral camera (INCA) for the  
 1712 NASA Cassini mission to Saturn and Titan. *Proceedings of SPIE*, 2803,  
 1713 154 – 161. Retrieved from <https://doi.org/10.1117/12.253415> doi:  
 1714 10.1117/12.253415
- 1715 Moirano, A., Mura, A., Hue, V., Bonfond, B., Head, L. A., Connerney, J. E. P., ...  
 1716 Zambon, F. (2024). The Infrared Auroral Footprint Tracks of Io, Europa  
 1717 and Ganymede at Jupiter Observed by Juno-JIRAM. *Journal of Geophys-*  
 1718 *ical Research: Planets*, 129(3), e2023JE008130. Retrieved from <https://agupubs.onlinelibrary.wiley.com/doi/abs/10.1029/2023JE008130>  
 1719 (e2023JE008130 2023JE008130) doi: <https://doi.org/10.1029/2023JE008130>
- 1720 Müller, J., Simon, S., Motschmann, U., Schüle, J., Glassmeier, K.-H., & Pringle,  
 1721 G. J. (2011). A.i.k.e.f.: Adaptive hybrid model for space plasma sim-  
 1722 ulations. *Computer Physics Communications*, 182(4), 946-966. Retrieved  
 1723 from <https://www.sciencedirect.com/science/article/pii/S0010465510005266> doi: <https://doi.org/10.1016/j.cpc.2010.12.033>
- 1724 Neubauer, F. M. (1980). Nonlinear standing Alfvén wave current system at Io - The-  
 1725 ory. *J. Geophys. Res.*, 85, 1171–1178. doi: 10.1029/JA085iA03p01171
- 1726 Neubauer, F. M. (1998). The sub-Alfvénic interaction of the Galilean satellites with  
 1727 the Jovian magnetosphere. *J. Geophys. Res.*, 103, 19843–19866. doi: 10.1029/  
 1728 97JE03370
- 1729 Neubauer, F. M. (1999). Alfvén wings and electromagnetic induction in the inte-  
 1730 riors: Europa and Callisto. *Journal of Geophysical Research (Space Physics)*,  
 1731 104(A12), 28671–28684. doi: 10.1029/1999JA900217
- 1732 Nordheim, T. A., Regoli, L. H., Harris, C. D. K., Paranicas, C., Hand, K. P., & Jia,  
 1733 X. (2022, jan). Magnetospheric Ion Bombardment of Europa’s Surface. *The  
 1734 Planetary Science Journal*, 3(1), 5. Retrieved from <https://dx.doi.org/>

- 1737            10.3847/PSJ/ac382a doi: 10.3847/PSJ/ac382a
- 1738        Oza, A. V., Leblanc, F., Johnson, R. E., Schmidt, C., Leclercq, L., Cassidy, T. A.,  
1739            & Chaufray, J.-Y. (2019). Dusk over dawn O<sub>2</sub> asymmetry in Europa's  
1740            near-surface atmosphere. *Planetary and Space Science*, 167, 23-32. Retrieved from <https://www.sciencedirect.com/science/article/pii/S0032063318301594> doi: <https://doi.org/10.1016/j.pss.2019.01.006>
- 1741        Paranicas, C., Cooper, J. F., Garrett, H. B., Johnson, R. E., & Sturner, S. J. (2009).  
1742            Europa's Radiation Environment and Its Effects on the Surface. In R. T. Pappalardo, W. B. McKinnon, & K. K. Khurana (Eds.), *Europa, edited by robert t. pappalardo, william b. mckinnon, krishan k. khurana ; with the assistance of rené dotson with 85 collaborating authors. university of arizona press, tucson, 2009. the university of arizona space science series isbn: 9780816528448, p.529*  
1743            (p. 529).
- 1744        Paranicas, C., McEntire, R. W., Cheng, A. F., Lagg, A., & Williams, D. J. (2000,  
1745            July). Energetic charged particles near Europa. *J. Geophys. Res.*, 105, 16005-  
1746            16016. doi: 10.1029/1999JA000350
- 1747        Paranicas, C., Ratliff, J. M., Mauk, B. H., Cohen, C., & Johnson, R. E. (2002,  
1748            March). The ion environment near Europa and its role in surface energetics.  
1749            *GRL*, 29, 18-1. doi: 10.1029/2001GL014127
- 1750        Phipps, P., & Bagenal, F. (2021). Centrifugal Equator in Jupiter's Plasma Sheet.  
1751            *Journal of Geophysical Research: Space Physics*, 126(1), e2020JA028713.  
1752            Retrieved from <https://agupubs.onlinelibrary.wiley.com/doi/abs/10.1029/2020JA028713> (e2020JA028713 2020JA028713) doi: <https://doi.org/10.1029/2020JA028713>
- 1753        Plainaki, C., Cassidy, T. A., Shematovich, V. I., Milillo, A., Wurz, P., Vorburger, A., ... Teolis, B. (2018, February). Towards a Global Unified  
1754            Model of Europa's Tenuous Atmosphere. *Space Sci. Rev.*, 214, 40. doi:  
1755            10.1007/s11214-018-0469-6
- 1756        Pontoni, A., Shimoyama, M., Futaana, Y., Fatemi, S., Poppe, A. R., Wieser, M., &  
1757            Barabash, S. (2022). Simulations of Energetic Neutral Atom Sputtering From  
1758            Ganymede in Preparation for the JUICE Mission. *Journal of Geophysical Research: Space Physics*, 127(1), e2021JA029439. Retrieved from <https://agupubs.onlinelibrary.wiley.com/doi/abs/10.1029/2021JA029439>

- 1770 (e2021JA029439 2021JA029439) doi: <https://doi.org/10.1029/2021JA029439>
- 1771 Roth, L. (2021). A Stable H<sub>2</sub>O Atmosphere on Europa's Trailing Hemisphere  
1772 From HST Images. *Geophysical Research Letters*, 48(20), e2021GL094289.  
1773 Retrieved from <https://agupubs.onlinelibrary.wiley.com/doi/abs/10.1029/2021GL094289> (e2021GL094289 2021GL094289) doi: <https://doi.org/10.1029/2021GL094289>
- 1774 Roth, L., Retherford, K. D., Ivchenko, N., Schlatter, N., Strobel, D. F., Becker,  
1775 T. M., & Grava, C. (2017, Jan). Detection of a Hydrogen Corona in HST Ly  
1776 Images of Europa in Transit of Jupiter. *The Astronomical Journal*, 153(2),  
1777 67. Retrieved from <https://dx.doi.org/10.3847/1538-3881/153/2/67> doi:  
1778 [10.3847/1538-3881/153/2/67](https://doi.org/10.3847/1538-3881/153/2/67)
- 1779 Roth, L., Retherford, K. D., Saur, J., Strobel, D. F., Feldman, P. D., McGrath,  
1780 M. A., & Nimmo, F. (2014, December). Orbital apocenter is not a suf-  
1781 ficient condition for HST/STIS detection of Europa's water vapor aurora.  
1782 *Proceedings of the National Academy of Science*, 111, E5123-E5132. doi:  
1783 [10.1073/pnas.1416671111](https://doi.org/10.1073/pnas.1416671111)
- 1784 Roth, L., Saur, J., Retherford, K. D., Strobel, D. F., Feldman, P. D., McGrath,  
1785 M. A., ... Ivchenko, N. (2016). Europa's far ultraviolet oxygen aurora  
1786 from a comprehensive set of HST observations. *Journal of Geophysical Re-  
1787 search (Space Physics)*, n/a. Retrieved from <http://dx.doi.org/10.1002/2015JA022073> doi: [10.1002/2015JA022073](https://doi.org/10.1002/2015JA022073)
- 1788 Sarkango, Y., Szalay, J. R., Poppe, A. R., Nénon, Q., Kollmann, P., Clark, G.,  
1789 & McComas, D. J. (2023). Proton Equatorial Pitch Angle Distributions  
1790 in Jupiter's Inner Magnetosphere. *Geophysical Research Letters*, 50(11),  
1791 e2023GL104374. Retrieved from <https://agupubs.onlinelibrary.wiley.com/doi/abs/10.1029/2023GL104374> (e2023GL104374 2023GL104374) doi:  
1792 <https://doi.org/10.1029/2023GL104374>
- 1793 Saur, J., Strobel, D. F., & Neubauer, F. M. (1998, September). Interaction of the  
1794 Jovian magnetosphere with Europa: Constraints on the neutral atmosphere.  
1795 *Journal of Geophysical Research (Space Physics)*, 103, 19947–19962. doi:  
1796 [10.1029/97JE03556](https://doi.org/10.1029/97JE03556)
- 1797 Schilling, N., Neubauer, F. M., & Saur, J. (2007). Time-varying interaction of  
1798 Europa with the Jovian magnetosphere: Constraints on the conductivity of  
1799 Europa

- 1803 Europa's subsurface ocean. *Icarus*, 192(1), 41-55. Retrieved from <https://www.sciencedirect.com/science/article/pii/S0019103507002837> doi:  
 1804 <https://doi.org/10.1016/j.icarus.2007.06.024>
- 1805 Seufert, M., Saur, J., & Neubauer, F. M. (2011). Multi-frequency electromagnetic  
 1806 sounding of the Galilean moons. *Icarus*, 214(2), 477–494. doi: 10.1016/j.icarus  
 1807 .2011.03.017
- 1808 Shen, X.-C., Li, W., Ma, Q., Nishimura, Y., Daly, A., Kollmann, P., ... Bolton, S.  
 1809 (2022). Energetic Proton Distributions in the Inner and Middle Magnetosphere  
 1810 of Jupiter Using Juno Observations. *Geophysical Research Letters*, 49(16),  
 1811 e2022GL099832. Retrieved from <https://agupubs.onlinelibrary.wiley.com/doi/abs/10.1029/2022GL099832> (e2022GL099832 2022GL099832) doi:  
 1812 <https://doi.org/10.1029/2022GL099832>
- 1813 Smith, H., Mitchell, D. G., Johnson, R. E., Mauk, B. H., & Smith, J. E. (2019,  
 1814 jan). Europa neutral torus confirmation and characterization based on ob-  
 1815 servations and modeling. *The Astrophysical Journal*, 871(1), 69. Retrieved  
 1816 from <https://doi.org/10.3847/1538-4357/aaed38> doi: 10.3847/1538-4357/  
 1817 aaed38
- 1818 Spencer, J. R., Tamppari, L. K., Martin, T. Z., & Travis, L. D. (1999, May). Tem-  
 1819 peratures on Europa from Galileo Photopolarimeter-Radiometer: Nighttime  
 1820 Thermal Anomalies. *Science*, 284, 1514. doi: 10.1126/science.284.5419.1514
- 1821 Szabo, P. S., Poppe, A. R., Mutzke, A., Liuzzo, L., & Mogan, S. R. C. (2024,  
 1822 feb). Backscattering of Ions Impacting Ganymede's Surface as a Source for  
 1823 Energetic Neutral Atoms. *The Astrophysical Journal Letters*, 963(1), L32.  
 1824 Retrieved from <https://dx.doi.org/10.3847/2041-8213/ad2701> doi:  
 1825 <https://doi.org/10.3847/2041-8213/ad2701>
- 1826 Tippens, T., Liuzzo, L., & Simon, S. (2022). Influence of Titan's Variable Electro-  
 1827 magnetic Environment on the Global Distribution of Energetic Neutral Atoms.  
 1828 *Journal of Geophysical Research: Space Physics*, 127(10), e2022JA030722.  
 1829 Retrieved from <https://agupubs.onlinelibrary.wiley.com/doi/abs/10.1029/2022JA030722> (e2022JA030722 2022JA030722) doi: <https://doi.org/10.1029/2022JA030722>
- 1830 Tippens, T., Roussos, E., Simon, S., & Liuzzo, L. (2024). A Novel Backtracing  
 1831 Model to Study the Emission of Energetic Neutral Atoms at Titan. *Journal*  
 1832

- 1836        *of Geophysical Research: Space Physics*, 129(1), e2023JA032083.      Retrieved  
1837        from <https://agupubs.onlinelibrary.wiley.com/doi/abs/10.1029/2023JA032083> (e2023JA032083 2023JA032083) doi: <https://doi.org/10.1029/2023JA032083>
- 1840        Tosi, F., Roatsch, T., Galli, A., Hauber, E., Lucchetti, A., Molyneux, P., ...  
1841        Lorente, R. (2024, August). Characterization of the Surfaces and Near-Surface  
1842        Atmospheres of Ganymede, Europa and Callisto by JUICE.      *Space Science  
1843        Reviews*, 220(5), 59. doi: 10.1007/s11214-024-01089-8
- 1844        Vance, S. D., Panning, M. P., Stähler, S., Cammarano, F., Bills, B. G., Tobie, G.,  
1845        ... Banerdt, B. (2018). Geophysical Investigations of Habitability in Ice-  
1846        Covered Ocean Worlds.      *Journal of Geophysical Research: Planets*, 123(1),  
1847        180-205.      Retrieved from <https://agupubs.onlinelibrary.wiley.com/doi/abs/10.1002/2017JE005341> doi: <https://doi.org/10.1002/2017JE005341>
- 1848        Vance, S. D., Styczinski, M. J., Bills, B. G., Cochrane, C. J., Soderlund, K. M.,  
1849        Gómez-Pérez, N., & Paty, C. (2021). Magnetic Induction Responses of  
1850        Jupiter's Ocean Moons Including Effects From Adiabatic Convection.      *Jour-  
1851        nal of Geophysical Research: Planets*, 126(2), e2020JE006418.      Retrieved  
1852        from <https://agupubs.onlinelibrary.wiley.com/doi/abs/10.1029/2020JE006418> (e2020JE006418 2020JE006418) doi: <https://doi.org/10.1029/2020JE006418>
- 1853        Vorbburger, A., & Wurz, P. (2018). Europa's Ice-Related Atmosphere: The Sputter  
1854        Contribution. *Icarus*, 311, 135–145. doi: 10.1016/j.icarus.2018.03.022
- 1855        Wulms, V., Saur, J., Strobel, D. F., Simon, S., & Mitchell, D. G. (2010, June). En-  
1856        ergetic neutral atoms from Titan: Particle simulations in draped magnetic and  
1857        electric fields.      *Journal of Geophysical Research (Space Physics)*, 115, A06310,  
1858        doi: 10.1029/2009JA014893.
- 1859        Zimmer, C., Khurana, K. K., & Kivelson, M. G. (2000). Subsurface Oceans on  
1860        Europa and Callisto: Constraints from Galileo Magnetometer Observations.  
1861        *Icarus*, 147(2), 329–347. doi: 10.1006/icar.2000.6456